

Study on synthesis of valuable
compounds from diols

January 2008

Nishi Yoshikawa

Graduate School of Science and Technology
KUMAMOTO UNIVERSITY

Content

1. General introduction	1
1.1 Importance in the transformation of commodity chemicals	1
1.2 Synthesis of γ -butyrolactone from 1,4-butanediol	2
1.2.1 The production of 1,4-butanediol	2
1.2.2 Synthesis of γ -butyrolactone	4
1.3 Catalytic reactions of 1,3-butanediol over catalysts	5
1.3.1 Dehydrogenation of 1,3-butanediol over metal catalysts	5
1.3.2 Dehydration of 4-hydroxy-2-butanone into 3-buten-2-one	7
1.3.3 Dehydration of 1,3-butanediol over metal oxide catalysts	7
1.4 Constitution of this thesis	8
2. Dehydrogenative cyclization of 1,4-butanediol over copper-based catalyst	17
2.1 Introduction	17
2.2 Experimental	18
2.2.1 Catalyst preparation	18
2.2.2 Preparation procedure of 2HTHF and SDA	18
2.2.3 Catalytic reaction	19
2.3 Results	19
2.4 Discussion	22
2.4.1 Effects of additives on the physical and catalytic property	22
2.4.2 Kinetic consideration	23
2.4.3 Reaction pathway from 1,4-BDO to GBL	25
2.5 Conclusion	27
3. Synthesis of 3-buten-2-one from 4-hydroxy-2-butanone over anatase-TiO₂ catalyst	41
3.1 Introduction	41
3.2 Experimental	42
3.2.1. Catalyst samples	42
3.2.2. Catalytic reaction	42
3.3 Results and discussion	43
3.4 Conclusion	46

4. Catalytic Reaction of 1,3-butanediol over solid acids	53
4.1 Introduction	53
4.2 Experimental	54
4.3 Results	55
4.4 Discussion	57
4.4.1 Effects of acid and base properties of catalysts on catalytic performance	57
4.4.2 Different product-distribution among the catalysts	59
4.4.3 Reaction pathway from 1,3-BDO to products	61
4.5 Conclusion	62
5. Reaction of 1,3-butanediol over CeO₂	73
5.1 Introduction	73
5.2 Experimental	74
5.2.1 Characterization of CeO ₂ samples	74
5.2.2 Catalytic reaction	74
5.2.3 Calculation method	75
5.2.3.1 DFT calculation	75
5.2.3.2 PIO calculation	76
5.3 Results	77
5.3.1 Characterization of CeO ₂ catalysts calcined at different temperatures	77
5.3.2 Reaction of 1,3-BDO over CeO ₂	78
5.3.3 Investigation of 1,3-BDO adsorption on CeO ₂ (111) surface with DFT and PIO calculations	78
5.4 Discussion	81
5.4.1 Defect sites of CeO ₂ with different particle sizes	81
5.4.2 Characterization of CeO ₂ catalysts calcined at different temperatures	82
5.4.3 Reaction of 1,3-BDO over CeO ₂	84
5.4.4 Investigation of the adsorption site of 1,3-BDO on CeO ₂ (111) surface	84
5.4.5 Reaction mechanism of 1,3-diols dehydration	87
5.5 Conclusion	89
6. General conclusions	119

(千葉大学学位申請論文)

**Study on synthesis of valuable
compounds from diols**

2006 年 1 月

千葉大学大学院自然科学研究科
物質高次科学専攻 応用化学講座

市川 尚紀

Chapter 1

General introduction

1.1 Importance in the transformation of chemicals

Nowadays, chemical industry is essential to modern living of human beings because it supplies various products to our life through many other industries. The transformation of the chemical resources into various compounds is the essences of chemical industries. The chemical industry has been employed fossil fuels such as coal, petroleum, and natural gas as the resources for the production of several chemical compounds. For example, the mixture of CO and H₂, which can be obtained by partial oxidation of coal and methane, is an important raw material for the production of methanol [1-5], aldehydes via hydroformylation of olefins [1,6], and hydrocarbons including gasoline and diesel fuels via Fischer-Tropsch process [1,7,8]. Olefins, alcohols, aromatics as well as synthesis gas are basic raw materials for the conversion of chemical compounds into variable ones [1]. The application of the chemical resources derived from petroleum and natural gas, however, will be limited because of their exhaustion.

Therefore, the transformation of the renewable and recyclable resources has an attractive attention. Ethanol derived from fermentation, namely bioethanol, is one of the potential resources. Recently, the coupling of ethanol into 1-butanol was presented over alkali-modified zeolite [9], MgO [10] and calcium phosphate [11]. In our laboratory, the effective transformation of ethanol into ethyl acetate over heterogeneous Cu catalyst via dehydrogenative coupling reaction was investigated [12-14].

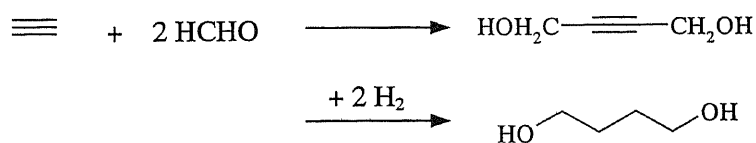
The dehydration and dehydrogenation of alcohols give corresponding olefins and carbonyl compounds, respectively, and are also important reactions in organic

synthesis. Diols, which have two OH groups within its molecule, have been widely used in the field of organic and polymer chemistry. However, the simple dehydration and dehydrogenation of diols have been rarely investigated, while the dehydrogenation of 1,4-butanediol over Cu-based catalyst has been already industrialized to produce γ -butyrolactone [1]. This reaction, however, has not been deeply studied from the mechanistic view point; the effects of catalyst component and reaction pathway from the reactant to the products. The dehydration of 1,3-diols is recently investigated in our laboratory, and it is effective for the production of unsaturated alcohols using CeO_2 catalyst [15,16]. However, the reason why CeO_2 is the efficient catalyst for the dehydration of 1,3-diols is not clarified. It is essential for the improvement of the catalytic performance to clarify the reaction mechanism in the dehydration of 1,3-diols over CeO_2 catalyst.

1.2 Synthesis of γ -butyrolactone from 1,4-butandiol

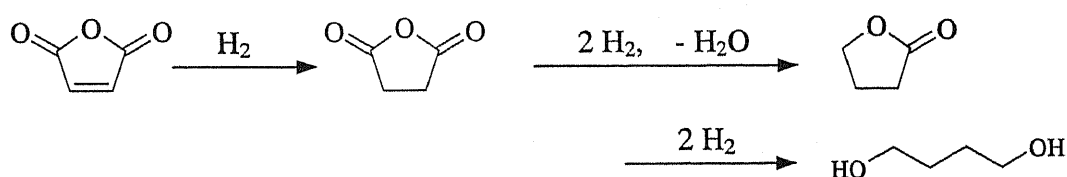
1.2.1 The production of 1,4-butanediol

1,4-Butanediol has been produced by the reaction between acetylene and formaldehyde, namely Reppe process (Scheme 1.1). In this process, acetylene reacts with formaldehyde at 100-110 °C and 0.5-2 MPa to produce 2-butyn-1,4-diol. The produced diol is hydrogenated under high pressure at 20-30 MPa to produce 1,4-butanediol [1]. The use of expensive acetylene and tight reaction conditions are the disadvantages of Reppe process.



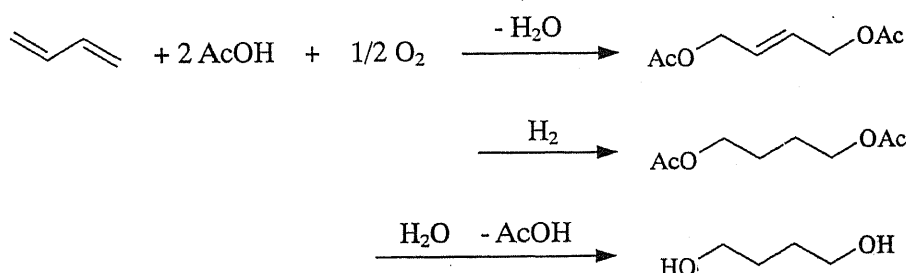
Scheme 1.1 1,4-Butanediol production via Reppe process

The production of 1,4-butanediol by the hydrogenation of maleic anhydride, so-called Kvaerner process, is also commercialized (Scheme 1.2) [1]. This process has been focused on due to the less expensive maleic anhydride. Maleic anhydride, however, is produced by partial oxidation of benzene, butenes and *n*-butane [1], and complete oxidation of the reactant into CO₂ is inevitable. The CO₂ emission is not preferable in the view of green chemistry because of its high green house effect [17], which is the disadvantage of the Kvaerner process.



Scheme 1.2 Reaction pathway from maleic anhydride to 1,4-butanediol (Kvaerner)

Recently, however, brand-new process for 1,4-butanediol production was industrialized by Mitsubishi Chemical Co. Ltd., Japan [1,18]. In the process, 1,3-butadiene and acetic acid are employed as a resource, and 1,4-butanediol is synthesized through the following sequence; acetoxylation of butadiene at 70 °C and 70 bar over Pd/C catalyst modified with Te, hydrogenation at 50 °C and 50 bar over Pd/C, and hydration on acidic ion exchanged resin (Scheme 1.3).

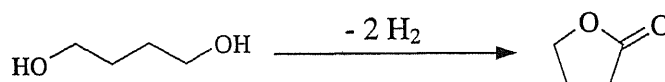


Scheme 1.3 1,4-Butanediol production via process developed by Mitsubishi Chemical Corporation

The application of 1,4-butanediol is summarized in Table 1.1 [1]. 1,4-Butanediol is mainly used as a raw material for THF in USA and Western Europe. In Japan, however, it is used for the production of plastics such as polybutylene terephthalate (PBT). Here, the production capacity of 1,4-butanediol by prime chemical firms is listed in Table 1.1. The Reppe process is still the predominant method for the production of 1,4-butanediol in the world.

1.2.2 Synthesis of γ -butyrolactone

γ -Butyrolactone is an important compound because of its use as solvent and the intermediate of 2-pyrrolidone. In 1996, about 6000 tones of γ -butyrolactone are produced in Japan [1]. In the industrial processes, γ -butyrolactone is synthesized via two routes; one is the hydrogenation of maleic anhydride (Scheme 1.2) and another is the dehydrogenation of 1,4-butanediol (Scheme 1.4). In the former process, γ -butyrolactone is obtained as the intermediate of the hydrogenation of maleic anhydride into 1,4-butanediol, as mentioned in the previous section. The hydrogenation of γ -butyrolactone into 1,4-butanediol, however, requires high temperature at 250 °C and pressure at 10 MPa [1].



Scheme 1.4 Reaction of 1,4-butanediol to γ -butyrolactone

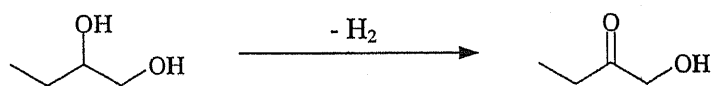
The latter process is carried out under mild conditions and is greener than the former one because of the large amount of CO₂ emission in the former process, as mentioned previously. Thus, it is considered that the dehydrogenation of 1,4-butanediol into γ -butyrolactone is the promising process. In the heterogeneous

system, copper-based catalysts are usually employed for the process.

1.3 Catalytic reactions of 1,3-butanediol over catalysts

1.3.1 Dehydrogenation of 1,3-butanediol over metal catalysts

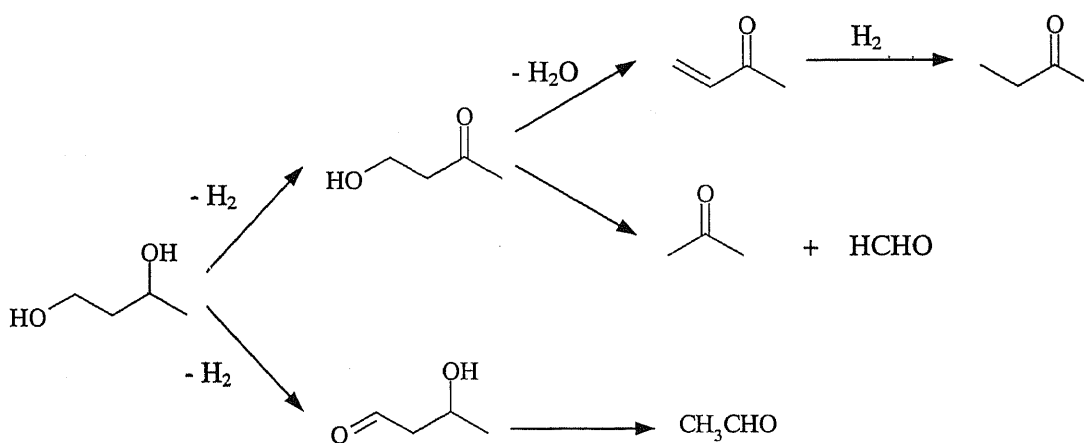
Cu-based catalysts have high dehydrogenation and hydrogenation ability. In the dehydrogenation of 1,2-diols over Cu-based catalysts, dehydrogenation at 2-position OH group preferably proceeded and produced β -ketoalcohols, whereas that at 1-position OH group hardly proceeded [19]. For example, 1,2-butanediol is selectively dehydrogenated over Cu-based catalyst to produce 1-hydroxy-2-butanone with its selectivity of 98.1 mol% at the conversion of 50.0 % (Scheme 1.5) [19].



Scheme 1.5 Reaction of 1,2-butanediol to 1-hydroxy-2-butanone

In the dehydrogenation of 1,3-butanediol, the selective dehydrogenation of OH group at 3-position of 1,3-butanediol produces 4-hydroxy-2-butanone, which is used as an intermediate for the production of 3-buten-2-one. 4-Hydroxy-2-butanone is manufactured by the aldol reaction of propanone and formaldehyde [20,21]. Because of the instability and toxicity of formaldehyde, another process to produce 4-hydroxy-2-butanone is expected. The selective dehydrogenation of 1,3-butanediol into 4-hydroxy-2-butanone is a potential process to take the place of the present one. In our laboratory, the dehydrogenation of 1,3-butanediol over Cu-based catalysts was carried out [22]. Table 1.3 shows the reaction results of 1,3-butanediol over several Cu-based catalysts. The catalysts with high surface area such as Cu/Al₂O₃ and Cu/ZrO₂ exhibit high activity. The selectivity to 4-hydroxy-2-butanone, however, is

quite low due to the large amount of production of butanone. Butanone would be produced via dehydration of 4-hydroxy-2-butanone to 3-buten-2-one, which is consecutively hydrogenated into butanone. Propanone would be formed by the decomposition of acetaldol, which is produced by the dehydrogenation of OH group at 1-position in 1,3-butanediol. The side reaction prefers high reaction temperature as 300 °C. The probable reaction pathway from 1,3-butanediol to products is summarized in Scheme 1.6. The 4-hydroxy-2-butanone selectivity is high over the catalyst with low surface area such as Cu, Cu/ZnO and N-211, while they show low activity. Fig. 1.1 shows the relation between 1,3-butanediol conversion and the selectivity to 4-hydroxy-2-butanone and butanone. The selectivity to 4-hydroxy-2-butanone decreasing with increasing the conversion, while that to butanone decreases with it. This result supports that butanone is produced via the consecutive reaction of 4-hydroxy-2-butanone. At this point, it seems to be still difficult to produce 4-hydroxy-2-butanone from 1,3-butanediol over Cu-based catalyst.



Scheme 1.6 Probable reaction pathway from 1,3-butanediol to product over Cu-based catalyst

1.3.2 *Dehydration of 4-hydroxy-2-butanone into 3-buten-2-one*

3-Buten-2-one is an intermediate of steroids, terpenoids, medical drugs and pesticides and thus is an important compound in industrial chemistry.

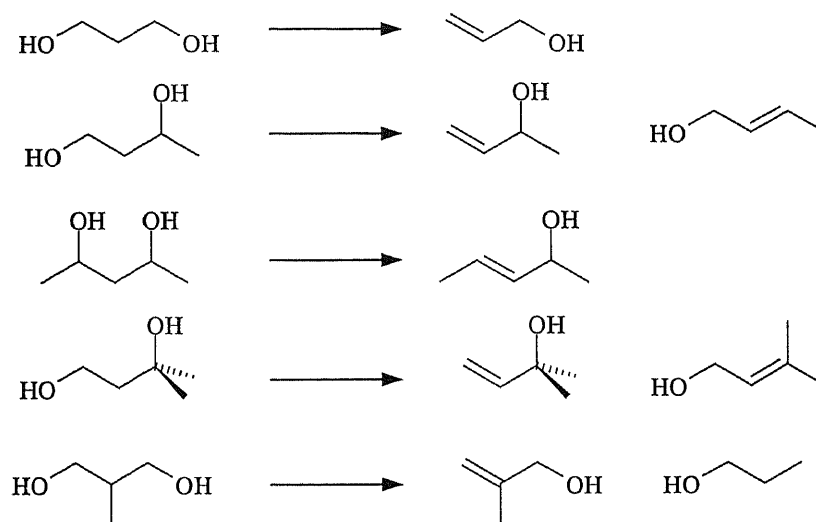
3-Buten-2-one has been produced from 4-hydroxy-2-butanone with aqueous acid catalysts such as sulfuric acid and phosphoric acid. These homogeneous catalysts need to be removed from products by neutralization with base after the reaction, and production of large amount of solid waste is inevitable. From the viewpoint of green chemistry, the production of by-products should be reduced [17]. Heterogeneous catalysts have an advantage in the problem: the separation of products from catalyst is easy and there is no need to neutralize the heterogeneous catalyst.

1.3.3 *Dehydration of 1,3-butanediol over metal oxide catalysts*

1,3-Butanediol is produced via aldol reaction of acetaldehyde followed by the hydrogenation of the produced acetaldol [1]. 1,3-Butanediol is widely applied as a raw material of plastics, solvent, elasticizer, humectant and so on. The reaction of 1,3-butanediol for the synthesis of organic compounds is rarely investigated. In our laboratory, it was found that CeO_2 catalyzed 1,3-diols into unsaturated alcohol at 325 °C, while 1,3-diols with substituent at 2-position are less reactive (Scheme 1.7) [16]. The reaction of diols over CeO_2 is listed in Table 1.4.

As has been investigated, other metal catalysts with high acidity and basicity are not good catalyst for the selective dehydration of 1,3-diols because they catalyzed it into gaseous products, mainly dienes, and catalysts with moderate acid-base property and lanthanide oxides other than CeO_2 are inactive for 1,3-butanediol [15]. However, the relation between the catalytic performance and its acid-base property was not deeply studied.

The reaction mechanism and active site of the reaction of 1,3-diols was not also investigated. It is speculated that the reaction proceeds with redox mechanism, and redox property of CeO_2 would play an important roll in the catalysis: initially, the 2-position H is abstracted as radical by Ce^{4+} and H radical donates one electron to



Scheme 1.7 Reaction of diols over CeO_2

reduce Ce^{4+} to Ce^{3+} and H itself is oxidized to proton, followed by the abstraction of one of OH group from 1,3-diols to give unsaturated alcohols [16,23].

1.4 Constitution of this thesis

In the following chapters, the reaction of diols over heterogeneous catalysts will be discussed. In the dehydration of 1,4-butanediol over Cu-based catalyst, the study on the copper loading, effect of supports on catalytic performance, and reaction pathway from 1,4-butanediol to γ -butyrolactone has not been clarified yet. Thus, in Chapter 2, the dehydrogenation of 1,4-butanediol into γ -butyrolactone over copper-based catalyst is investigated. The effect of the catalyst component on catalytic performance and the reaction pathway from 1,4-butanediol to γ -butyrolactone will be

discussed.

In Chapter 3, the dehydration of 4-hydroxy-2-butanone, which can be obtained by dehydration of 1,3-butanediol, into 3-buten-2-one is investigated. The optimization of catalyst for the reaction and reaction conditions, and acid property of the catalyst that plays a crucial role in catalysis will be discussed.

In Chapter 4, the dehydration of 1,3-butanediol over metal-oxide catalysts with different acid and base property is investigated to clarify the effect of it on catalysis. The correlation between the property of catalysts and product distribution will be discussed.

In Chapter 5, the reaction of 1,3-butanediol over CeO_2 catalyst will be discussed. Preliminarily, quantum calculation based on Paired Interactive Orbital theory was employed to prove the reaction mechanism with the assumed adsorption structure on oxygen-defect site of $\text{CeO}_2(111)$ surface, and it was observed that the repulsive overlap of orbitals between C and H atoms at 2-position induced by the interaction between Ce cation and H atom at 2-position [23]. However, the above result has some disadvantages: the adsorption model employed in the calculation was only “assumed” one, and it is not clear that reaction actually proceeds at the oxygen-defect site of $\text{CeO}_2(111)$ surface. Considering the issues mentioned above, the active site of 1,3-butanediol dehydration, adsorption structure of 1,3-butanediol on CeO_2 surface and reaction mechanism of 1,3-butanediol into unsaturated alcohols will be discussed.

References in Chapter 1

- [1] K. Weissmehl, H.-J. Arpe, *Industrial Organic Chemistry, 4th ed.*, Wiley-VCH, 2003.

- [2] A. B. Stiles, *AIChE J.* **23** (1977) 362-375.
- [3] C. J. Schack, M. A. McNeil, R. G. Rinker, *Appl. Catal.* **50** (1989) 247-263.
- [4] M. A. McNeil, C. J. Schack, R. G. Rinker, *Appl. Catal.* **50** (1989) 265-285.
- [5] G. C. Chinchin, K. C. Waugh, D. A. Whan, *Appl. Catal.* **25** (1986) 101-107.
- [6] P. W. N. M. van Leeuwen, C. Claver, *Rhodium Catalyzed Hydroformylation*, Kluwer Academics Publishers, Dordrecht (2000).
- [7] M. E. Dry, *Appl. Catal. A* **138** (1996) 319-344.
- [8] M. E. Dry, *J. Chem. Technol. Biotechnol.* **77** (2001) 43-50.
- [9] C. Yang, Y. Z. Meng, *J. Catal.* **142** (1993) 37-44.
- [10] A. S. Ndou, N. Plint, N. J. Coville, *Appl. Catal. A* **251** (2003) 337-345.
- [11] *Japan Kokai Tokkyo Koho*, JP H11-217343.
- [12] K. Inui, T. Kurabayashi, S. Sato, *Appl. Catal. A* **237** (2002) 53-61.
- [13] K. Inui, T. Kurabayashi, S. Sato, *J. Catal.* **212** (2002) 207-215.
- [14] K. Inui, T. Kurabayashi, S. Sato, N. Ichikawa, *J. Mol. Catal. A* **216** (2004) 147-156.
- [15] S. Sato, R. Takahashi, T. Sodesawa, N. Honda, H. Shimizu, *Catal. Commun.* **4** (2003) 77-81.
- [16] S. Sato, R. Takahashi, T. Sodesawa, N. Honda, *J. Mol. Catal. A* **221** (2004) 177-183.
- [17] P. T. Anastas, J. C. Warner, *Green Chemistry: Theory and Practice*, Oxford University Press, 1998.
- [18] H. Ohno, *Shokunai (Japanese)* **42** (2000) 46-50.
- [19] S. Sato, R. Takahashi, T. Sodesawa, H. Fukuda, T. Sekine, E. Tsukuda, *Catal. Commun.*, **6** (2005) 607-610.
- [20] *Japan Kokai Tokkyo Koho*, JP S52-128311.
- [21] J. T. Hays, G. F. Hager, H. M. Engelmann, H. M. Spurlin, *J. Am. Chem. Soc.*, **73**

(1951) 5369-5373.

[22] Master thesis, H. Fukuda, Chiba University.

[23] N. Ichikawa, S. Sato, R. Takahashi, T. Sodesawa, *J. Mol. Catal. A* **231** (2005) 181-189.

Table 1.1 Application of 1,4-butanediol

Area	Year	Products ^a (%)					Total use / 1000 tones
		THF	AC	PBT	PU	Others	
USA	1994	51	20	20	6	3	289
	2000	36	18	32	12	2	640
Western Europe	1992	35	16	20	23	6	104
	1997	36	15	24	20	5	140
Japan	1991	12	-	66	16	6	38
	1997	28	-	55	4	13	67

^a The abbreviation of the products are as follows; THF: tetrahydrofuran, AC: acetylene chemicals (vinyl esters, ethers, butanone and so on), PBT: polybutylene terephthalate, PU: polyurethane.

Table 1.2 The production capacity of 1,4-butanediol in 1999 ^a

Area	Producer	Capacity / tones year ⁻¹	Method
Asia			
(Japan)	Mitsubishi Chemical	50,000	Mitsubishi Chemical
	BASF / Idemitsu	25,000	Reppe
	Tonen Chemical	30,000	Kvaerner
(Korea)	Shinwa	20,000	Kvaerner
(Taiwan)	Dairen	30,000	Oxo ^b
USA	ISP	35,000	Reppe
	DuPont	110,000	Reppe
	BASF	125,000	Reppe
Euro	BASF	160,000	Reppe
	ISP	90,000	Reppe

^a Data cited from Ref. [18].

^b Method by the hydroformylation of allyl alcohol.

Table 1.3 Reaction of 1,3-butanediol over Cu-based catalysts ^a

Catalyst ^b	S _{ABET} ^c / m ² g ⁻¹	S _{A_{Cu}} ^d / m ² g ⁻¹	Conv. / %	Selectivity ^e / mol%			
				HB	MEK	AcH	AcMe
Cu	1.2	1.2	40.8	55.9	6.1	2.7	17.8
Cu / ZnO	5.5	5.6	66.3	55.5	19.9	1.7	9.2
Cu / Al ₂ O ₃	113.6	39.5	98.4	2.6	51.5	3.6	15.5
Cu / ZrO ₂	53.8	16.7	99.4	7.1	50.1	3.9	19.6
N-211	38.0	-	77.7	51.4	24.8	3.8	7.6

^a The reaction conditions are as follows; catalyst weight: 0.100 g, 1,3-butanediol feed rate: 1.8 cm³ h⁻¹, carrier gas flow rate (He): 30 cm³ min⁻¹, reaction temperature: 240 °C. Prior to the reaction, the catalysts are reduced in H₂ flow at 300 °C for 1 h.

^b All the samples except for N-211 are prepared by co-precipitation method. The ratio of Cu to support is fixed at 3 in molar in all the samples. N-211 is commercially available catalyst supplied by Nikki Chemical Co., Ltd. whose composition is Cu : ZnO = 49.3 : 45.1 in weight.

^c Specific surface area.

^d Copper surface area.

^e The abbreviation of the products are as follows; HB: 4-hydroxy-2-butanone, MEK: butanone, AcH: acetaldehyde, AcMe, propanone.

Table 1.4 Reaction results of diols over CeO₂^a

Reactant	Conv ^b / %	Product ^c
1,2-butanediol	6.4	butanone (14)
1,3-butanediol	36.9	3-buten-2-ol (56.9), <i>trans</i> -2-buten-1-ol (2.2), <i>cis</i> -2-buten-1-ol (1.8)
1,4-butanediol	2.6	3-buten-1-ol (84)
1,3-propanediol	50.6	2-propen-1-ol (98.9)
2,4-pentanediol	47.2	<i>trans</i> -3-penten-2-ol (86.8), <i>cis</i> -3-penten-2-ol (7.4), 1,3-pentadiene (1.4)
3-methyl-1,3-butanediol	42.3	2-methyl-3-buten-2-ol (56.8), 3-methyl-2-buten-1-ol (24.7)
2-methyl-1,3-propanediol	6.8	2-methyl-2-propen-1-ol (61), 1-propanol (23), propanal (6), 2-methylpropanol (7)
2-ethyl-1,3-hexanediol	19.0	2-ethyl-1-hexen-3-ol (54.1), 2-ethyl-2-hexen-1-ol (22.5)
1,2,3-propanetriol	3.9	1-hydroxy-2-propanone (50)

^a Data cited from Ref. [7].

^b Reaction conditions are as follows; catalyst: CeO₂ with specific surface area of 20 m² g⁻¹, catalyst weight: 0.15 g, reactant feed rate: 2.01 cm³ h⁻¹, carrier gas flow rate (N₂): 73 mmol h⁻¹.

^c The number in parenthesis indicates the selectivity.

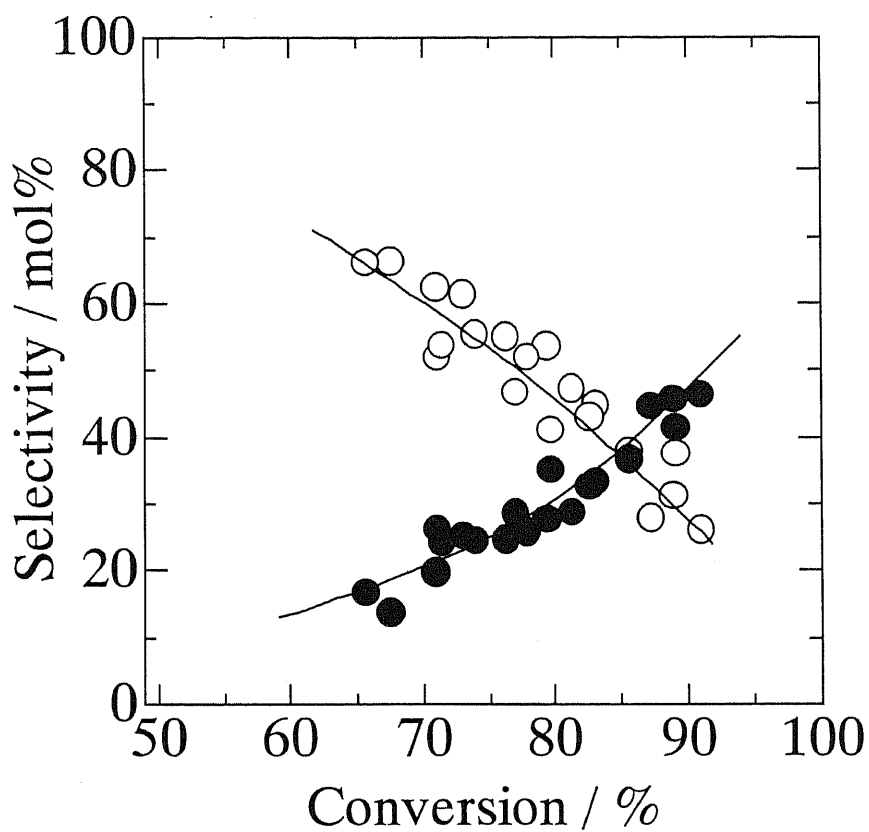


Fig. 1.1 Relation between 1,3-butanediol conversion and selectivities at 240 °C. The reaction was carried out under several conditions in order to change the conversion. The selectivity to (○) 4-hydroxy-2-butanone, (●) butanone.

Chapter 2

Dehydrogenative cyclization of 1,4-butanediol over copper-based catalyst

2.1 Introduction

In Section 1.2.2, the advantages of γ -butyrolactone (hereafter abbreviated as GBL) production via the dehydrogenation of 1,4-butanediol (1,4-BDO) are mentioned, compared to the successive hydrogenation of maleic anhydride; mild reaction conditions and low-level emission of CO₂. In the hydrogenation of maleic anhydride into GBL, three moles of hydrogen molecules are necessary in order to produce one mole of GBL (Scheme 2 in Chapter 1), and the reaction is carried out under high-pressure condition. In this process, metal-based catalysts such as Cu, Pd and Ru are employed [1-6].

Both homogeneous [7-9] and heterogeneous catalysts [10-13] are used for the dehydrogenation of 1,4-BDO into GBL. In the heterogeneous system, Cu-based catalysts are mainly employed [10-13]. However, the effects of the metal-oxide additives on catalytic performance and reaction pathway from 1,4-BDO to GBL have not been clarified yet.

Therefore, in this chapter, the effects of additives of copper-based catalyst such as ZnO, ZrO₂, and Al₂O₃ on the catalytic activity are discussed, and the reaction pathway from 1,4-BDO to GBL is also investigated using reactions of several substrates such as tetrahydrofuran (THF), 2-hydroxytetrahydrofuran (2HTHF), and succindialdehyde (SDA), which are possible intermediates.

2.2 Experimental

2.2.1 Catalyst preparation

Catalyst samples were prepared by a conventional coprecipitation method. Three metal oxides, ZnO, ZrO₂ and Al₂O₃, were employed as additives. The detailed procedure was described elsewhere [14]. Hereafter, the catalyst composition of CuO: ZnO: ZrO₂: Al₂O₃ = *a*: *b*: *c*: *d* was abbreviated as *A-abcd*. For example, a catalyst name of “A-6122” means its molar ratio of CuO: ZnO: ZrO₂: Al₂O₃ = 6: 1: 2: 2. Tables 2.1-2.3 list the physical properties of specific surface area and Cu metal surface area [14]. The details of the measurement of Cu surface area is described elsewhere [15].

2.2.2 Preparation procedure of 2HTHF and SDA

2HTHF was synthesized as referring [16,17]. The details are as follows. A mixture of 2,3-dihydroxytetrahydrofuran and the four-fold volume of 0.1 mol dm⁻³ of HCl solution was heated about 60 °C for 1 h with reflux-condenser. Heating at higher temperature and longer reaction period would lower the yield of 2HTHF probably because of oligomerization. After the reaction, the mixture was cooled to ambient temperature and neutralized with 0.2 mol dm⁻³ of NaOH solution. 2HTHF was distilled under reduced pressure and remaining water was removed by drying over anhydrous Na₂SO₄. The purity of 2HTHF exceeded 94 % in GC.

SDA was synthesized as modifying the procedure described in Ref. [18]: 2,5-dimethoxytetrahydrofuran and the four-fold volume of 0.1 mol dm⁻³ of HCl solution were mixed in a flask and heated at 95 °C for 3 h with reflux-condenser. Then, the reaction mixture was cooled to ambient temperature and neutralized with 0.2 mol dm⁻³ of NaOH solution, followed by distillation under reduced pressure. Since

high concentrated SDA solution was solidified, SDA was collected by distillation in aqueous solution at low concentration. The concentration of SDA in the solution was 21.0 wt %.

2.2.3 Catalytic reaction

The reaction of 1,4-BDO to GBL was performed in a fixed-bed down-flow glass reactor at 200-300 °C under atmospheric pressure in He flow of 30 cm³ min⁻¹. Prior to the reaction, the catalyst was reduced by H₂ at the flow rate of 30 cm³ min⁻¹ at 300 °C for 1 h. After the reduction, the catalyst bed was cooled to the reaction temperature, and the carrier gas was switched to He. The effluent was collected periodically for 5 h at 0 °C, and analyzed by FID-GC (Shimadzu GC-8A) using a 30-m capillary column of TC-WAX (GL Science, Japan). No gaseous products except H₂ were detected during the reaction with on-line TCD-GC. A typical reaction was carried out under the condition at 240 °C and $W/F = 0.083 \text{ g h cm}^{-3}$ where W and F are catalyst weight and reactant feed rate, respectively.

The reactions of 2HTHF and SDA over several catalyst samples were carried out at 240 °C with the same procedure described above. Either 2HTHF with 94 % purity or SDA 21.0 wt % solution was introduced over the fresh catalyst for 1 h in the reactions because of small quantity of produced 2HTHF and SDA.

2.3 Results

Table 2.1 summarizes the effects of additives on both the physical and catalytic properties of copper-based catalysts. Both specific surface area and Cu surface area decrease as following order: A-3001 > A-3010 > A-3100 [14]. All the samples were slightly deactivated during the initial reaction for 5h. Thus, the

catalytic data were average activity between 0 and 5 h. Over A-3001 sample, for example, the conversion of 1,4-BDO and selectivity to GBL in the initial period for 1 h was 71.8 and 97.3 mol%, respectively. At the final period between 4 and 5 h, they decreased to 63.3 and 96.1 mol%, respectively. The cause of deactivation would be the deposition of carbon species onto the catalyst surface, because the deactivated catalyst recovered its initial activity after the oxidizing treatment at 500 °C. In addition to the majority of GBL, THF, 2HTHF and some unidentified products were detected in effluent. However, I should note that 4-hydroxybutanal and SDA were not detected within the detection limit. GBL was formed even in the reaction over A-3000, which is pure Cu without additives. As shown in Table 2.1, no clear correlation between catalytic activity and Cu surface area was observed in the binary system. Over A-3001, the conversion of 1,4-BDO was not so high in spite of its high surface area, and THF was observed with relatively high selectivity. A-3010 showed the highest conversion of 1,4-BDO and selectivity to GBL in the binary systems. A-3100 was less active than A-3000, and 2HTHF was observed with high selectivity.

Table 2.2 summarizes the effects of ZnO and/or ZrO₂ added to A-3001 on both the physical and catalytic properties. Both specific surface area and Cu surface area were maintained their high values after the addition of ZnO and ZrO₂ to A-3001. It was also observed that the addition of ZnO and ZrO₂ increased the conversion of 1,4-BDO and it decreased the selectivity to THF together with increasing GBL yield. A-6222, containing both ZnO and ZrO₂, showed similar activity to that of A-6022, while A-6122 showed much higher activity than A-6222.

Table 2.3 summarizes the physical and catalytic properties of A-x122 (x = 0–95). Specific surface area decreased monotonically with increasing the copper content. Cu content did not affect Cu surface area around 40 m² g⁻¹. THF was

selectively produced at $x = 0$, where there is no copper. The production of THF, however, drastically suppressed at $x = 1$ and the selectivity to GBL increased. The catalytic activity was enhanced with increasing Cu content, and the highest catalytic activity, 84.0 % 1,4-BDO conversion and 97.7 mol% GBL selectivity, was obtained at $x = 6$ (A-6122).

Figs. 2.1 and 2.2 show changes in the conversion of 1,4-BDO and in the selectivity to GBL and 2HTHF with W/F over A-6122 at reaction temperature range between 200 and 300 °C, respectively. At any reaction temperature, the 1,4-BDO conversion and the GBL selectivity increased with increasing W/F value, while the 2HTHF selectivity decreased. Fig. 2.3 shows changes in the conversion of 1,4-BDO and the selectivity to GBL and 2HTHF with W/F value over a less active A-3100 at 240 °C. It was confirmed that high selectivity to 2HTHF is attained at low 1,4-BDO conversion. The GBL selectivity increased with decreasing the 2HTHF selectivity.

Table 2.4 summarizes the dehydrogenation of 2HTHF over several Cu-based catalysts and support (A-0122). 2HTHF was dehydrogenated to GBL over all the samples. The catalytic activity was quite different: the A-3001, A-3010 and A-3111 samples showed much higher activity than A-0122, A-3000 and A-3100 samples.

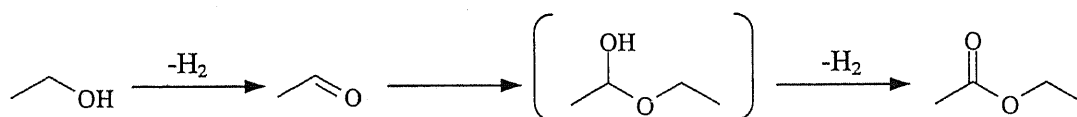
Table 2.5 summarizes the transformation of SDA in different atmosphere of He and H₂. Over the non-copper sample (A-0122), a small amount of SDA was transformed to GBL in both atmospheres, and the catalytic activity was not affected by carrier gas. Other products, 2HTHF and 1,4-BDO, were also observed. In contrast, Cu-based catalysts had little activity in He flow, whereas they effectively transformed SDA to GBL in H₂ flow. This result implies that the formation of GBL from SDA requires hydrogenation at the first step of the transformation.

2.4 Discussion

2.4.1 Effects of additives on the physical and catalytic property

A-3000 catalyst, pure copper, showed ability of dehydrogenative cyclization (Table 2.1). On the other hand, A-0122 containing no copper was active to dehydrative cyclization to THF. Therefore, metallic Cu is active center of dehydrogenation of 1,4-BDO to GBL. However, no simple correlation between catalytic activity and Cu surface area was observed (Tables 2.1-2.3). Hence, the catalytic activity would be greatly influenced by the additives.

In the reaction of ethanol to ethyl acetate [14,19], the reaction pathway was considered as shown in Scheme 2.1. Ethanol was initially dehydrogenated to acetaldehyde, followed by hemiacetalization of ethanol with acetaldehyde. The hydroxyl group of hemiacetal compound, which was not detected in the reaction effluent, was consecutively dehydrogenated to ethyl acetate.



Scheme 2.1 Reaction pathway from ethanol to ethyl acetate over the copper-based catalyst. A compound in the parenthesis is not observed in the ethyl acetate formation.

The effects of additives on the direct synthesis of ethyl acetate from ethanol are summarized in Ref. [14]. Al₂O₃ increased Cu surface area, and enhanced the catalytic activity. The high dispersion of Cu species would be attributed to the insertion of aluminum ions into CuO lattice to decrease CuO particle size. However, a large amount of diethyl ether formation was observed in Cu-Al₂O₃ system such as A-3001. ZrO₂ greatly increased the catalytic activity. ZnO did not affect both the Cu surface area and catalytic activity. The addition of ZnO and ZrO₂ to A-3001

suppressed the diethyl ether formation. The decrease in the selectivity to diethyl ether would be attributed to neutralization of acid sites of Al_2O_3 surface with ZnO and ZrO_2 . In the reaction of ethanol to ethyl acetate over the quaternary system, A-x122, diethyl ether was observed at low copper content, whereas it disappeared at high copper content. The formation of diethyl ether was attributed to the isolated Al_2O_3 species, which was not incorporated into CuO lattice. At low copper content, aluminum ion was not incorporated into CuO lattice completely. Thus, the isolated Al_2O_3 species existing over catalyst surface catalyze the etherification of ethanol to diethyl ether. The content of copper in A-x122 sample affects the catalytic activity, and the highest activity is observed at $x=12$.

In the present reaction of 1,4-BDO to GBL, effects of additives on catalytic activity are similar to those observed in the ethyl acetate formation (Tables 2.1-2.3). While ZnO did not affect the catalytic activity, ZrO_2 drastically enhanced it. THF was formed over A-3001 sample in place of diethyl ether formed in the reaction of ethanol. Rao *et al.* reported that 1,4-BDO interacted with Brønsted acid site of Cr-ZSM-5 and was dehydrated to THF [20]. It is probable that THF would be formed over acidic sites of Al_2O_3 . The formation of THF over A-3001 sample was greatly suppressed by the addition of ZnO and ZrO_2 . The catalytic activity was enhanced in the quaternary system. In the A-x122 systems, THF was preferentially formed at $x=0$, whereas it was greatly suppressed by the addition of copper, which would reduce acidic property. The highest activity was obtained at $x=6$.

2.4.2 Kinetic consideration

In the reaction of 1,4-BDO to GBL, the reaction pathway would be similar to that of ethanol to ethyl acetate (Scheme 2.1). The variations in the selectivity to GBL

and 2HTHF shown in Figs. 2.1-2.3 suggest that 2HTHF is the intermediate in the GBL synthesis from 1,4-BDO. The reaction of 1,4-BDO to GBL is simply regard as the consecutive reaction via 2HTHF as following:



The reaction rate constants of the steps, 1,4-BDO to 2HTHF and 2HTHF to GBL, were denoted as k_1 and k_2 , respectively. The relation between conversion and selectivity was simulated, assuming that the elementary reaction of each step has first order. In general, the change in the composition of 1,4-BDO, 2HTHF and GBL in the consecutive reaction can be expressed as follows [21]:

$$X_A = \exp(-k_1 t)$$

$$X_B = [k_1 / (k_1 - k_2)] [\exp(-k_2 t) - \exp(-k_1 t)]$$

$$X_C = 1 - X_A - X_B$$

where t , X_A , X_B and X_C are the time factor, the composition of 1,4-BDO, that of 2HTHF and that of GBL, respectively. Eliminating the time factor, the selectivity to 2HTHF as the function of the conversion of 1,4-BDO was obtained, as the following equation

$$y = (1/x) / (1 - k_2/k_1) [(1-x)^{k_2/k_1} - (1-x)]$$

where x and y represent the conversion of 1,4-BDO, $x = 1 - X_A$, and the selectivity to 2HTHF, $y = X_B / (1 - X_A)$, respectively. The selectivity to GBL is expressed as $1 - y$.

Then, the theoretical selectivity-conversion curve can be calculated at appropriate ratio of k_2 to k_1 , k_2/k_1 , which is the variable. Figs. 2.4 and 2.5 show the relation between the conversion and selectivity over A-6122 and A-3100, respectively, together with the theoretical curves at several k_2/k_1 values. The curves calculated with the k_2/k_1 value at 48 and 8 well fit with the plotted data of Figs. 2.4 and 2.5,

respectively. The results indicate that the reaction rate of the second step is 48 times faster than that of the first step over A-6122, whereas it is 8 times faster over A-3100. Therefore, the addition of ZnO into Cu catalyst greatly decreased the dehydrogenation ability, especially in the second step. In the reduction of A-3100, ZnO could be partially reduced with Cu, to be bimetal solid solution. This would be the reason for the deactivation over A-3100. This consideration is consistent with the result shown in Table 2.4: A-3100 is less active than the others in the dehydrogenation of 2HTHF to GBL.

The initial step, the reaction from 1,4-BDO to 2HTHF, includes two elementary reactions, which involve the dehydrogenation of 1,4-BDO to 4-hydroxybutanal and hemiacetalization of 4-hydroxybutanal to 2HTHF. In the step, the hemiacetalization would much faster than dehydrogenation because 4-hydroxybutanal was not observed in the reaction of 1,4-BDO to GBL. Therefore, it is considered that the dehydrogenation of 1,4-BDO to 4-hydroxybutanal is the rate-determination-step in the total GBL formation.

2.4.3 Reaction pathway from 1,4-BDO to GBL

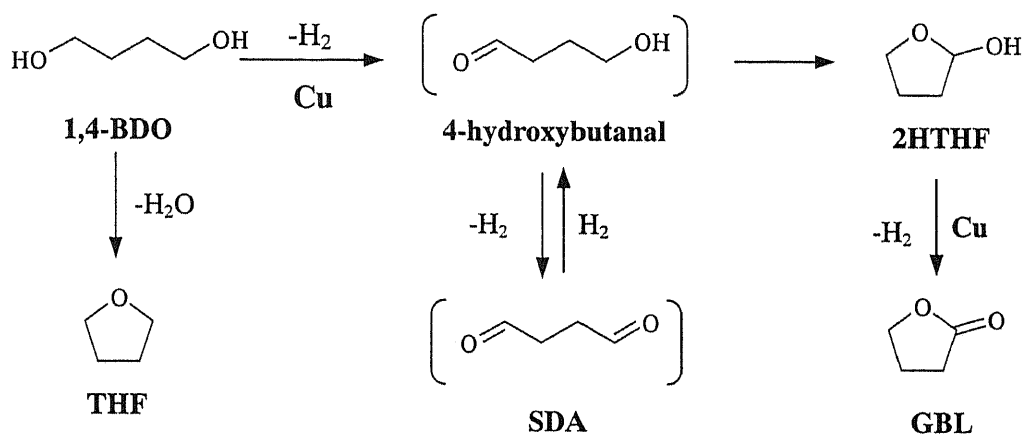
As shown in Table 2.4, 2HTHF was dehydrogenated to GBL over any samples. The catalytic activity, however, is quite different among the samples. In the A-0122 and A-3000 samples, the yield of GBL is almost the same in spite of specific surface area of A-0122 sample being more than 150 times higher than the Cu surface area of A-3000 (Table 2.1). This means that the dehydrogenation of 2HTHF mainly proceeds over metallic Cu surface. In the binary systems, A-3100 is less active than A-3010 and A-3001 samples. This is probably caused by not only their Cu surface area but also effects of additive mentioned in the previous section.

Although it is elucidate that 2HTHF is the intermediate in the reaction of 1,4-BDO to GBL, other possible reaction pathways, partial oxidation of THF and Tishchenko reaction, are still remained. In the partial oxidation of THF, the oxygen source would be bulk oxygen in metal oxide of additives and/or oxygen in H₂O, which was generated during the dehydration of 1,4-BDO to THF. Neither pure THF nor 50 mol% aqueous THF solution was reacted even over the most reactive A-6122 in He flow. Hence, the possibility of partial oxidation of THF to GBL is denied in the present system.

Then, it was examined whether Tishchenko reaction would proceed over the samples or not. The fact that a small amount of SDA is transformed to GBL in both atmospheres of He and H₂ over A-0122 (Table 2.5) indicates that Tishchenko reaction could proceed over the mixed metal oxides. However, Tishchenko reaction did not occur over the Cu-based catalysts in He flow. It is reported that Tishchenko reaction required both acidic and basic sites [22], and I previously mentioned that Cu addition to A-0122 would suppress the surface acidity [14]. Thus, I speculated that similar suppression would inhibit Tishchenko reaction of SDA to GBL over A-x122 except for A-0122. On the other hand, SDA was transformed to GBL over the Cu-based catalyst in H₂ flow. In H₂, one of formyl groups in SDA would be hydrogenated to be 4-hydroxybutanal. This can be converted to GBL through 2HTHF. In the reaction of SDA in H₂, 1,4-BDO would be formed by the further hydrogenation of 4-hydroxybutanal.

In Scheme 2.2, I summarize the reaction pathway. 1,4-BDO is initially dehydrogenated over metallic Cu surface to 4-hydroxybutanal. Since the existence of 4-hydroxybutanal was not observed within the detection limit, 4-hydroxybutanal is so unstable that it is rapidly hemiacetalized to 2HTHF. 2HTHF is further

dehydrogenated to GBL over metallic Cu surface. 2HTHF is the intramolecular hemiacetal compound of 4-hydroxybutanal. In the reaction of ethanol to ethyl acetate (Scheme 2.1), the existence of hemiacetal was not confirmed, while acetaldehyde was observed in the possible reaction pathway [14]. Here, it can be confirmed that hemiacetal is the intermediate in the dehydrogenative esterification of alcohol.



Scheme 2.2 Reaction pathway from BDO to GBL over Cu-based catalyst. Compounds in the parenthesis are not observed in the BDO reaction.

2.5 Conclusion

Synthesis of γ -butyrolactone from 1,4-BDO was investigated over Cu-Zn-Zr-Al-O catalyst. The relation between catalyst composition and catalytic activity for the GBL synthesis from 1,4-BDO and the reaction pathway were examined. GBL was effectively formed over the Cu-based catalyst. The catalytic activity was greatly affected by additives, and the mixing of metal oxide additives increased catalytic activity, the maximum activity was obtained at catalyst composition of CuO: ZnO: ZrO₂: Al₂O₃ = 6: 1: 2: 2.

The reaction pathway was clarified as follows; 1,4-BDO was initially dehydrogenated to 4-hydroxybutanal, which was rapidly hemiacetalized to 2HTHF.

2HTHF was further dehydrogenated to GBL. All the dehydrogenation occurred over metallic Cu species. The pathways through the partial oxidation of THF and Tishchenko reaction were denied over the copper-based catalysts.

References in Chapter 2

- [1] U. Herrmann, G. Emig, *Ind. Eng. Chem. Res.* **36** (1997) 2885-2896.
- [2] A. Küksal, E. Klemm, G. Emig, *Appl. Catal. A* **228** (2002) 237-251.
- [3] S. M. Jung, E. Godard, S. Y. Jung, K.-C. Park, J. U. Choi, *Catal. Today* **87** (2003) 171-177.
- [4] U. R. Pillai, E. Sahle-Demessie, D. Young, *Appl. Catal. B* **43** (2003) 131-138.
- [5] Y. Hara, H. Kusaka, H. Inagaki, K. Takahashi, K. Wada, *J. Catal.* **194** (2000) 188-197.
- [6] M. Messori, A. Vaccari, *J. Catal.* **150** (1994) 177-185.
- [7] *Japan Kokai Tokkyo Koho*. JP14-233762 (2002).
- [8] S. Murahashi, T. Naota, K. Ito, Y. Maeda, H. Taki, *J. Org. Chem.* **52** (1987) 4319-4327.
- [9] Y. Lin, X. Zhu, Y. Zhou, *J. Organomet. Chem.* **429** (1992) 269-274.
- [10] *Japan Kokai Tokkyo Koho*. JP02-255668 (1990).
- [11] *US Patent*. US5210229 (1993).
- [12] *US Patent*. US6093677 (2000).
- [13] *Japan Kokai Tokkyo Koho*. JP05-286959 (1993).
- [14] K. Inui, T. Kurabayashi, S. Sato, *Appl. Catal. A* **237** (2002) 53-61.
- [15] S. Sato, R. Takahashi, T. Sodesawa, K. Yuma, Y. Obata, *J. Catal.* **196** (2000) 195-199.
- [16] L. Leite, A. Lebedevs, V. Stonkus, M. Fleisher, *J. Mol. Catal. A* **144** (1999)

323-328.

- [17] L. E. Schniepp, H. H. Geller, *J. Am. Chem. Soc.* **68** (1946) 1646-1648.
- [18] A. R. Katritzky, H-Y. He, J. Wang, *J. Org. Chem.* **67** (2002) 4951-4956.
- [19] K. Inui, T. Kurabayashi, S. Sato, *J. Catal.* **212** (2002) 207-215.
- [20] Y. V. Subba Rao, S. J. Kulkarni, M. Subrahmanyam, A. V. Rama Rao, *J. Org. Chem.* **59** (1994) 3998-4000.
- [21] J. M. Smith, *Chemical Engineering Kinetics, 3rd. ed.*, McGraw-Hill, New York, 1981, p. 84.
- [22] H. Hattori, *Appl. Catal. A* **222** (2001) 247-259.

Table 2.1 Effect of additive on physical property and catalytic activity in the dehydrogenative cyclization of 1,4-BDO^a

Catalyst	SA _{BET} ^b / m ² g ⁻¹	SA _{Cu} ^c / m ² g ⁻¹	Conv. / %	Selectivity/ mol %		
				GBL	THF	2HTHF
A-3000	1.2	1.2	27.6	88.9	0	9.6
A-3100	5.5	5.6	25.7	66.4	0.5	31.3
A-3010	53.8	16.6	65.2	96.4	0.2	3.1
A-3001	113.6	39.5	43.8	70.1	11.9	4.0

^a Average conversion and selectivity between 1 and 5 h, catalyst weight 0.150 g, feed rate 1.8 cm³ h⁻¹, carrier gas flow rate 30 cm³ min⁻¹ at 240 °C.

^b Specific surface area cited from Ref. [14].

^c Cu surface area cited from Ref. [14].

Table 2.2 Effect of additive to A-3001 sample on physical and catalytic property in the dehydrogenative cyclization of 1,4-BDO ^a

Catalyst	S _{ABET} ^b / m ² g ⁻¹	S _{Cu} ^c / m ² g ⁻¹	Conv. / %	Selectivity/ mol %		
				GBL	THF	2HTHF
A-6002 ^d	113.6	39.5	43.8	70.1	11.9	4.0
A-6202	101.0	52.7	71.0	96.1	< 0.1	3.3
A-6022	134.4	36.0	62.0	95.1	0.4	3.7
A-6220	51.8	20.7	50.6	86.7	0	10.1
A-6222	120.1	39.7	67.4	92.6	0.1	3.6
A-6122	131.2	40.3	84.0	97.7	0.2	1.6

^a Average conversion and selectivity between 1 and 5 h, catalyst weight 0.150 g, feed rate 1.8 cm³ h⁻¹, carrier gas flow rate 30 cm³ min⁻¹ at 240 °C.

^b Specific surface area cited from Ref. [14].

^c Cu surface area cited from Ref. [14].

^d Equals A-3001.

Table 2.3 Physical property and catalytic activity of A-x122 (x=0–95) sample in the dehydrogenative cyclization of 1,4-BDO^a

<i>x</i>	SA _{BET} ^b / m ² g ⁻¹	SA _{Cu} ^c / m ² g ⁻¹	Conv. / %	Selectivity/ mol %		
				GBL	THF	2HTHF
0	183.3	-	43.5	0.6	95.0	0.3
1	161.3	36.3	57.7	75.2	1.3	4.0
3	144.7	35.5	67.5	95.9	0.1	2.3
6	131.2	40.3	84.0	97.7	0.2	1.6
12	99.7	38.7	84.1	94.9	0.1	1.5
18	83.2	45.1	74.9	96.1	< 0.1	2.1
95	37.3	31.6	56.1	93.2	0.2	3.9

^a Average conversion and selectivity between 1 and 5 h, reaction temperature 240 °C, catalyst weight 0.150 g, feed rate 1.8 cm³ h⁻¹, carrier gas flow rate 30 cm³ min⁻¹.

^b Specific surface area cited from Ref. [14].

^c Cu surface area cited from Ref. [14].

Table 2.4 Dehydrogenation of 2HTHF ^a

Catalyst	Conversion / %	Selectivity / mol%	
		GBL	1,4-BDO
A-0122	25.6	18.2	12.0
A-3000	12.1	35.7	1.8
A-3100	12.1	27.5	7.0
A-3010	76.9	80.3	13.9
A-3001 (=A-6002)	79.6	84.8	6.0
A-3111 (=A-6222)	88.4	66.7	3.9

^a Each data were obtained by the reaction results of initial 1 h, reaction temperature 240 °C, catalyst weight 0.150 g, feed rate 1.8 cm³ h⁻¹, carrier gas flow rate 30 cm³ min⁻¹.

Table 2.5 Transformation of SDA^a

Catalyst	Carrier gas	Conversion / %	Selectivity/ mol %		
			GBL	2HTHF	1,4-BDO
A-0122	He	14.4	69.2	30.8	0
A-0122	H ₂	14.9	77.8	21.4	0.8
A-3010	He	2.7	93.8	0	6.2
A-3010	H ₂	89.9	95.6	4.0	0.4
A-3111	He	0.5	100	0	0
A-3111	H ₂	88.4	92.0	5.6	2.4

^a Each data were obtained by the reaction results of initial 1 h, reaction temperature 240 °C, catalyst weight 0.150 g, carrier gas flow rate 30 cm³ min⁻¹. SDA solution of 21.0 wt % was fed at 1.8 cm³ h⁻¹.

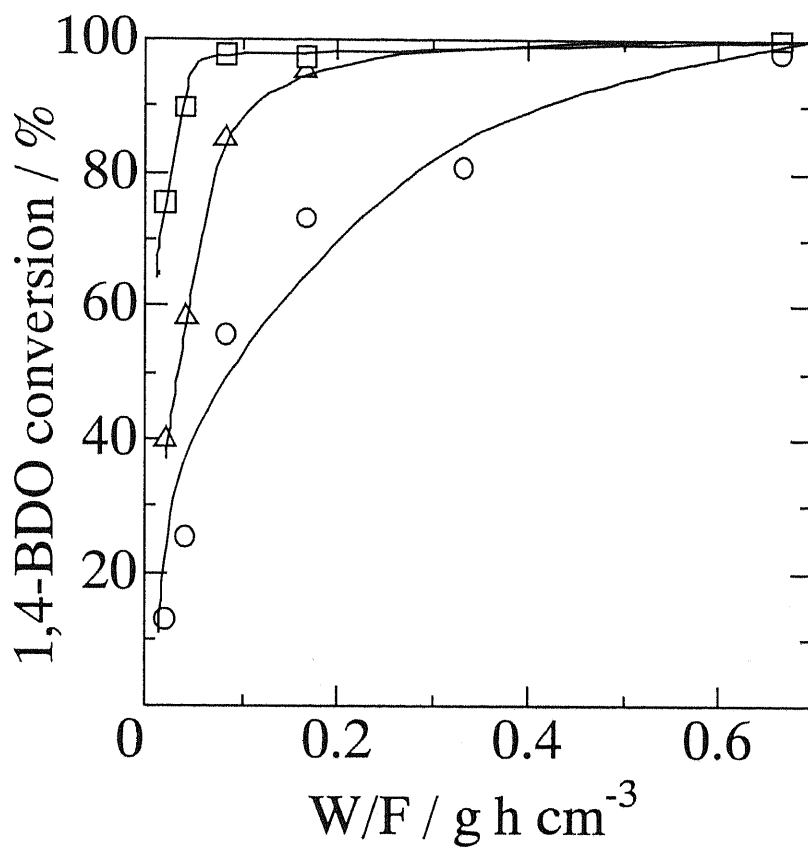


Fig. 2.1 Relation between the conversion of BDO and W/F at (○) 200 °C, (△) 240 °C and (□) 300 °C over A-6122 sample.

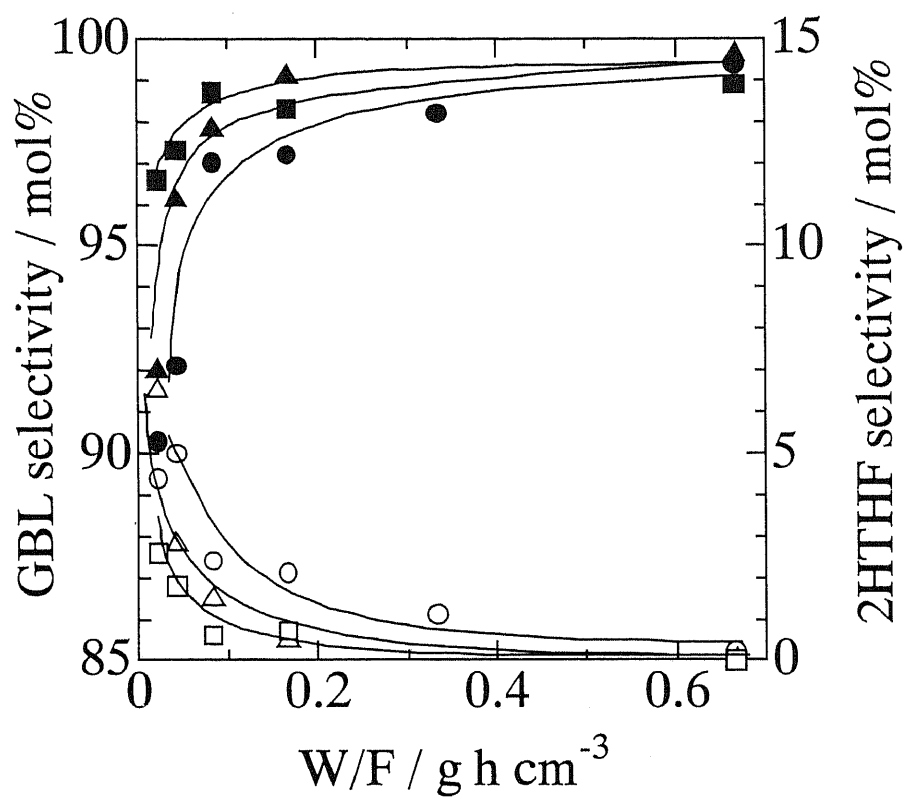


Fig. 2.2 Relation between the selectivity to GBL (closed symbol), 2HTHF (open symbol) and W/F at (circle) 200 °C, (triangle) 240 °C, (square) 300 °C over A-6122 sample.

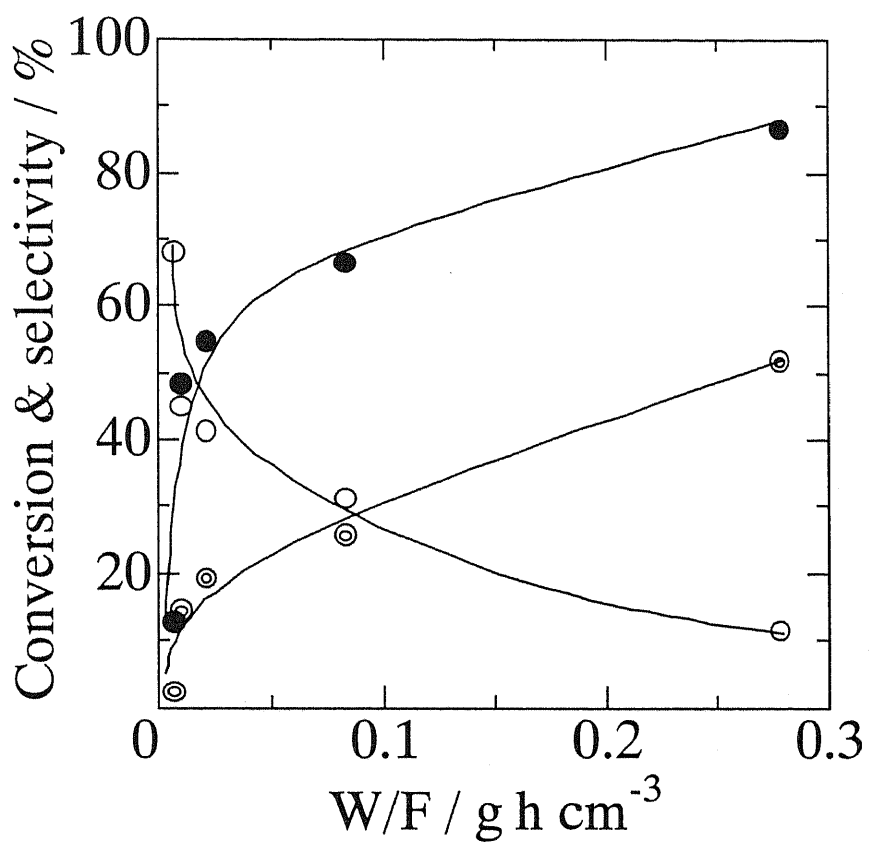


Fig. 2.3 Relation between the conversion of BDO (⊙), the selectivity to GBL (●) and 2HTHF (○), and W/F over A-3100 sample at 240 °C.

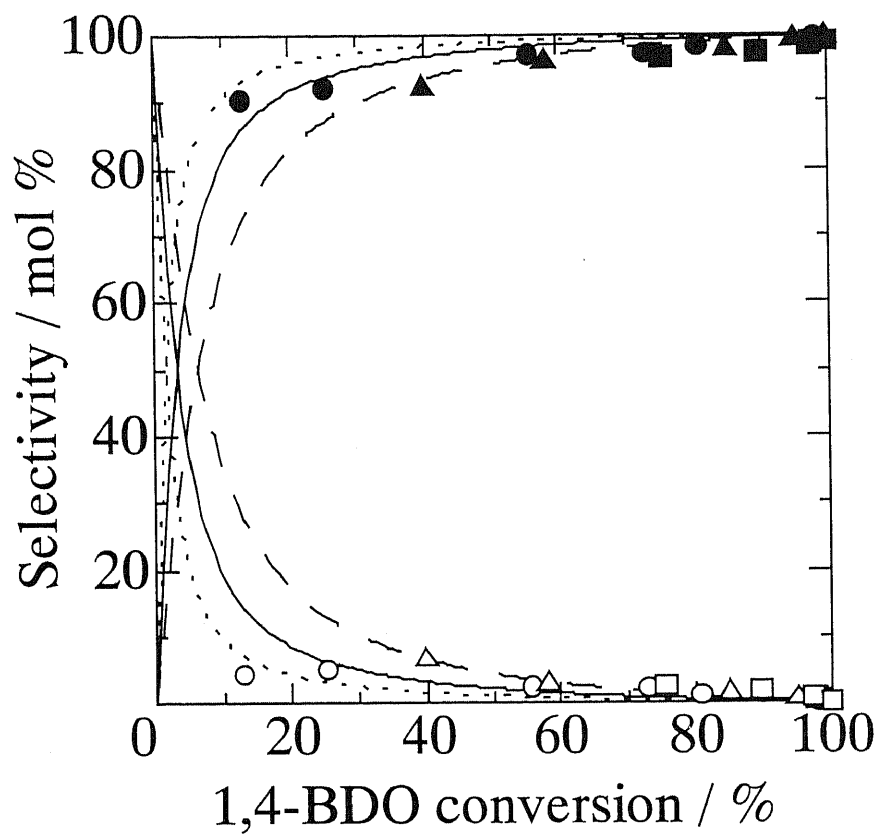


Fig. 2.4 The theoretical selectivity-conversion curves simulated at several k_2/k_1 over A-6122 sample; broken line: $k_2/k_1=24$, solid line: $k_2/k_1=48$, dotted line: $k_2/k_1=96$. Symbols are the same as those in Fig. 2.2.

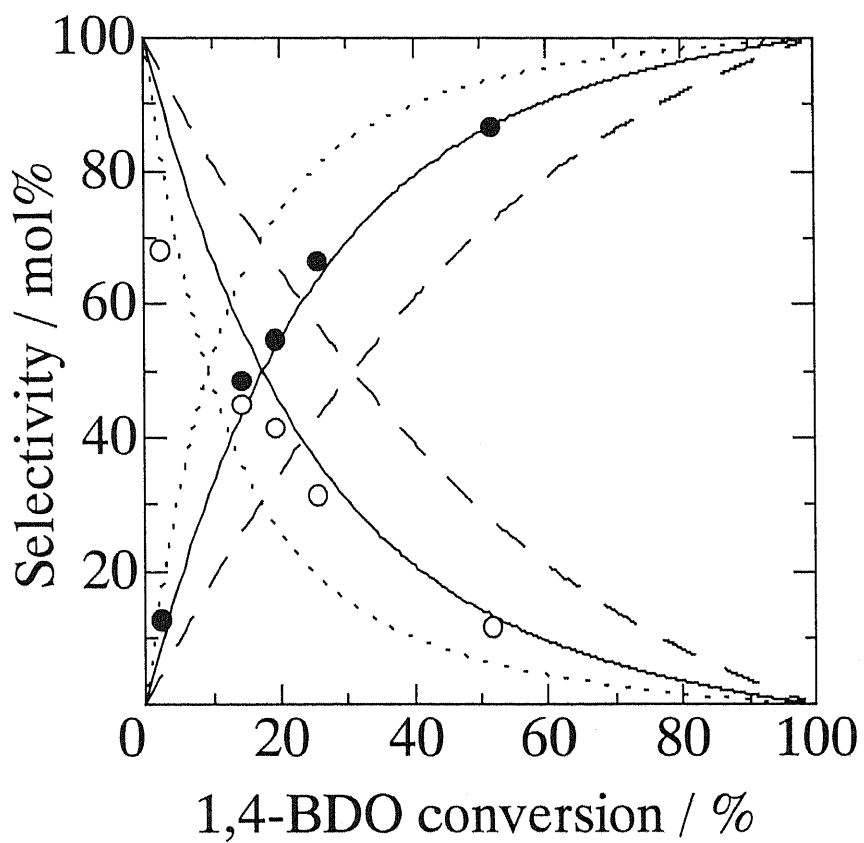


Fig. 2.5 The theoretical selectivity-conversion curves simulated at several k_2/k_1 over A-3100 sample; broken line: $k_2/k_1=4$, solid line: $k_2/k_1=8$, dotted line: $k_2/k_1=16$. Symbols are the same as those in Fig. 2.3.

Chapter 3

Synthesis of 3-buten-2-one from 4-hydroxy-2-butanone over anatase-TiO₂ catalyst

3.1 Introduction

3-Buten-2-one (MVK) is known as an intermediate of steroids, terpenoids, medical drugs, and pesticides. Several reports for the production of MVK have been recently focused on the condensation of propanone with methanol. Catalysts such as Fe-Cu complex [1], SnO₂ doped with rare earth metal [2], and phosphorous-metal mixed oxides [3] are employed in the reaction. Methane is also used as the condensation reagent instead of methanol over MgO catalyst [4]. On the other hand, the dehydration of 4-hydroxy-2-butanone (HB) to MVK in di-*n*-butyl phthalate including small amount of iodine and hydroquinone had been reported [5]. At this point, MVK is manufactured by dehydration of HB catalyzed by soluble acid in a liquid phase. HB can be produced by coupling of propanone and formaldehyde in basic media [6,7]. As mentioned in Section 1.3, the production of HB via the dehydrogenation of 1,3-butanediol (1,3-BDO) is potential process, whereas HB is not selectively obtained over Cu-based catalysts. This will be the target reaction for the utilization of 1,3-BDO.

The dehydration with liquid acid catalysts such as sulfuric acid, phosphoric acid, and so on, are used in many chemical processes, while heterogeneous catalyst has some advantages: It facilitates the separation of products from catalyst and there is no need to neutralize the homogeneous catalyst in order to extract the products. However, no effective heterogeneous catalyst has been proposed in the dehydration of HB into MVK.

Therefore, in this chapter, the dehydration of HB to MVK is investigated over several metal oxides, and it is found that anatase-TiO₂ has excellent activity for the reaction. In this paper, the effect of temperature on the reaction over anatase-TiO₂ and comparison of TiO₂ catalyst with other solid catalysts are examined.

3.2 Experimental.

3.2.1. Catalyst samples

All the samples, except for two TiO₂, were commercially available. TiO₂ samples were supplied by Catalysis Society of Japan as the Japan Reference Catalysts. The specific surface area of samples was calculated from the adsorption isotherm of N₂ at -196 °C with BET method. The temperature-programmed desorption of adsorbed ammonia (NH₃-TPD) was also carried out to measure acidity of the catalysts. A sample (10 mg) was preheated at 500 °C for 1 h under reduced pressure. NH₃ was adsorbed at 100 °C for 10 min and evacuated for 1h. After no NH₃ had been observed in N₂ flow, the sample was heated from 100 to 800 °C at heating rate of 10 °C min⁻¹ under N₂ flow of 99 mmol min⁻¹. The detailed TPD procedure was described elsewhere [8]. The origin of samples, their specific surface area and the total amount of acid are listed in Table 3.1.

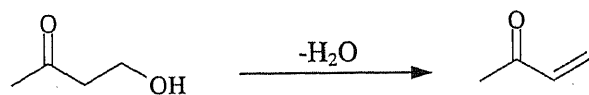
3.2.2. Catalytic reaction

The reaction was carried out in a conventional down-flow tubular-reactor at ambient pressure. A catalyst was charged in the reactor, and catalyst bed was heated at a prescribed temperature in He carrier gas of 30 cm³ min⁻¹ (STP). After the catalyst bed had been heated for 60 min, liquid HB was fed into the reactor at feed rate of 1.7

$\text{cm}^3 \text{h}^{-1}$. The effluent collected periodically at 0 °C every hour was analyzed with FID-GC (GC-8A, Shimadzu, Japan) with 30-m capillary column (TC-WAX). Gaseous products were analyzed with on-line TCD-GC (GC-8A) with 2-m packed column (Porapak Q).

3.3 Results and discussion

Fig. 3.1 exhibits the changes in HB conversion with time on stream at different temperatures over anatase-TiO₂. MVK is efficiently produced over anatase-TiO₂ at <200 °C, as shown in Scheme 3.1. Deactivation was confirmed at temperatures higher than 160 °C, and it was found that the deactivated catalysts changed their color from white to black. To confirm the cause of the deactivation, the deactivated sample was oxidized. Oxidation was performed as following procedure; the dehydration of HB was carried out over anatase-TiO₂ at 350 °C for 300 min, and then the catalyst was heated in the air at 500 °C for 60 min, and cooled to 350 °C. After the oxidation treatment, the catalyst recovered the initial activity (data not shown). This result suggests that the cause of deactivation is deposition of carbon species onto the catalyst surface. In general, olefins are the precursor of the carbon species, and they are formed over acid sites [9]. In this study, MVK is the precursor of carbon species. The initial step of the deactivation was adsorption of MVK on the acid sites and the adsorbed MVK was sequentially polymerized. The rate of polymerization increases with increasing the reaction temperature, whereas the desorption rate of MVK also increases. The polymerization rate probably exceeds the desorption rate of MVK above 160 °C.



Scheme 3.1 Dehydration of 4-hydroxy-2-butanone into 3-buten-2-one

Fig. 3.2 depicts temperature dependence of average catalytic activity of anatase-TiO₂ in the initial reaction for 300 min. The highest HB conversion and MVK selectivity were attained at 160 °C. The HB conversion decreased with increasing the reaction temperature from 160 to 240 °C, while it increased above 300 °C. Although the selectivity to propanone kept in low level at <240 °C, it increased above 240 °C. In order to elucidate the origin of propanone, blank tests were carried out without using catalyst at several temperatures. Propanone was formed at 240 °C in the non-catalytic reaction of HB (figure not shown). The formation of propanone would be attributed to the thermal decomposition of HB, which is the ketol of propanone and formaldehyde. The catalytic dehydration of HB to MVK and the thermal decomposition of HB to propanone were competitive, and the rate of the latter would increase with increasing the reaction temperature above 240 °C. Therefore, the HB conversion was recovered above 300 °C (Fig. 3.2).

Finally, I examined the catalytic activity for the HB dehydration over several oxide samples at 160 °C (Fig. 3.3). Although the metal oxides such as rutile-TiO₂, Al₂O₃, CeO₂ and SiO₂-Al₂O₃ showed relatively high initial activity, they were rapidly deactivated. The SiO₂-Al₂O₃ showed the largest deactivation. The other samples, rutile-TiO₂, Al₂O₃, and CeO₂ exhibited moderate deactivation. They showed deactivation even at 120 °C, while the selectivity to MVK is high in all the samples (Table 3.1). Propanone is the major by-product with 1-2 mol% selectivity. Dehydration of alcohols is readily catalyzed by acids [10]. However, the deactivation

is probably caused by the strong interaction of MVK with acid sites to form carbon species on the catalyst surface, as discussed above.

Fig. 3.4 shows TPD profiles of NH_3 adsorbed on the samples. The total amounts of acid sites are listed in Table 3.1. It is obvious that $\text{SiO}_2\text{-Al}_2\text{O}_3$ is the strongest acid catalyst in this study, and that Al_2O_3 has the second highest acidity on its surface. It can be confirmed that anatase- TiO_2 has only weak acid sites because the TPD peak is located at 125 °C. It should be noted that the acidity of rutile- TiO_2 is higher than that of anatase- TiO_2 . TPD profile of CeO_2 is similar to that of anatase- TiO_2 , and SiO_2 has no NH_3 adsorbed on its surface at 100 °C.

The NH_3 -TPD results support the speculation about the deactivation of the catalysts, except for CeO_2 : the samples with strong acid such as $\text{SiO}_2\text{-Al}_2\text{O}_3$, Al_2O_3 and rutile- TiO_2 were deactivated, and the degree of the deactivation follows the acid strength of the samples. $\text{SiO}_2\text{-Al}_2\text{O}_3$ with the strongest acidity exhibited the steepest deactivation behavior among the samples. Al_2O_3 showed more rapid degradation in catalysis than rutile- TiO_2 , which is attributed to the higher acidity on Al_2O_3 surface. In spite of the similar acidity, deactivation behavior is different between anatase- TiO_2 and CeO_2 . The cause of the difference cannot be explained in the TPD study. Redox nature of CeO_2 would be correlated with the deactivation. The activation of alcohols over CeO_2 for the dehydration of 1,3-BDO to 3-buten-2-ol and *trans*-2-buten-1-ol [11] and the dehydration of 1,4-BDO to 3-buten-1-ol [12] have been reported, and It has been concluded that the redox property of CeO_2 plays a crucial role in the catalytic dehydration of diols.

No acid sites are observed on SiO_2 surface in the NH_3 -TPD analysis. However, even SiO_2 with the weakest acidity as well as anatase- TiO_2 shows stable conversion. It

is surprising that the dehydration of HB to MVK, which is probably stabilized by the conjugated double bond, proceeds over the less acidic SiO₂ at 160 °C. Namely, the dehydration of HB requires weak acid sites, and strong ones induce unfavorable deactivation because of strong interaction between MVK and the acid sites.

3.4 Conclusion

4-Hydroxy-2-butanone was converted to 3-buten-2-one with 98.8 mol% selectivity over anatase-TiO₂ catalyst, and no deactivation was observed at 160 °C. Propanone was produced as a by-product in the thermal decomposition of 4-hydroxy-2-butanone above 240 °C. Acidic catalysts such as Al₂O₃ and SiO₂-Al₂O₃ were deactivated because the strong acid sites interacted with 3-buten-2-one to form carbonaceous species. Weak acid sites of anatase-TiO₂ and SiO₂ are sufficient for the dehydration of 4-hydroxy-2-butanone to 3-buten-2-one.

References in Chapter 3

- [1] M. Sato, S. Akabori, M. Katada, I. Motoyama, H. Sano, *Chem. Lett.* (1987) 1847-1850.
- [2] N. L. V. Carreno, H. V. Fajardo, A. P. Maciel, A. Valentini, F. M. Pontes, L. F. D. Probst, E. R. Leite, E. Longo, *J. Mol. Catal. A* **207** (2004) 91-96.
- [3] *Japan Kokai Tokkyo Koho*. JP05-009146.
- [4] E. Ruckenstein, B. M. Reddy, *Appl. Catal. A* **121** (1995) 159-167.
- [5] N. A. Milas, E. Sakal, J. T. Plati, J. T. Rivers, J. K. Gladding, F. X. Grossi, Z. Weiss, M. A. Campbell, H. F. Wright, *J. Am. Chem. Soc.* **70** (1948) 1597-1607.
- [6] J. T. Hays, G. F. Hager, H. M. Engelmann, H. M. Spurlin, *J. Am. Chem. Soc.* **73**

(1951) 5369-5373.

[7] *Japan Kokai Tokkyo Koho JP S52-128311.*

[8] S. Sato, K. Takematsu, T. Sodesawa, F. Nozaki, *Bull. Chem. Soc. Jpn.* **65** (1992) 1486-1490.

[9] C. H. Bartholomew, *Appl. Catal. A* **212** (2001) 17-60.

[10] J. McMurry, *Fundamentals of Organic Chemistry, third ed*, Brooks/ Cole, California, 1994.

[11] S. Sato, R. Takahashi, T. Sodesawa, N. Honda, H. Shimizu, *Catal. Commun.* **4** (2003) 77-81.

[12] S. Sato, R. Takahashi, T. Sodesawa, N. Yamamoto, *Catal. Commun.* **5** (2004) 397-400.

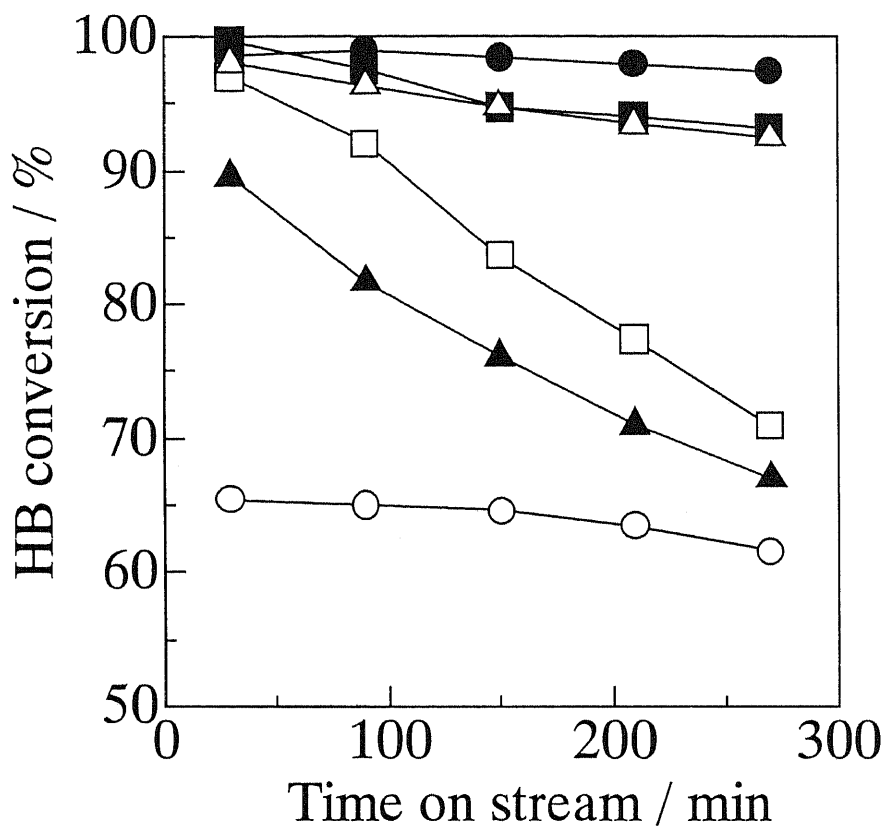


Fig. 3.1 Changes in HB conversion with time on stream over anatase-TiO₂. The reaction was carried out at (○) 120 °C, (●) 160 °C, (△) 200 °C, (▲) 240 °C, (□) 300 °C, (■) 350 °C. Catalyst weight, 0.050 g; HB feed rate, 1.7 cm³ h⁻¹; He flow rate, 30 cm³ min⁻¹.

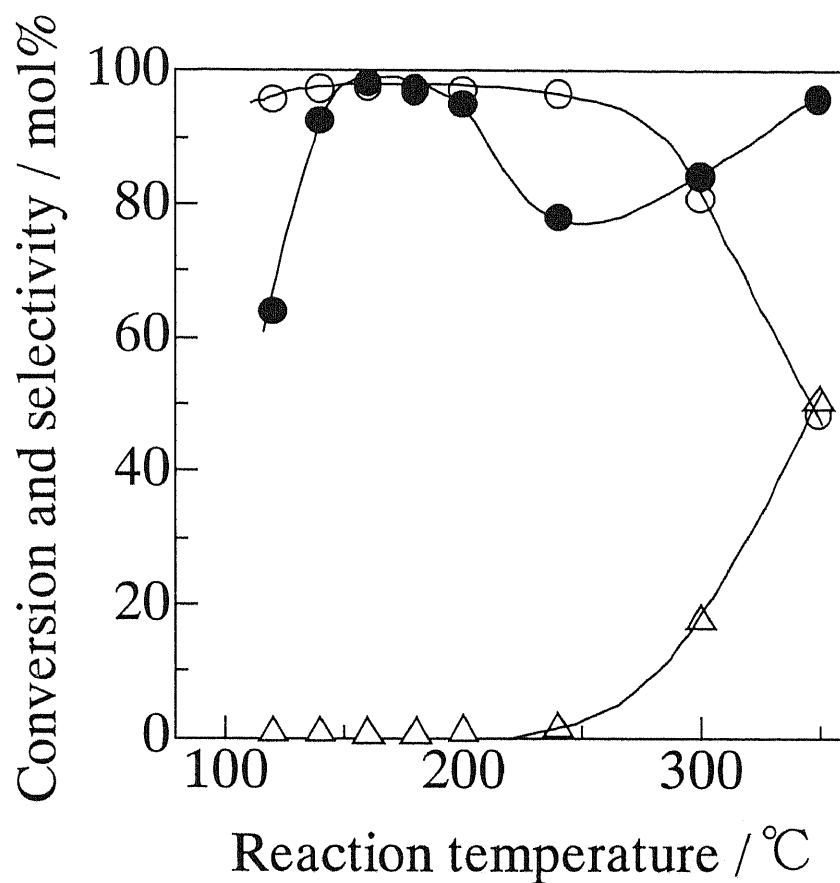


Fig. 3.2 Changes in average HB conversion and selectivities to MVK and propanone at 120-350 °C over anatase-TiO₂. (●) HB conversion, (○) MVK selectivity, (△) propanone selectivity. The reaction conditions are the same as those in Fig. 1.

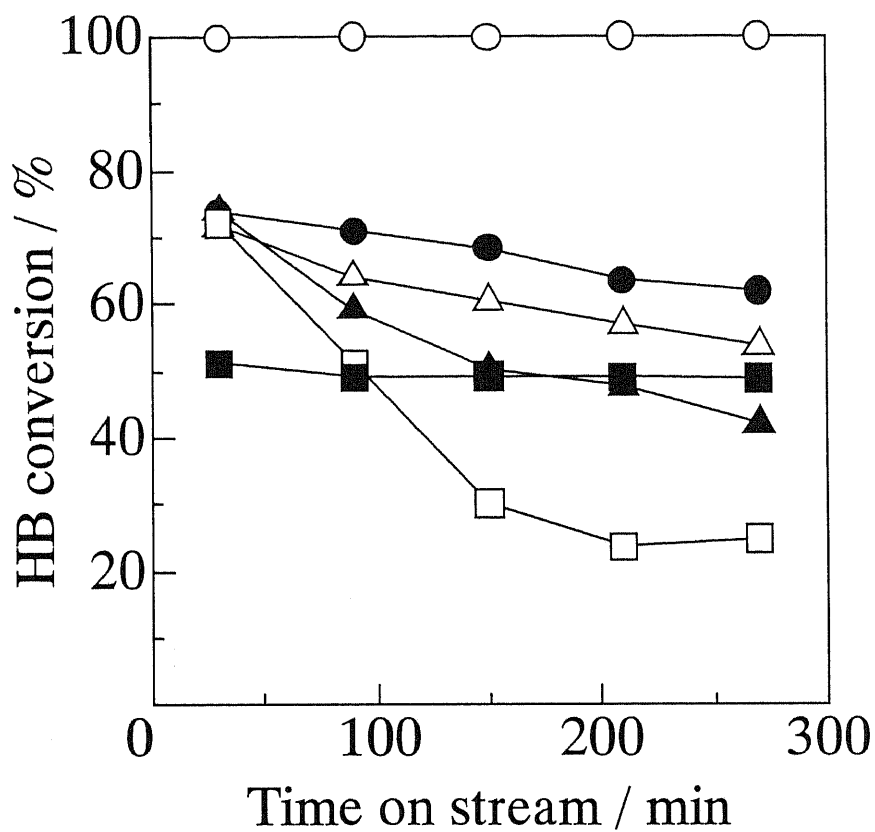


Fig. 3.3 Changes in HB conversion with time on stream over various catalysts at 160 °C. (○) anatase-TiO₂, (●) rutile-TiO₂, (△) Al₂O₃, (▲) CeO₂, (□) SiO₂-Al₂O₃ and (■) SiO₂. Catalyst weight, 0.150 g.

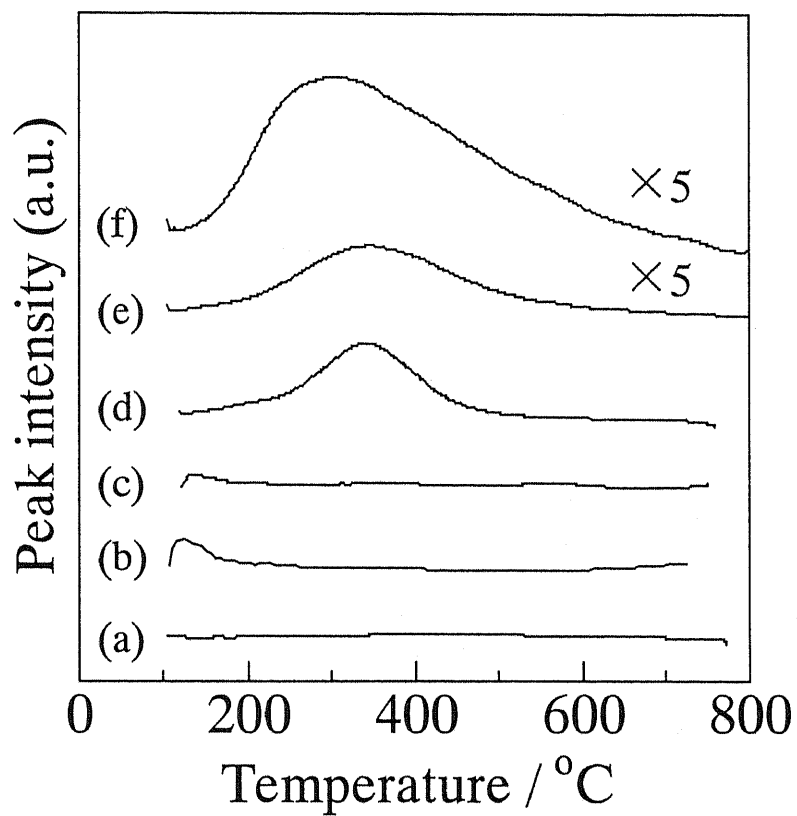


Fig. 3.4 TPD profiles of NH_3 adsorbed on several samples. (a) SiO_2 , (b) CeO_2 , (c) anatase- TiO_2 , (d) rutile- TiO_2 , (e) Al_2O_3 , and (f) SiO_2 - Al_2O_3 .

Table 3.1 The catalysts used for the reaction.

Catalyst	Origin	SA _{BET} / m ² g ⁻¹	Selectivity ^a / mol%	Acidity ^b / μmol g ⁻¹
anatase-TiO ₂	TIO-4 (Japan Reference Catalyst)	55	98.8	4.5
rutile-TiO ₂	TIO-3 (Japan Reference Catalyst)	40	97.1	30.8
Al ₂ O ₃	DC-2282 (Dia Catalyst)	200	96.1	166
CeO ₂	(Wako Pure Chemical Industry)	20	97.9	4.7
SiO ₂ - Al ₂ O ₃	N631-L (Nikki Chemical)	420	96.8	440
SiO ₂	Q-10 (Fuji Silysia Chemical)	295	97.4	2.4

^a Selectivity to MVK in the reaction of HB at 160 °C shown in Fig. 3.3.

^b Total acidity measured by NH₃-TPD (Fig. 3.4).

Chapter 4

Catalytic Reaction of 1,3-butanediol over solid acids

4.1 Introduction

Unsaturated alcohols are important compound in industrial chemistry because they can be used as raw material and intermediates of pesticides, medicines and so on. Selective hydrogenation of unsaturated carbonyl compounds to unsaturated alcohols has been extensively investigated: in the homogeneous system, the stoichiometric reagent, NaBH_4 /lanthanoide chloride [1] and Ru-complex system [2,3] are reported to show effective ability for this reaction. In the heterogeneous system, Cr-modified Raney-Ni [4], Sn-Pt/Nylon [5] and M/zeolite (M=Ru, Pt, Rh) catalysts [6] show good catalytic performance for the selective hydrogenation of unsaturated ketones into unsaturated alcohols. Recently, novel catalyst system such as Meerwein-Ponndorf-Verley reduction over $\text{Zr}(\text{O}-n\text{-Pr})$ on mesoporous molecular sieve [7], and supported-Au catalyst [8,9] are presented.

It has been found that CeO_2 has catalytic activity for the selective dehydration of 1,3-diols [10,11] and 1,4-BDO [12] to unsaturated alcohols. For example, 1,3-BDO is dehydrated into 3-buten-2-ol and *trans*-2-buten-1-ol at 325 °C with selectivity of 56.9 mol% and 35.5 mol%, respectively [11], while 1,4-BDO requires the reaction temperature above 375 °C to be activated, and the selectivity to 3-buten-1-ol is 68.1 mol% [12]. The mechanism of the dehydration of 1,3-BDO over CeO_2 (111) surface was investigated, and it was concluded that the oxygen-defect site of CeO_2 (111) surface probably the active site for the dehydration of 1,3-BDO to unsaturated alcohols [13].

It is well known that acid and base catalyze alcohols to dehydrate into olefins [14]. However, the reaction of diols over acid-base catalysts has not been deeply

investigated. Therefore, in this study, the promising acid catalysts for the dehydration of 1,3-BDO into unsaturated alcohol are investigated. The effect of acid and base properties of the catalysts on the catalytic activity and selectivity to products are discussed.

4.2 Experimental

I used four metal oxides such as SiO₂-Al₂O₃, Al₂O₃, ZrO₂ and rutile-TiO₂. SiO₂-Al₂O₃ (N631-L), Al₂O₃ (DC2282) and ZrO₂ (RSC-100) were supplied from Nikki Chemical, Dia Catalyst and Daiichi Kigenso Kagaku Kogyo Co., Ltd., respectively. TiO₂ was supplied by Catalysis Society of Japan, Japan Reference Catalyst TIO-3. The specific surface area of SiO₂-Al₂O₃, Al₂O₃, TiO₂ and ZrO₂ were 420, 200, 40 and 100 m² g⁻¹, respectively, which were estimated by BET method using N₂ isotherm at -196 °C.

Temperature-Programmed Desorptions (TPD) of NH₃ and CO₂ was carried out to evaluate the acid and base properties, respectively. The numbers of acid and base sites were estimated from the neutralization-titration curves of H₂SO₄ and NaOH solution, respectively. The procedure of TPD was detailed in elsewhere [15].

The catalytic reactions of alcohols were carried out in a conventional fixed-bed down-flow reactor. 1,3-Butanediol, 1-butanol and 2-butanol were purchased from Waco Pure Chemical Ind. Ltd., Japan, and unsaturated alcohols such as 3-buten-1-ol, 3-buten-2-ol and 2-buten-1-ol were purchased from Tokyo Kasei Kogyo Co., Ltd., Japan. All the reagents were used without further purification. The catalyst bed was heated in an N₂ flow at a rate of 30 cm³ min⁻¹ at the desired reaction temperature of 200–375 °C and kept for 1 h as the pretreatment. The reaction was carried out in the N₂ flow at a rate of 30 cm³ min⁻¹. Then, a reactant was fed into the reactor at a liquid

flow rate of $1.7 \text{ cm}^3 \text{ h}^{-1}$. A liquid effluent was collected with ice trap and analyzed periodically every 1 h by FID-GC (Shimadzu GC-8A equipped with 30 m length of TC-WAX column) and gaseous products were analyzed by on-line TCD-GC (Shimadzu GC-8A equipped with 6 m length of VZ-7). The products were identified with GC-MS (Shimadzu GCMS-QP5050A).

Selectivity to product, S , was calculated with following equation:

$$S = \frac{(\text{amount of product}) \times (\text{the number of carbon atoms in the product})}{(\text{total amount of products})}$$

4.3 Results

Fig. 4.1 shows NH_3 - and CO_2 -TPD profiles of the catalysts, and Table 4.1 lists the physical properties of them. The desorption of NH_3 was observed over all the catalysts. $\text{SiO}_2\text{-Al}_2\text{O}_3$ showed the largest and asymmetric desorption peak of NH_3 . This asymmetry implies that $\text{SiO}_2\text{-Al}_2\text{O}_3$ has acid sites with different strength. I deconvoluted the desorption peak into two peaks with Gaussian fitting, as shown in Fig. 4.1A. The peaks centered at 279 and 414 °C, respectively. Al_2O_3 and TiO_2 had symmetric desorption peak of NH_3 centered at 345 and 342 °C, respectively, while the amount of acid sites of Al_2O_3 is ca. five times larger than that of TiO_2 . ZrO_2 showed the weakest and broad desorption peak centered at 214 °C. This suggests that ZrO_2 has the weakest acid sites and its amount is the smallest. In the CO_2 -TPD, I could not confirm the desorption of CO_2 from $\text{SiO}_2\text{-Al}_2\text{O}_3$ and TiO_2 , whereas Al_2O_3 and ZrO_2 have a small desorption peak centered around 110 °C. These results indicate that $\text{SiO}_2\text{-Al}_2\text{O}_3$ and TiO_2 have no base sites on their surface, and Al_2O_3 and ZrO_2 have weak base sites together with acid ones. Hence, it was summarized that the sequences of

acid and base property of the catalysts as $\text{SiO}_2\text{-Al}_2\text{O}_3 > \text{Al}_2\text{O}_3 > \text{TiO}_2, > \text{ZrO}_2$, and $\text{Al}_2\text{O}_3 > \text{ZrO}_2 \gg \text{SiO}_2\text{-Al}_2\text{O}_3, \text{TiO}_2$, respectively.

Fig. 4.2 shows the activities of the catalysts at different reaction temperatures. Conversion of 1,3-butanediol monotonously increased with increasing the reaction temperature over all the catalysts. $\text{SiO}_2\text{-Al}_2\text{O}_3$ catalyzed the dehydration of 1,3-butanediol at the lowest reaction temperature among the catalysts. Al_2O_3 , TiO_2 and ZrO_2 required the temperature around 250, 350 and 350 °C to activate 1,3-butanediol, respectively. Table 4.2 summarizes the product distribution in the reaction results of 1,3-butanediol over the catalysts. 3-Buten-1-ol was the major product over $\text{SiO}_2\text{-Al}_2\text{O}_3$, TiO_2 and ZrO_2 at any temperatures. Formaldehyde and 4-methyl-1,3-dioxane, however, were mainly obtained over Al_2O_3 . With increasing the reaction temperature, the selectivity to 1,3-butadiene, the consecutive dehydration product from unsaturated alcohols, increased while that to unsaturated ethers, the bimolecular dehydration products from unsaturated alcohols, decreased over $\text{SiO}_2\text{-Al}_2\text{O}_3$. TiO_2 and ZrO_2 exhibited similar conversion level of 1,3-butanediol at the same reaction temperature. The compounds such as 3-buten-2-one, 2-butenal, 1-butanol and 2-butanol were produced via dehydrogenation and/or hydrogenation and were obtained with relatively large selectivities over TiO_2 and ZrO_2 . Over ZrO_2 , 3-buten-2-ol was preferably produced compared to the other catalysts, where 3-buten-2-one and butanone were major by-products.

I tested the dehydration of 1-butanol and 2-butanol in order to confirm the difference of reactivity of OH groups of the butanol. Tables 4.3 and 4.4 summarize the reaction results of 1- and 2-butanols over $\text{SiO}_2\text{-Al}_2\text{O}_3$, TiO_2 and ZrO_2 , respectively. In the reaction of 1-butanol, $\text{SiO}_2\text{-Al}_2\text{O}_3$ exhibited the highest activity even though the reaction temperature over $\text{SiO}_2\text{-Al}_2\text{O}_3$ was lower than that over TiO_2 and ZrO_2 by 125

°C. TiO₂ showed moderate activity and ZrO₂ hardly activated 1-butanol at 350 °C. 2-Butenes were mainly produced over SiO₂-Al₂O₃, while 1-butene was predominantly obtained over TiO₂ and ZrO₂. I note that butyl butyrate was produced over ZrO₂ with the selectivity of 22.2 mol%. In the reaction of 2-butanol, the catalytic activity showed similar tendency as the case of 1-butanol, i.e. SiO₂-Al₂O₃ > TiO₂ > ZrO₂. *Cis*-2-butene was mainly produced over SiO₂-Al₂O₃ and TiO₂, whereas 1-butene was obtained with the largest selectivity over ZrO₂. The reactivity of 2-butanol was much higher than 1-butanol over the catalysts.

I also examined the reactivity of unsaturated alcohols over SiO₂-Al₂O₃ and TiO₂. The results over SiO₂-Al₂O₃ and TiO₂ are listed in Tables 4.5 and 4.6, respectively. Over SiO₂-Al₂O₃, 2-buten-1-ol and 3-buten-2-ol were predominantly dehydrated into 1,3-butadiene at the same conversion level. On the contrary, 3-buten-1-ol was subject to decomposition to produce propene and formaldehyde with the highest selectivity and the dehydration into 1,3-butadiene did not effectively proceed. Furthermore, the reactivity of 3-buten-1-ol was lower than those of 2-buten-1-ol and 3-buten-2-ol. The reactivity of unsaturated alcohols over TiO₂ was summarized as the following sequence: 3-buten-2-ol > 2-buten-1-ol > 3-buten-1-ol. The consecutive dehydration into 1,3-butadiene proceeded for all the unsaturated alcohols, while the several side reactions were also promoted over TiO₂. Consequently, the product distribution was very complex.

4.4 Discussion

4.4.1 *Effects of acid and base properties of catalysts on catalytic performance*

In this study, four catalysts with different acid and base properties were

employed to investigate the effects of these properties on catalytic performance.

$\text{SiO}_2\text{-Al}_2\text{O}_3$ showed the highest activity because it catalyzed the dehydration of 1,3-butanediol at the lowest temperature among the catalysts I tested. Then, the sequence of the catalytic activity can be summarized as follows; $\text{SiO}_2\text{-Al}_2\text{O}_3 > \text{Al}_2\text{O}_3 \gg \text{TiO}_2 \approx \text{ZrO}_2$ (Fig. 4.2). It shows good coincidence with the acidity of catalysts: the most acidic catalyst, $\text{SiO}_2\text{-Al}_2\text{O}_3$, exhibited the highest activity for the reaction of 1,3-butanediol. These results imply that the dehydration of 1,3-butanediol is catalyzed at acid sites of the catalysts.

Furthermore, the reaction of 1- and 2-butanols was carried out over $\text{SiO}_2\text{-Al}_2\text{O}_3$, TiO_2 and ZrO_2 to discuss the reaction mechanism of 1,3-butanediol dehydration (Tables 4.3 and 4.4). It should be noted that 2-butanol is more reactive than 1-butanol. This result suggests that reaction should proceed via carbocation as the intermediate: secondary carbocation, which is produced from the elimination of OH group from 2-butanol, is more stable than primary one which is derived from 1-butanol. The product distribution from butanols over acidic $\text{SiO}_2\text{-Al}_2\text{O}_3$ and TiO_2 also supports the acid-catalyzed mechanism. Zaitsev products are mainly obtained with acid-catalyzed mechanism [14], and 2-butenes, Zaitsev product, were mainly produced from 2-butanol. 1-Butene is, however, selectively produced from 2-butanol over ZrO_2 . It is well known that ZrO_2 gives Hoffman products from secondary alcohols [16,17]. I would like to mention that butyl butyrate was produced with a moderate selectivity from 1-butanol over ZrO_2 . It is possible to consider that the reaction from 1-butanol to butyl butyrate proceeds via Tishchenko reaction of n-butylaldehyde [18] or hemiacetal formation [19-21].

4.4.2 Different product-distribution among the catalysts

The dehydration of 1,3-diols over CeO_2 catalyst has been already reported [10,11,13], and it is concluded that the reaction is promoted by radical mechanism [11,13]. Hence, 1,3-butanediol would be activated with different mechanism between acid catalysts and CeO_2 . Actually, the distribution of the dehydrated products of 1,3-butanediol was different each other. 3-Buten-2-ol and *trans*-2-buten-1-ol were selectively produced over CeO_2 , while 3-buten-1-ol was preferably obtained over acid $\text{SiO}_2\text{-Al}_2\text{O}_3$, which was the strong acid catalyst with no base sites on its surface, as shown in Fig. 4.1. Generally, alcohols are dehydrated to give Zaitsev products over acid catalysts as mentioned above [14]. Thus, 2-buten-1-ol should be produced as the main dehydrated products over acid catalysts. I elucidated the reactivity of unsaturated alcohols in the consecutive reaction (Tables 4.5 and 4.6). 1,3-Butadiene was produced over $\text{SiO}_2\text{-Al}_2\text{O}_3$. The selectivity to 1,3-butadiene increased while those to unsaturated alcohols decreased with increasing the conversion of 1,3-butanediol (Table 4.2). 1,3-Butadiene could be produced from unsaturated alcohols over $\text{SiO}_2\text{-Al}_2\text{O}_3$, while 3-buten-1-ol was less reactive than 2-buten-1-ol and 3-buten-2-ol, and remained in the reaction mixture (Table 4.3). Hence, the low selectivity to 2-buten-1-ol is probably caused by the faster consumption rate of 2-buten-1-ol than that of 3-buten-1-ol. Here, I would like to mention the production of propene. 3-Buten-1-ol was decomposed into propene over $\text{SiO}_2\text{-Al}_2\text{O}_3$ (Table 4.5), while it was not observed in the reaction of 1,3-butanediol (Table 4.2). This difference is probably attributed to the conditions for each reactant: the reaction of unsaturated alcohols was carried out at twice longer residence-time than that of 1,3-butanediol, *i.e.* using twice amount of catalyst weight, and at high temperature of 250 °C. Such severe conditions may promote the production of propene from 3-buten-1-ol over $\text{SiO}_2\text{-Al}_2\text{O}_3$.

3-Buten-1-ol was the main product from 1,3-butanediol over TiO_2 , while 2-buten-1-ol was produced with high selectivity and 3-buten-2-ol was rarely produced. The lower selectivity to 2-buten-1-ol is not attributed to the consecutive dehydration into butadiene because butadiene was not formed over TiO_2 (Table 4.2). In the reaction of 2-butanol over TiO_2 , *cis*-2-butene was mainly obtained, and the selectivity to 1-butene was higher than that to *trans*-2-butene (Table 4.4). In the reaction of 1,3-butanediol, however, *cis*-2-buten-1-ol was less selective than *trans*-2-buten-1-ol; the selectivities to *cis*- and *trans*-2-buten-1-ol were 3.2 and 8.0 mol% at 350 °C, respectively. The formation of *cis*-2-buten-1-ol may be restricted by the large steric hindrance induced by the OH group at 3-position in 1,3-butanediol, and thus, 3-buten-1-ol would be mainly produced over TiO_2 .

Although ZrO_2 had the weakest acidity among the catalysts employed in this study, its activity was comparable to that of TiO_2 (Fig. 4.1). Thus, the dehydration of 1,3-butanediol probably does not proceed with acid-catalyzed mechanism over ZrO_2 . Recently, I have reported the selective dehydration of 1,4-butanediol into 3-buten-1-ol over ZrO_2 and concluded that the acid-base property of ZrO_2 plays a crucial role in the reaction [22,23]. It is speculated that 1,3-butanediol also dehydrated in the same mechanism as in the case of 1,4-butanediol. Here, I would like to emphasize that the acid-base concerted mechanism rather than simple acid catalysis possibly elucidates the high selectivity to 3-buten-2-ol over ZrO_2 (Table 4.1). Primary OH group in 1,3-butanediol can be readily activated in the mechanism because 1,4-butanediol, which has two primary OH groups, is dehydrated into 3-buten-1-ol [22,23]. In the acid-catalyzed dehydration, primary OH group is less active as mentioned above.

Over TiO_2 and ZrO_2 , the products distribution was very complex. This complexity is caused by the side reactions; hydrogenation and dehydrogenation. The

details are explained in the next section.

Al_2O_3 showed unique catalytic performance in the reaction of 1,3-butanediol: 4-methyl-1,3-dioxane and formaldehyde were obtained with moderate selectivities. 4-Methyl-1,3-dioxane can be produced via acetalization of formaldehyde with 1,3-butanediol and formaldehyde. Formaldehyde would be produced via the reverse-aldol reaction of 4-hydroxy-2-butanone, which is produced by dehydrogenation of OH group at 3-position in 1,3-butanediol. Here, I face a puzzling question: propanone should be produced by the decomposition of 4-hydroxy-2-butanone. However, the amount of propanone does not match with that of formaldehyde (Table 4.2). At this point, these phenomena are not explainable.

4.4.3 *Reaction pathway from 1,3-BDO to products*

Several products were observed over the catalysts. Unsaturated ethers (17 in Table 4.1) were formed only over $\text{SiO}_2\text{-Al}_2\text{O}_3$. This would be attributed to the low reaction temperature over $\text{SiO}_2\text{-Al}_2\text{O}_3$. Generally, etherification of alcohols proceeds at lower temperature because synthesis of ethers from alcohols is a kinetic control reaction.

3-Buten-2-one was the major by-product from 1,3-butanediol over TiO_2 and ZrO_2 , and it can be synthesized via two routes: one is the dehydration of 4-hydroxy-2-butanone that is produced by dehydrogenation of 1,3-butanediol, and another is the dehydrogenation of 3-buten-2-ol. It is deduced that the former route is probable because TiO_2 and ZrO_2 mainly catalyzed the dehydration of monoalcohols (Tables 4.3 and 4.4), although 3-buten-2-one was produced with the selectivity of 10.7 mol% in the reaction of 3-buten-2-ol over TiO_2 (Table 4.6). In Chapter 3, I discussed that the dehydration of 4-hydroxy-2-butanone over TiO_2 and it is dehydrated at the

reaction temperature as low as 160 °C [24]. The produced 3-buten-2-one is probably hydrogenated into butanone, and it may be further hydrogenated to produce 2-butanol. 2-Butanol can be also produced by the hydrogenation of 3-buten-2-ol.

4-Hydroxy-2-butanone is easily decomposed into propanone and formaldehyde at temperatures above 240 °C [24]. The acetalization of formaldehyde with 1,3-butanediol effectively proceeds over Al_2O_3 , as discussed in the previous section.

The dehydrogenation of OH group at 1-position in 1,3-butanediol produces acetaldol, and it would be decomposed into acetaldehyde at the reaction temperature. Thus produced acetaldehyde could be hydrogenated into ethanol.

1-Butanol would be produced by the hydrogenation of 3-buten-1-ol and 2-buten-1-ol. 2-Butenal is obtained by the dehydrogenation of 2-buten-1-ol. Butanal can be produced via dehydrogenation of 1-butanol and hydrogenation of 2-butenal.

Here, I summarize the probable reaction pathways from 1,3-butanediol to products detected in this work as shown in Scheme 4.1.

4.5 Conclusion

The reaction of 1,3-butanediol over several catalysts with different acid-base properties was investigated. The catalytic activity was ruled by its acidity. The strong acid sites of $\text{SiO}_2\text{-Al}_2\text{O}_3$ catalyzed the dehydration of 1,3-butanediol into unsaturated alcohols, which was further dehydrated into 1,3-butadiene at high conversion level. The weak acidic catalysts, TiO_2 and ZrO_2 , promoted not only the dehydration of 1,3-butanediol but also several side reactions such as hydrogenation and dehydrogenation. As the consequence, the products distribution was complex over these catalysts. Al_2O_3 enhanced the decomposition of 1,3-butanediol into formaldehyde. The produced formaldehyde and 1,3-butanediol formed an acetal

compound, 4-methyl-1,3-dioxane.

References in Chapter 4

- [1] A. L. Gemal, J. Luche, *J. Am. Chem. Soc.* **103** (1981) 5454-5459.
- [2] T. Ohkuma, H. Ooka, T. Ikariya, R. Noyori, *J. Am. Chem. Soc.* **117** (1995) 10417-10418.
- [3] M. Hernandez, P. Kalck, *J. Mol. Catal. A* **116** (1997) 131-146.
- [4] P. S. Gradeff, G. Formica, *Tetrahedron Lett.* **17** (1976) 4681-4684.
- [5] Z. Poltarzewski, S. Galvagno, R. Pietropaolo, P. Staiti, *J. Catal.* **102** (1986) 190-198.
- [6] D. G. Blackmond, R. Oukaci, B. Blanc, P. Gallezot, *J. Catal.* **131** (1991) 401-411.
- [7] M. De bruyn, D. E. De Vos, P. A. Jacobs, *Adv. Synth. Catal.* **344** (2002) 1120-1125.
- [8] P. Claus, *Appl. Catal. A* **291** (2005) 222-229.
- [9] C. Milone, R. Ingoglia, A. Pistone, G. Neri, F. Frusteri, S. Galvagno, *J. Catal.*, **222** (2004) 348-356.
- [10] S. Sato, R. Takahashi, T. Sodesdawa, N. Honda, H. Shimizu, *Catal. Commun.*, **4** (2003) 77-81.
- [11] S. Sato, R. Takahashi, T. Sodesdawa, N. Honda, *J. Mol. Catal. A* **221** (2004) 177-183.
- [12] S. Sato, R. Takahashi, T. Sodesdawa, N. Yamamoto, *Catal. Commun.*, **5** (2004) 397-400.
- [13] N. Ichikawa, S. Sato, R. Takahashi, T. Sodesawa, *J. Mol. Catal. A* **231** (2005) 181-189.
- [14] J. McMurry, *Fundamentals of Organic Chemistry, third ed*, Brooks/ Cole, California, 1994.
- [15] S. Sato, K. Takematsu, T. Sodesawa, F. Nozaki, *Bull. Chem. Soc. Jpn.*, **65** (1992)

1486-1490.

[16] B. H. Davis, P. Ganesan, *Ind. Eng. Chem. Prod. Res. Dev.*, **18** (1979) 191-198.

[17] S. Chokkaram, B. H. Davis, *J. Mol. Catal. A*, **118** (1997) 89-99.

[18] H. Hattori, *Appl. Catal. A*, **222** (2001) 247-259.

[19] N. Ichikawa, S. Sato, R. Takahashi, T. Sodesawa, K. Inui, *J. Mol. Catal. A*, **212** (2004) 197-203.

[20] K. Inui, T. Kurabayashi, S. Sato, *J. Catal.*, **212** (2002) 207-215.

[21] K. Inui, T. Kurabayashi, S. Sato, N. Ichikawa, *J. Mol. Catal. A*, **216** (2004) 147-156.

[22] N. Yamamoto, S. Sato, R. Takahashi, K. Inui, *Catal. Commun.*, **6** (2005) 480-484.

[23] N. Yamamoto, S. Sato, R. Takahashi, K. Inui, *J. Mol. Catal. A*, **243** (2006) 52-59.

[24] N. Ichikawa, S. Sato, R. Takahashi, T. Sodesawa, *Catal. Commun.*, **6** (2005) 19-22.

Table 4.1 Specific surface area and acid and base property of catalyst

Catalyst	SA ^a / m ² g ⁻¹	NH ₃ -TPD		CO ₂ -TPD	
		T ^b / °C	A ^c / μmol g ⁻¹	T ^b / °C	A ^c / μmol g ⁻¹
SiO ₂ -Al ₂ O ₃	420	303	440	-	0
Al ₂ O ₃	200	345	166	113	333
TiO ₂	40	342	30.8	-	0
ZrO ₂	100	214	10.4	115	232

^a Specific surface area.

^b Temperature at which the desorption peak centered.

^c Number of acid or base sites.

Table 4.2 Reaction of 1,3-BDO over SiO₂-Al₂O₃, Al₂O₃, TiO₂ and ZrO₂.

Catalyst	Temp. / °C	Conv. / %	Selectivity ^a / mol%																
			1	2	3	4	5	6	7	8	9	10	11	12	13	14	15	16	17
SiO ₂ -Al ₂ O ₃	200	18.6	43.8	14.2	2.1	1.3	0	1.4	0	0	0	0	0	0	0	5.5	0	19.6	12.1
	225	45.9	36.7	9.6	3.2	2.4	0	2.8	0	0	0	0	0	2.4	0	6.4	3.5	30.0	3.0
	250	74.3	27.7	3.2	2.9	4.1	0	3.5	0.3	0.4	3.8	1.5	0.2	0.3	0.6	6.6	7.7	36.0	1.2
Al ₂ O ₃	225	4.7	25.8	9.2	0	0	5.2	0	0	0	0	0	0	0	0	28.8	31.0	0	0
	250	49.3	15.4	4.4	0	8.6	6.5	2.0	0	2.2	1.1	9.5	0	0.9	3.1	18.4	27.9	0	0
	275	89.1	17.0	2.2	0	7.5	5.2	0.3	0	4.0	2.3	2.5	0.6	0.8	7.2	22.1	28.3	0	0
TiO ₂	325	8.4	27.3	19.6	4.9	13.5	10.5	9.1	7.3	0	0	3.4	0	4.4	0	0	0	0	0
	350	55.7	20.8	10.5	2.8	18.6	8.4	11.8	9.5	1.4	3.5	1.2	0.7	2.4	3.1	0	5.3	0	0
	375	84.0	30.2	7.3	2.1	16.0	6.6	5.3	4.1	1.8	4.2	3.7	1.9	2.0	3.0	0	11.8	0	0
ZrO ₂	325	25.3	25.9	18.7	16.3	14.0	0	1.7	2.3	4.0	8.1	5.3	0	0.6	3.1	0	0	0	0
	350	57.3	18.3	14.5	12.6	11.4	0	2.4	5.0	3.6	11.0	9.9	0.8	-	4.7	0	2.7	3.1	0
	375	71.4	20.0	9.6	12.1	13.8	0	2.9	4.7	3.8	15.4	9.3	1.2	0.9	2.4	0	-	3.9	0

^a The abbreviation of the products are as follows; **1**: 3-buten-1-ol, **2**: 2-buten-1-ol, **3**: 3-buten-1-ol, **4**: 3-buten-2-ol, **5**: 2-butenal, **6**: 1-butanol, **7**: 2-butanol, **8**: ethanol, **9**: methanol, **10**: butanone, **11**: butanal, **12**: propanone, **13**: acetaldehyde, **14**: 4-methyl-1,3-dioxane, **15**: formaldehyde, **16**: 1,3-butadiene, **17**: ethers derived from the dimerization of produced unsaturated alcohols.

^b Catalyst weight, 0.150 g.

Table 4.3 Reaction of 1-butanol over SiO₂-Al₂O₃, TiO₂, and ZrO₂^a

Catalyst	Temp. ^b /°C	Conv. ^c /%	Selectivity / mol%				
			1-butene	<i>t</i> -2-butene	<i>c</i> -2-butene	butanal	others ^d
SiO ₂ -Al ₂ O ₃	225	28.4	24.9	36.0	32.2	2.8	4.1
TiO ₂	350	11.7	52.7	11.4	15.9	7.5	12.5
ZrO ₂	350	3.3	59.2	0	0	11.7	29.1

^a The reaction was carried out under following conditions: catalyst weight, 0.150 g; reactant feed rate, 1.7 cm³ h⁻¹; carrier gas, N₂ (30 cm³ min⁻¹).

^b Reaction temperature.

^c Conversion.

^d Others are di-*n*-butyl ether and butyl butyrate.

Table 4.4 Reaction of 2-butanol over SiO₂-Al₂O₃, TiO₂, and ZrO₂^a

Catalyst	Temp. ^b /°C	Conv. ^c /%	Selectivity / mol%				
			1-butene	<i>t</i> -2-butene	<i>c</i> -2-butene	butanone	others ^d
SiO ₂ -Al ₂ O ₃	225	76.1	14.4	45.3	37.8	1.0	1.5
TiO ₂	350	63.8	31.0	18.4	41.3	7.5	1.8
ZrO ₂	350	39.2	70.5	7.5	8.9	10.4	2.7

^a The reaction conditions are the same as those in Table 4.3.

^b Reaction temperature.

^c Conversion.

^d Others are not identified.

Table 4.5 Reaction of unsaturated alcohols over SiO₂-Al₂O₃ at 250 °C^a

Reactant	Conv. / %	Selectivity ^b / mol%
1	41.5	18 ^c (58.0), 16 (12.8), 5 (11.0), 11 (6.9), 9 (5.6)
2	76.7	16 (92.8), 5 (5.3)
3	70.8	16 (93.0), 2 (2.6), 12 (2.0)

^a The reaction was carried out under following conditions: catalyst weight, 0.300 g; reactant feed rate, 1.7 cm³ h⁻¹; carrier gas, N₂ (30 cm³ min⁻¹).

^b Numbers of the reactants and of the products except **18** are the same as those in Table 2, and numbers in parentheses indicate the selectivity.

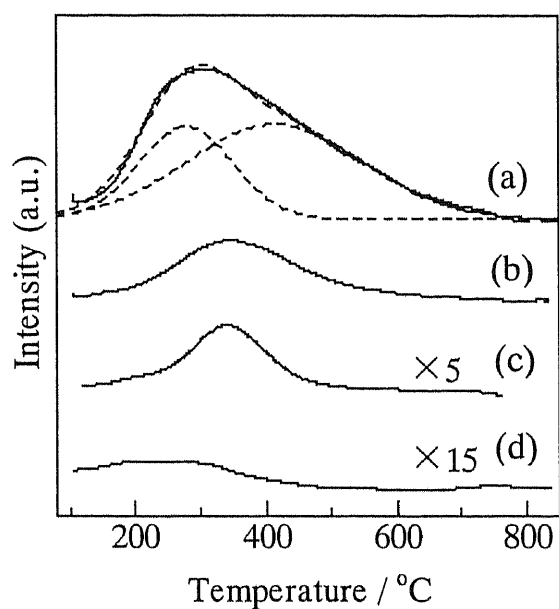
^c Propene.

Table 4.6 Reaction of unsaturated alcohols over TiO₂ at 375 °C^a

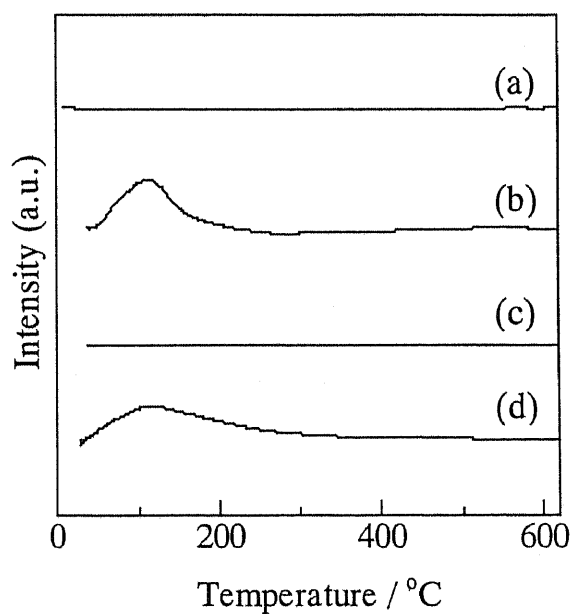
Reactant	Conv. / %	Selectivity ^b / mol%
1	38.2	16 (50.0), 13 (13.2), 9 (11.4), 5 (8.1), 6 (4.0)
2	53.3	16 (71.3), 5 (11.9), 9 (3.3)
3	70.2	16 (70.2), 4 (10.7), 10 (4.0)

^a The reaction conditions are the same as those in Table 4.5 except for the temperature.

^b Numbers of the reactants and of the products are the same as those in Table 4.2, and numbers in parentheses indicate the selectivity.



(A)



(B)

Fig. 4.1 TPD profiles of (a) $\text{SiO}_2\text{-Al}_2\text{O}_3$, (b) Al_2O_3 , (c) TiO_2 , (d) ZrO_2 . The probe molecules are (A) NH_3 , (B) CO_2 . The dotted lines in Fig. 4.1A are the deconvolution of the profile of $\text{SiO}_2\text{-Al}_2\text{O}_3$ according to Gaussian fitting

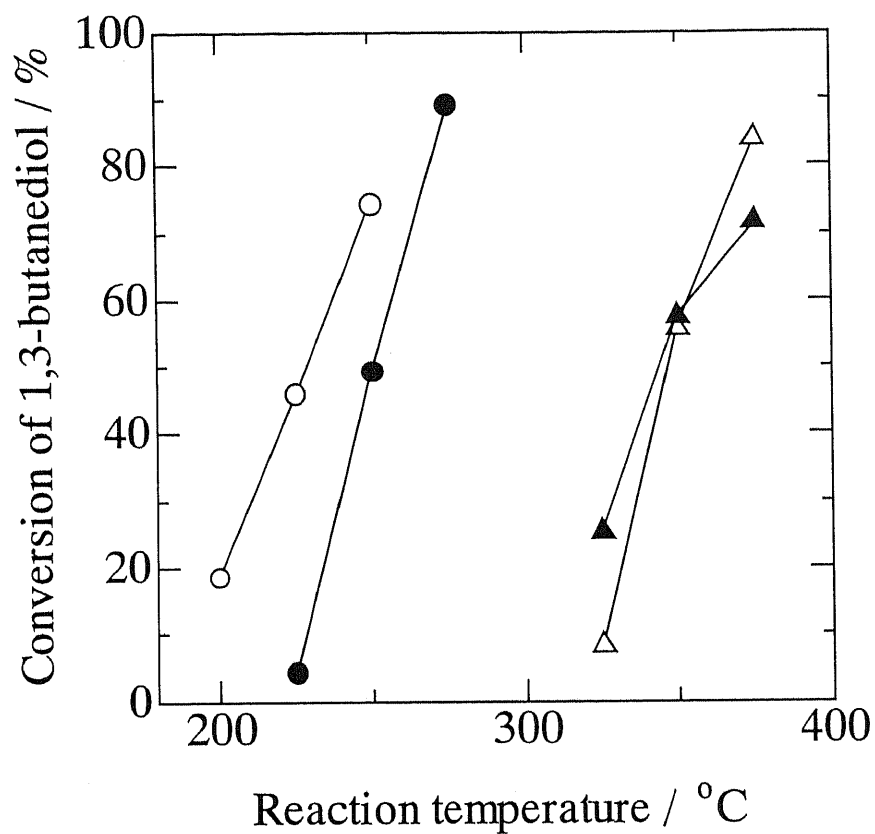
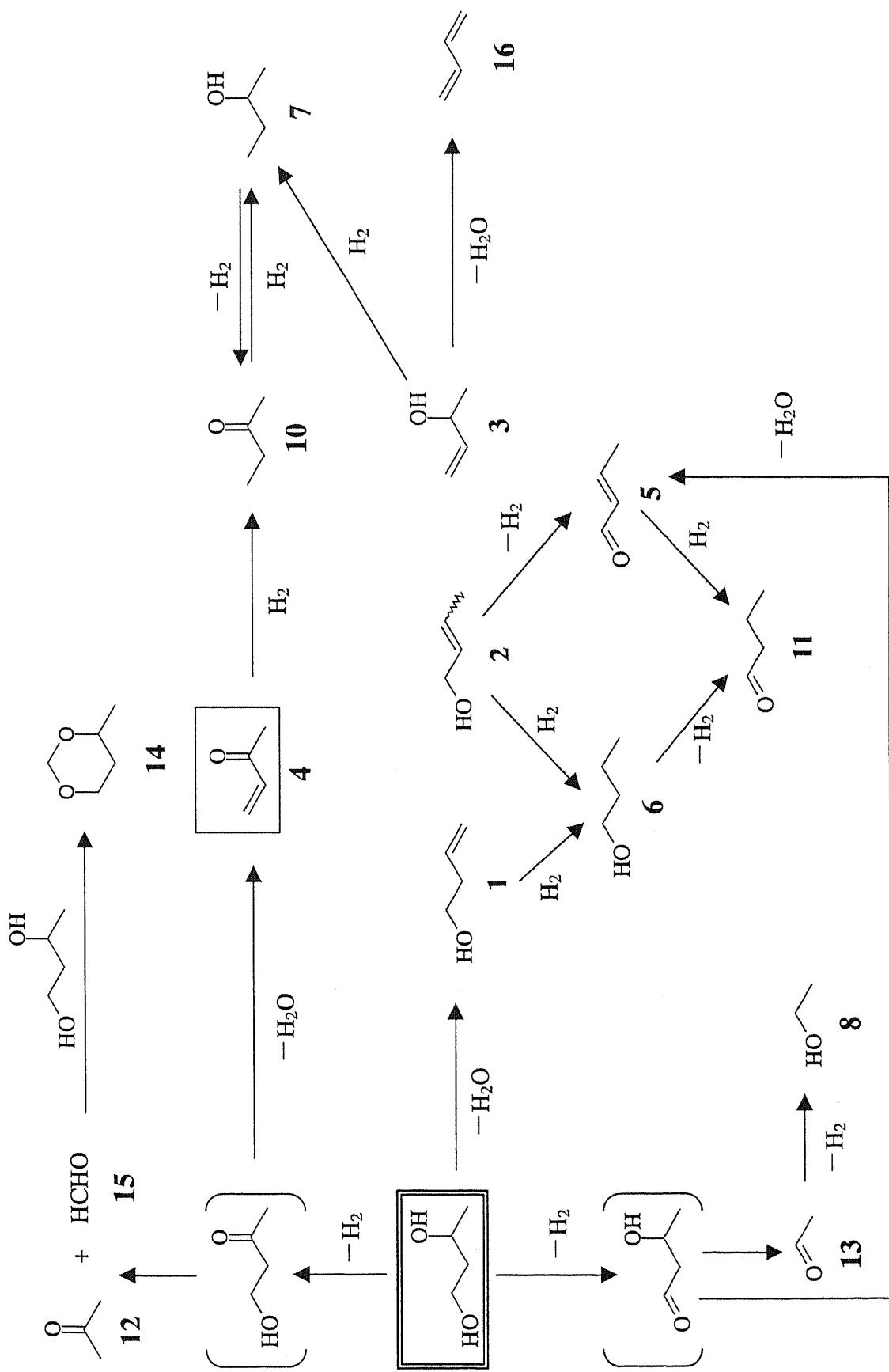


Fig. 4.2 Relationship between 1,3-BDO conversion and reaction temperature over several metal-oxide catalysts. (open circle) SiO₂-Al₂O₃, (closed circle) Al₂O₃, (open triangle) TiO₂, (closed triangle) ZrO₂.



Scheme 4.1 Probable reaction pathway from 1,3-BDO to products over catalysts. The numbers below the products are the same as those listed in Table 4.1.

Chapter 5

Reaction of 1,3-butanediol over CeO₂

5.1 Introduction

CeO₂ is an important component as the support of three-way catalyst, which is served to decompose the exhaust of automobile into nontoxic CO₂, N₂ and H₂O. It is also used in the organic synthesis such as dehydrogenation of ethylbenzene into styrene [1], *ortho*-selective alkylation phenol employing alcohols as the alkylation reagent [2-4] and symmetric ketone formation from primary alcohols [4-10] and carboxylic acid [11-14].

As mentioned in Chapter 1, CeO₂ effectively activates 1,3-diols in the formation of unsaturated alcohols [15-17]. It is well known that alcohols are dehydrated with acid and base catalyst [18]. As shown in the previous chapter, however, solid acid catalysts are not suitable for the efficient production of unsaturated alcohols from 1,3-BDO: side reactions such as dehydrogenation, decomposition, consecutive reaction of produced unsaturated alcohols decrease the selectivity to them.

It is considered that redox property of CeO₂ plays a crucial roll in the dehydration of 1,3-diols [15-17], and that oxygen-defect site of most stable CeO₂ (111) surface would be the active site for the dehydration of 1,3-diols [17]. However, there are some questions: (i) is really (111) surface active for 1,3-diols dehydration? (ii) how many defects exist on CeO₂ surface? and (iii) does 1,3-diols adsorb on oxygen-defect site of CeO₂ (111) ?

In this chapter, in order to investigate the above issues, the factors that affect the catalytic performance of CeO₂ and the active site for the dehydration of 1,3-diols are discussed. 1,3-BDO is used as the representative of 1,3-diol. Furthermore, the

reaction mechanism of 1,3-diol dehydration over CeO₂ is also discussed. CeO₂ catalysts with different specific surface area are employed to confirm the effects on catalytic performance. Computational techniques based on Density Functional Theory (DFT) and Paired Interacting Orbital (PIO) theory are also used to investigate the adsorption of 1,3-BDO and reaction mechanism, respectively.

5.2 Experimental

5.2.1 Characterization of CeO₂ samples

X-ray diffraction patterns were recorded on a XRD7000 (Shimadzu, Japan) with the Cu-K α radiation ($\lambda = 0.154$ nm) as the X-ray source.

The specific surface area of the catalyst was calculated with the BET equation using isotherm of the N₂ adsorption at -196 °C. The average particle size of the CeO₂ was estimated with equation, $D = 6 / (S \times d)$ (Eq. (1)), where D , SA and d were average particle size, specific surface area and density of CeO₂ ($d = 7.1$ g cm⁻³), respectively.

Temperature-programmed reduction (TPR) was measured under following procedure. About 30 mg of CeO₂ was fixed in the quartz tube. The H₂/N₂ (H₂ concentration of 10 vol.%) mixed gas was flowed at the rate of 10 cm³ min⁻¹. The catalyst bed was gradually heated from 25 to 900 °C at the heating rate of 5 K min⁻¹ and H₂ consumption was monitored with TCD.

Transmission electron microscopy (TEM, JEM-2010, JEOL) was employed to observe the morphology of CeO₂ particles in the samples calcined at 500 and 1000 °C.

5.2.2 Catalytic reaction

CeO₂ catalysts employed in this study were supplied by Daiichi Kigenso Kagaku Kogyo Co., Ltd. All the catalysts were calcined at 500-1000 °C before the

experiments to control the specific surface area and particle size of CeO₂. The reactions were carried out with conventional fixed-bed down-flow reactor under atmospheric pressure. Prior to the reaction, a CeO₂ sample (0.5-2.0g) was preheated in the flow reactor in N₂ gas flow at 500 °C for 1h. After the catalyst bed had been cooled at the prescribed temperature, reactant was fed into the reactor at a liquid flow rate of 10 cm³ h⁻¹ together with an N₂ flow of 30 cm³ min⁻¹. Effluent samples collected periodically were analyzed by gas chromatography (GC-9A, Shimadzu, Japan) with a capillary column of TC-WAX (30m, GL Science Inc, Japan) over a temperature range controlled from 60 to 200 °C at a heating rate of 10 K min⁻¹. Gaseous products such as 1,3-butadiene were analyzed by on-line gas chromatography (GC-8A, Shimadzu) with a 1-m packed column (Porapak Q). Since the catalytic activity is stable, as reported in Ref. [16], both the conversion of 1,3-BDO and the selectivity to each product are averaged in the initial 5 h to evaluate the catalytic activity.

5.2.3 Calculation method

5.2.3.1 DFT calculation

DFT calculation was performed using DMol³ program mounted on MS Modeling 3.0 package [19,20]. Each CeO₂(111) surface model was geometrically optimized at the level of the local density approximation (LDA) using Vosko-Wilk-Nussair (VWN) functional [21]. Also double-numeric-polarized (DNP) basis set is used [19,20], which is equivalent in accuracy to 6-31G** double zeta class Gaussian orbital basis set. Total electronic energy convergence criteria in the geometrical optimization were set to 10⁻⁴ a.u. (1 a.u. = 2625.5 kJ mol⁻¹) and the self-consistent field (SCF) convergence criteria during geometrical optimization were set to 10⁻⁴ a.u. Only the Γ point in the Brillouin-zone was sampled. Using the

optimized models, a single-point electronic energy calculation was executed at the level of generalized gradient approximation (GGA) of Perdew-Burke-Enzerhof (PBE) functional [22]. DNP basis sets were also used as in the case of geometry optimization. SCF convergence criteria of GGA electronic calculation were set to 10^{-5} a.u. Brillouin-zone integration was performed using $2 \times 2 \times 1$ Monkhorst-Pack grid [23].

CeO₂(111) surface model was constructed as a slab-gap model [24]. First, the optimized bulk structure is sliced along with the specified plane. In the next step, empty space that has adequate height is created along with z-axis and only 2D periodicity is taken into account. Our slab model had six-layer thickness and the height of the empty space was set to 10 Å. Then, lattice parameters of the model, as shown in Fig. 5.7, were $a = b = 15.304$ Å, $c = 14.684$ Å, $\alpha = 60.00$ degree, and $\beta = \gamma = 90.00$ degree. These parameters were fixed during following geometrical optimization.

5.2.3.2 *PIO calculation*

PIO theory presented by Fujimoto et al. [25,26] are executed to analyze the orbital interactions between 1,3-BDO and CeO₂(111) surface with optimum geometry obtained by DFT calculation. All the PIO calculations are executed with quantum chemical application software LUMMOXTM [27]. PIO calculations successfully employed to confirm the interaction between the two substrates and to determine quantitatively the interacting orbital that played an important roll in chemisorption [28-31]. The molecular orbitals are determined by Extended Hückel theory, and the Extended Hückel parameters [32,33] used in this study are listed in Table 1 of Ref. [17]. The algorithm of PIO theory is summarized in literatures [25,26,28-31]. PIO theory quantifies the importance of PIOs between two fragments, A and B. In this study, A

and B are 1,3-BDO and CeO₂(111) surface, respectively. The importance of PIOs is evaluated by eigenvalue (EV), and PIOs are labeled as PIO-n, where n means the sequence of the importance of PIOs: PIO-1 is the most important PIO and PIO-2 is the second most important PIO. Value of overlap population (OP) evaluates the attractive or repulsive role that the PIO plays in the adsorption system: PIO with positive OP plays attractive role in the adsorption, alternatively PIO with negative OP affects repulsively.

5.3 Results

5.3.1 Characterization of CeO₂ catalysts calcined at different temperatures

Table 5.1 summarizes the specific surface area, *SA*, the average particle size, *D*, of CeO₂ calcined at different temperature. With increasing the calcinations temperature, *SA* of CeO₂ decreased whereas *D* increased.

Fig. 5.1 shows the XRD profiles of the CeO₂ with different calcinations temperature. All the peaks were identified from the fluorite structure of CeO₂. The diffraction peaks of the CeO₂ became sharp with decreasing *SA*, i.e. increasing *D*.

Fig. 5.2 shows the TPR profiles of the catalysts. The reducibility of CeO₂ was strongly dependent on *SA*. Three H₂ consumption peaks are observed in temperature ranges of <300, 300-600, and >600 °C. The peaks at <600 °C increased with increasing the *SA*, whereas the peak at >600 °C slightly decreases. The reducibility of CeO₂ samples is summarized in Table 5.1. The H₂ consumption was normalized as the quantity of Ce³⁺ in the TPR process. In the TPR process, 30-40 % of total Ce⁴⁺ cations were reducible. The reducibility at <600 °C increased with increasing *SA*. It should be mentioned that the temperature at which reduction begins becomes lower with increasing *SA*. The reduction begins at ca. 200 °C on the sample calcined at 500 °C,

while its temperature increases to ca. 350 °C on the sample calcined at 1000 °C.

Figs. 5.3 and 5.4 exhibit the TEM images of on the sample calcined at 500 °C and 1000 °C, respectively. The particle sizes of CeO₂ estimated from Figs. 5.3 and 5.4 were 7.2 and 53.0 nm, respectively. The particle of CeO₂ calcined at 500 °C showed spherical shape, whereas that calcined at 1000 °C looked rhombic-like shape.

5.3.2 Reaction of 1,3-BDO over CeO₂

Fig. 5.5 shows changes in conversion and selectivity with *SA* in dehydration of 1,3-BDO at 325 °C. Table 5.2 also summarizes the product distribution in the reaction. In the dehydration, major products were 3-buten-2-ol and *trans*-2-buten-1-ol. By-products such as methanol and ethanol were obtained, while no 1,3-butadiene was detected. The conversion of 1,3-BDO increased with increasing *SA*, and it reached a maximum value of 35.8% at 74 m²g⁻¹. The selectivity to the unsaturated alcohols decreased with increasing *SA*. The sum of the selectivity to the unsaturated alcohols exceeds 97 % at 13 m²g⁻¹. By-products were rarely produced at 13 m²g⁻¹, but the amounts increased with increasing *SA*. Intrinsic activity based on unit surface area, the space-time-yield (STY) of unsaturated alcohols, was estimated with the reaction results. The STY value drastically decreased with increasing *SA*.

5.3.3 Investigation of 1,3-BDO adsorption on CeO₂(111) surface with DFT and PIO calculations

Fig. 5.6 shows the structure of CeO₂(111) surface employed in DFT calculation. Fig. 5.7 depicts the optimized structure of oxygen-defect introduced on the CeO₂(111) surface in the DFT calculations. The relaxation of the surface was observed: the third layer O²⁻ anions around the oxygen-defect were migrated toward the oxygen-defect site,

while the second layer Ce^{4+} cations around the defect migrated toward the opposite direction. The relaxation of the outmost surface O^{2-} anions was hardly observed.

The adsorption geometry of 1,3-BDO on the oxygen-defect site of $\text{CeO}_2(111)$ surface was investigated. Two optimized structures were obtained from different starting geometries for the calculations, as shown in Figs. 5.8 and 5.9. The nomenclature of the atoms in 1,3-BDO was defined as shown in Fig. 5.10. The adsorption modes shown in Figs. 5.8 and 5.9 were depicted as Structures 1 and 2, respectively. In the Structure 1, two oxygen atoms in 1,3-BDO interacted with two Ce^1 and Ce^3 cations. However, in the Structure 2, $\text{H}^{2\alpha}$ atom accessed Ce^2 cation in addition to the interaction between two oxygen atoms in 1,3-BDO and Ce^1 and Ce^3 cations as observed in Structure 1. Another significant difference in the structures was the molecular structure of 1,3-BDO: the molecule in Structure 1 is linear, and that in Structure 2 was ringed through hydrogen bonding of OH groups. The distance in the hydrogen bonding of $\text{H}^1\text{-O}^3$ was 1.884 Å, which was larger than the bond lengths of C-O and C-C. Table 5.3 listed the structure parameter of free and adsorbed 1,3-BDO (Structures 1 and 2). The adsorption energies of the 1,3-BDO onto the oxygen-defect site in Structures 1 and 2 were -98.8 and -102.7 kJ mol^{-1} , respectively (Table 5.4). In Structure 1, the elongation of $\text{C}^2\text{-H}^{2\alpha}$ bond by 0.013 Å after the adsorption, whereas no stretching of C-O bonds was observed. In Structure 2, the bond lengths of $\text{C}^1\text{-O}^1$ and $\text{C}^3\text{-O}^3$ were elongated together with the elongation of $\text{C}^2\text{-H}^{2\alpha}$ bond, while the other bond lengths were rarely changed before and after the adsorption.

A $(\text{Ce}_9\text{O}_{36}\text{H}_{26})^{12-}$ cluster model is built from Structure 2 for the PIO calculations and three cut-out planes (I)-(III) were defined, as shown in Fig. 5.11, to observe the orbital interactions between two oxygen atoms in 1,3-BDO and Ce cations, between $\text{H}^{2\alpha}$ and Ce^2 and between $\text{C}^1\text{-O}^1$ and Ce^1 , respectively. Fig. 5.12 exhibits the

counter maps of PIO-1 to 6. PIOs 1-6 represented the interaction between oxygen atoms in 1,3-BDO and Ce cations (Fig. 5.12a-f). PIOs 1-4 showed in-phase interaction between 1,3-BDO and $(\text{Ce}_9\text{O}_{36}\text{H}_{26})^{12-}$ cluster. In the PIO-3, out-of-phase interaction between O^1 and C^1 induced by in-phase interaction between O^1 and Ce^1 was also observed as shown in Fig. 5.12g. PIO-5 depicted the out-of-phase interaction between $\text{H}^{2\alpha}$ and C^2 , which was induced by in-phase interaction between $\text{H}^{2\alpha}$ and Ce^2 (Fig. 5.12h). In contrast to PIO-5, the out-of-phase interaction between $\text{H}^{2\alpha}$ and C^2 in PIO-6 was not observed, although in-phase interaction between $\text{H}^{2\alpha}$ and Ce^2 was confirmed (Fig. 5.12i). The EV, OP and LCAO representation of PIO-1 to 6 were listed in Table 5.5.

The adsorption of 1,3-BDO on $\text{CeO}_2(111)$ surface without the oxygen defect, namely stoichiometric surface, was also investigated. Fig. 5.13 shows the optimized structure of the 1,3-BDO on the stoichiometric $\text{CeO}_2(111)$ surface (Structure 3). The adsorption energy of Structure 3 was $-82.7 \text{ kJ mol}^{-1}$ (Table 5.4). The structure parameter of Structure 3 was also summarized in Table 5.3. In Structure 3, O-H bonds in 1,3-BDO are elongated.

Additionally, the adsorption of 1- and 2-butanol on oxygen-defected and stoichiometric $\text{CeO}_2(111)$ surface is investigated with DFT calculations. The adsorption energies of 1- and 2-butanol, together with those of 1,3-BDO, on oxygen-defected and stoichiometric $\text{CeO}_2(111)$ surface are summarized in Table 5.4. The adsorption energies of the mono-alcohols were smaller than those of 1,3-BDO on both oxygen-defect site and stoichiometric surface of $\text{CeO}_2(111)$. Figs. 5.14 and 5.15 exhibit the adsorption structure of 1- and 2-butanol on oxygen-defect site of $\text{CeO}_2(111)$, respectively. The 1- and 2-butanol located on oxygen-defect site as filling the oxygen-defect point with O atoms in them.

5.4 Discussion

5.4.1 Defect sites of CeO₂ with different particle sizes

It is known that oxygen defect sites exist in a CeO₂ particle without the reduction by H₂ [34,35]: the concentration of oxygen defect sites increases with decreasing the CeO₂ particle size. Kosacki et al. have reported a relationship between the concentration of oxygen defect, N , and the enthalpy of formation of oxygen defects, ΔH , at the temperature, T , as follows [34]:

$$N = N_0 \exp(-\Delta H / 3kT) \quad (2)$$

where N_0 and k are the concentration of oxygen atoms in CeO₂ lattice, $N_0 = 4.99 \times 10^{22}$ cm⁻³, and Boltzmann constant, respectively. Therefore, it can be described with arranging Eq. (2) as follows:

$$N_{598} = N_0 (N_{300}/N_0)^{300/598} \quad (2')$$

where N_{300} and N_{598} are the concentration of oxygen defects at 27 °C and 325 °C, respectively. Using the reported value of oxygen defect concentration at 27 °C, N_{300} [34], the concentration of oxygen defect at the reaction temperature of 325 °C, N_{598} , is estimated. Assuming that the oxygen defects exist homogeneously within CeO₂ particle, the surface density of oxygen defects per unit surface area at 325 °C, N_s , is estimated with the following Eq. (3):

$$N_s = N_{598} \times F / (d \times SA) \quad (3)$$

where F is the fraction of surface oxygen atoms in the CeO₂ octahedral particle shown in Fig. 5.16. It is defined as follows:

$$\begin{aligned} F &= \frac{\text{The number of surface oxygen atoms assuming all the surfaces are } \{111\}}{\text{The total number of oxygen atoms in CeO}_2 \text{ particle}} \\ &= \frac{\sum n^2 - \sum (n-2)^2}{\sum n^2 + \sum (n-1)^2} = \frac{2n^2 - 2n + 1}{1/3 \times (2n^3 + n)} \end{aligned} \quad (4)$$

where n is the number of oxygen atoms on the side of (111) surface, and is related to the

particle size, D nm (Fig. 5.16), and can be described as follows:

$$D = 0.383 \times 2^{1/2} \times (n - 1) \quad (5)$$

Table 5.6 summarizes the calculation results of the fraction of surface oxygen atoms, F , the concentration, N_{598} , surface density, N_s , and surface fraction of the oxygen defect sites, C , at 325 °C. It is reasonable that both surface density, N_s , and surface fraction of oxygen defect sites, C , decrease with increasing the CeO₂ particle size.

5.4.2 *Characterization of CeO₂ catalysts calcined at different temperatures*

The physical properties of CeO₂ calcined at different temperatures are summarized in Table 5.1: the specific surface area of the catalysts decreases with increasing the calcinations temperature, which is caused by the aggregation of the CeO₂ particle. It is observed that the peaks of XRD profiles sharpen with increasing the calcinations temperature (Fig. 5.1), which apparently reflects the crystal growth of CeO₂. The TEM images of CeO₂ calcined at low and high temperature apparently exhibit the aggregation of CeO₂ particles (Figs. 5.3 and 5.4).

The change in the shape of the particle is also confirmed from spherical particle to rhombic shape. Wang *et al.* investigated the change in the shape of the CeO₂ particles with different size [36]. They reported that CeO₂ particle whose size ranged 3-10 nm is composed of truncated octahedral shape enclosed by {100} and {111} facets, whereas it become octahedral enclosed only by {111} facet with increasing the particle size. This phenomenon is caused by rapid growth of the particle along <100>, which results in the disappearance of {100} facet. It is reasonable to consider that CeO₂{111} facets become predominant on surface because several researchers reported that {111} facets form the most stable surfaces among other facets of CeO₂ [36-40].

Several researchers have reported the reducibility of pure CeO₂ during the TPR process [41-43]. Bruce *et al.* reported that the TPR of CeO₂ with different SA: reduction peak observed at <700 °C has a linear correlation with SA [41,42]. This is coincident with the present results (Fig. 5.2). In the TPR profiles, the reducibility of CeO₂ by using H₂ consumption was calculated (Table 5.1). The reducibility measured by H₂ consumption at <600 °C is roughly proportional to SA and *F* (Table 5.6). Thus, the TPR peaks at <600 °C can be assigned to be the reduction of surface Ce⁴⁺. In addition, it is obvious that the TPR peak at >600 °C is caused by the reduction of Ce⁴⁺ in the bulk CeO₂.

In Section 5.3.1, it was shown that the temperature at which reduction begins became lower with increasing SA, i.e. decreasing *D*. This is explained by the fact that enthalpy of formation of oxygen defect sites decreases with decreasing the CeO₂ particle size [34]. The number of defect sites also increases with increasing temperature (Eq.2). In Table 5.6, both the surface density and the surface fraction of oxygen defect sites at 325 °C increase with increasing SA of the CeO₂. In particular, the surface fraction of oxygen defect sites, *C* (the last column in Table 5.6), is proportional to SA. In the largest CeO₂ particles, oxygen-defect sites with small density are mostly on the {111} facets because {111} facets would be predominant on the large CeO₂ particle, as discussed in the previous section. In contrast, in the smallest CeO₂ particles, the defects with high density are on the whole facets. In any case, it is reasonable that CeO₂ samples are highly reduced under the reaction conditions tested in this work. The correlation between reducibility of CeO₂ and catalytic activity will be discussed in the following section.

5.4.3 Reaction of 1,3-BDO over CeO₂

The reaction of 1,3-butanediol was carried out using CeO₂ with different particle size. The conversion of 1,3-BDO increased with increasing SA, whereas the selectivity to unsaturated alcohols, mainly 3-buten-2-ol and *trans*-2-buten-1-ol, increased. The increase in the unsaturated alcohols selectivity is attributed by the suppression of by-products production such as methanol and ethanol (Fig. 5.5). The STY of unsaturated alcohols increased with increasing SA, in other word, decreasing the particle size of CeO₂, *D*. These results obviously indicate that the active site for dehydration of 1,3-BDO into unsaturated alcohols increase with increasing *D*. As discussed in the previous sections, the increase in *D* drastically affects the surface morphology of CeO₂: {111} facets become predominate on the surface and the number of oxygen defects decrease. Thus, it is deduced that {111} facets are active for the dehydration of 1,3-butanediol into unsaturated alcohols.

5.4.4 Investigation of the adsorption site of 1,3-BDO on CeO₂(111)

In the previous sections, it is deduced that {111} facets are active for the dehydration of 1,3-butanediol into unsaturated alcohols. Then, the adsorption of 1,3-BDO on oxygen-defect site and stoichiometric CeO₂(111) surface was investigated because oxygen-defects should exist on CeO₂(111) surface to some extent (Table 5.6).

DFT is a powerful tool to investigate the adsorption structure of chemical compounds on the modeled surface, because DFT can take correlation-exchange energy into consideration, which is essential in order to estimate the accurate adsorption energy. In the calculations, well-ordered surface that had no dislocated lattice parts is employed, although they often act as active site in catalysis [49]. Figs. 5.3 and 5.4 show TEM images of the most inactive and active CeO₂ catalyst, respectively. Being judged from

these images, the surface of the most active CeO₂ is flat compared to that of less active one. If the coordinatively unsaturated sites such as step, terrace and kink were active for the dehydration of 1,3-BDO, CeO₂ with the smallest particle would be the most active for the reaction, contrary to the actual result. Therefore, it is considered that stoichiometric or oxygen-defect site on flat CeO₂(111) surface provides the active site.

The adsorption energy of 1,3-BDO on stoichiometric and oxygen-defected site of CeO₂(111) is listed in Table 5.4. The energy of adsorption on oxygen-defect site is larger than that on stoichiometric surface. This indicates that 1,3-BDO preferably adsorbs on oxygen-defect site of CeO₂(111). Two adsorption structures of 1,3-BDO on oxygen-defect site were obtained as shown in Figs. 5.8 and 5.9, named as Structure 1 and 2, respectively. Structure 2 is more stable than Structure 1 by 3.9 kJ mol⁻¹. It also should be noted that C¹-O¹, C³-O³ and C²-H^{2α} bonds are elongated after adsorption in the form of Structure 2 (Table 5.3). This result suggests that these three bonds are activated by the adsorption onto the oxygen-defect site of CeO₂(111) surface, and it also should be mentioned that these activated bonds are well coincident with the reaction result: 3-buten-2-ol and *trans*-2-buten-1-ol are selectively produced over CeO₂. In order to obtain 3-buten-2-ol from 1,3-BDO, the cleavage of C¹-O¹ and C²-H^{2α} bonds is required, and in the same manner, that of C³-O³ and C²-H^{2α} bonds cleavage should occur to produce *trans*-2-buten-1-ol. Hence, it supports that an oxygen-defect site of CeO₂(111) is the active site of the dehydration of 1,3-butanediol.

PIO calculations were executed in order to investigate the orbital interaction between 1,3-BDO and CeO₂(111) surface. Fig. 5.11 shows the (Ce₉O₃₆H₂₆)¹²⁻ cluster-1,3-BDO adsorption structure, which is modeled from Structure 2, for the PIO calculation. As known generally, two Ce⁴⁺ cations are reduced to Ce³⁺ ones per one oxygen-defect formation. The charge of the cluster, -12, assures that two of nine Ce

cations are charged +3 and the others are +4 in the PIO calculation.

The in-phase and out-of-phase interactions between oxygen atoms in 1,3-BDO and Ce cations are observed in PIO-1 to 4 (Fig. 5.12a-d) and PIO-5 (Fig. 5.12e), respectively. It can be comprehend whether the PIO is in-phase or out-of-phase interaction between 1,3-BDO and $(\text{Ce}_9\text{O}_{36}\text{H}_{26})^{12-}$ cluster from OP of each PIO: the OP values of PIOs 1-4 are positive, whereas that of PIO-5 is negative (Table 5.5). Thus, PIOs 1-4 represent that 1,3-BDO is anchored on the oxygen defect site of $\text{CeO}_2(111)$ surface by the interaction between two O atoms and Ce cations.

PIO-3 also shows the out-of-phase interaction between O^1 and C^1 , i.e. 2py orbital of O^1 atom is interacting with opposite phase of 2py orbital of C^1 atom (6th row in Table 5.5). PIO-5 represents the out-of-phase interaction between $\text{H}^{2\alpha}$ and C^2 atoms; 1s orbital of $\text{H}^{2\alpha}$ is interacting with opposite phase of 2s orbital of C^2 atom in PIO-5 (10th row in Table 5.5). They result in the activation of $\text{C}^1\text{-O}^1$ and $\text{C}^2\text{-H}^{2\alpha}$ bonds, and elongation of the bond lengths (Table 5.3), although such interactions are hardly visualized between O^3 and C^3 probably because of the long distance of $\text{O}^3\text{-Ce}^3$, which causes ineffective overlap of the orbitals between O^3 and Ce^3 atoms. In-phase interaction between $\text{H}^{2\alpha}$ and Ce^2 is confirmed in PIO-6, which indicates that 1,3-BDO is coordinated through the interaction between $\text{H}^{2\alpha}$ and Ce^2 atoms. Judging from the counter map of PIO-6 (Fig. 5.12i), it may be considered that PIO-6 represents the out-of-interaction between $\text{H}^{2\alpha}$ and C^2 . However, PIO-6 would not represent the activation of $\text{H}^{2\alpha}\text{-C}^2$ bond because 1s orbital of $\text{H}^{2\alpha}$ interacts with the same phase of 2s orbital and with opposite phase of 2px orbital of C^2 atom (12th row in Table 5.5). The direction of 2px orbital of C^2 atom is vertical to that of $\text{H}^{2\alpha}\text{-C}^2$ bond. Thus, PIO-6 represents only the in-phase interaction between $\text{H}^{2\alpha}$ and Ce^2 .

In addition to $(\text{Ce}_9\text{O}_{36}\text{H}_{26})^{12-}$, other CeO_2 clusters, such as Ce_9O_{18} and $\text{Ce}_{20}\text{O}_{40}$,

with the charge of -2 are built from Structure 2 to confirm the validity of the cluster employed for the series of PIO calculations. The results of the calculation are slightly different among the three CeO₂ clusters, whereas they are essentially the same: 1,3-BDO molecule is anchored by the interaction between two oxygen atoms in 1,3-BDO and Ce cations, and out-of-phase interaction between H^{2α} and C² which is induced by the in-phase interaction between H^{2α} and Ce² are observed. Thus, in the Extended Hückel calculation, it can be said that the charge of the cluster probably gives few effect on the results [44].

5.4.5 Reaction mechanism of 1,3-diols dehydration

The STY of unsaturated alcohols decreased with decreasing the particle size of CeO₂ while the number of the oxygen-defect site on surface increased. In the above discussion, it was concluded that oxygen-defect site on CeO₂(111) surface would be the active site of the dehydration of 1,3-BDO. While facets other than {111} exist on the surface of CeO₂ with small particle and they are not probably active for the dehydration of 1,3-BDO, STY of unsaturated alcohols should increasing with decreasing the particle size. Preliminary, it was proposed that the dehydration of 1,3-diols over CeO₂ proceeds not via the mechanism promoted by acid or base but via redox mechanism [15-17]. In fact, acid or base catalysts are not suitable for the selective dehydration of 1,3-diols into unsaturated alcohols as mentioned in Chapter 4. The acid and base property of CeO₂ was investigated by NH₃- and CO₂-TPD, respectively, and they revealed that CeO₂ has very weak base sites on its surface and the existence of acid sites was hardly confirmed. Hence, the reaction mechanism was proposed as follows (Scheme 5.1): in the initiation step, β-H atom is radically eliminated from 1,3-diols and H radical donates one electron to Ce⁴⁺ cation to reduce Ce³⁺, and H radical itself was

oxidized into proton. Then, one of the OH group was radically eliminated from diol to produce unsaturated alcohol, and Ce^{3+} donates one electron to proton or OH radical to produce H_2O and it was oxidized into Ce^{4+} . Here, it is emphasized that Ce^{4+} plays an important roll in the catalysis. Several researchers observed $\text{CeO}_2(111)$ surface with oxygen-defect by STM [45,46] and AFM [47,48]. On the surface with high oxygen-defect concentration, they reported hat defect are predominantly formed as “line defect” or “triangle defect”, as shown in Fig. 5.18. The most of Ce cations exposed on line defect and triangle defect should be Ce^{3+} , and Ce^{4+} would hardly exist. Therefore, all of the oxygen-defect do not act as active site, and the number of Ce^{4+} cations on oxygen-defect site of $\text{CeO}_2(111)$ surface is the key point to comprehend the catalytic performance.

It has been reported that the reaction of 1,3-BDO over CeO_2 with the specific surface area of $20 \text{ m}^2 \text{ g}^{-1}$ pretreated in H_2 stream at prescribed ranged between 100–900 °C (Table 5.7) [16]. The catalytic activity was rarely affected up to the pretreatment temperature of 600 °C, and it gradually decreased with increasing the temperature above 600 °C. The TPR profile of CeO_2 shows the two peaks; the peak below 600 °C is caused by the reduction of the surface and that above 600 °C is bulk (Fig. 5.2). The specific surface area was not affected up to the reduction temperature of 600 °C. Hence, the number of the surface oxygen defect should increase while the catalytic activity was not improved probably because of the formation of line defects and/or triangle defects. The pretreatment at high temperature above 600 °C, specific surface area drastically decreased with increasing the temperature, which is partly because of the decrease in the catalytic activity, and partly because of the over-reduction of CeO_2 .

While 1,3-diols are dehydrated into unsaturated alcohols at 325 °C, mono-alcohols are mainly dehydrogenated even at the reaction temperature >400 °C

over CeO₂ [16]. The DFT calculation concerning the adsorption of 1- and 2-butanol on oxygen-defect site of CeO₂(111) surface was executed in order to examine the difference in the reactivity between 1,3-diols and mono-alcohols. 1,3-Diol and mono-alcohols adsorb on oxygen-defect site of CeO₂(111) surface in different manner, as shown in Fig. 5.9 and Figs. 5.14 and 5.15, respectively. Three Ce cations are exposed at the oxygen defect site (Fig. 5.7). Two O atoms in 1,3-BDO interact with two Ce cations and β -H atom, i.e. H^{2 α} atom in Fig. 5.12, weakly interacts with another Ce cation, whereas 1- and 2-butanol adsorb as filling the oxygen-defect point and β -H atom in butanols seems not to interact with Ce cation. The difference in the adsorption structure between 1,3-diol and mono-alcohol on oxygen-defect of CeO₂(111) is probably the cause of the difference in the reactivity over CeO₂. As mentioned above, β -H elimination would be the initiation step of the dehydration of 1,3-BDO over CeO₂, and it would be true to in the dehydration of mono-alcohols. However, β -H atom in mono-alcohols does not interact with surface Ce cation (Figs. 5.14 and 5.15). Therefore, the dehydration of mono-alcohols hardly proceed over CeO₂.

5.5 Conclusion

The dehydration of 1,3-BDO into unsaturated alcohols over CeO₂ was investigated. The reaction results were gratefully affected by the particle size of CeO₂. The STY of unsaturated alcohols increased with increasing the particle size of CeO₂, which is because the active facets of {111} became predominate with the growth of CeO₂ particle. The adsorption structure of 1,3-BDO on CeO₂(111) surface was investigated with DFT calculation. 1,3-BDO preferably adsorbs on oxygen-defect sites. It was also confirmed that activation of two C-O bonds and one C-H bond in the methylene group at 2-position in 1,3-BDO after the adsorption, which is coincident with

the reaction products from 1,3-butanediol over CeO₂. The number of oxygen-defect sites on the surface of CeO₂ with different particle size was estimated, and is larger on the smaller particle size. However, all of the oxygen-defects do not act as active site of the selective dehydration of 1,3-BDO into unsaturated alcohols. Oxygen-defect sites are formed as line defect or triangle defect in the region of high oxygen defect concentration, and the most of Ce cations exposed on line defects or triangle oxygen defects are Ce³⁺. It is speculated that the dehydration proceeded via redox of Ce⁴⁺-Ce³⁺-Ce⁴⁺. Hence, over-reduced surface with large number of oxygen-defect sites does not act as active site.

References in Chapter 5

- [1] A. Trovarelli, C. Leitenburg, M. Boaro, G. Dolcetti, *Catal. Today*, **50** (1999) 353-367.
- [2] S. Sato, K. Koizumi, F. Nozaki, *Appl. Catal. A* **133** (1995) L7-L10.
- [3] S. Sato, K. Koizumi, F. Nozaki, *J. Catal.* **178** (1998) 264-274.
- [4] S. Sato, R. Takahashi, T. Sodesawa, K. Mastumoto, Y. Kamimura, *J. Catal.* **184** (1999) 180-188.
- [5] H. Idriss, C. Diagne, J. P. Hindermann, A. Kiennemann, M. Barteau, *J. Catal.* **155** (1995) 219-237.
- [6] A. Yee, S. J. Morrison, H. Idriss, *J. Catal.* **186** (1999) 279-295.
- [7] N. Plint, D. Ghavalas, T. Vally, V. D. Sokolovski, N. J. Coville, *Catal. Today* **49** (1999) 71-77.
- [8] Y. Kamimura, S. Sato, R. Takahashi, T. Sodesawa, M. Fukui, *Chem. Lett.* (2000) 232-233.
- [9] Y. Kamimura, S. Sato, R. Takahashi, T. Sodesawa, T. Akashi, *Appl. Catal. A* **252**

(2003) 399-410.

[10] T. Akashi, S. Sato, R. Takahashi, T. Sodesawa, K. Inui, *Catal. Commun.* **4** (2003) 411-416.

[11] M. Glinski, J. Kijenski, A. Jakubowski, *Appl. Catal. A* **128** (1995) 209-217.

[12] J. Stubenrauch, E. Brosha, J. M. Vohs, *Catal. Today* **28** (1996) 431-441.

[13] T. S. Hendren, K. M. Dooley, *Catal. Today* **85** (2003) 333-351.

[14] O. Nagashima, S. Sato, R. Takahashi, T. Sodesawa, *J. Mol. Catal. A* **227** (2005) 231-239.

[15] S. Sato, R. Takahashi, T. Sodesawa, N. Honda, H. Shimizu, *Catal. Commun.* **4** (2003) 77-81.

[16] S. Sato, R. Takahashi, T. Sodesawa, N. Honda, *J. Mol. Catal. A* **221** (2004) 177-183.

[17] N. Ichikawa, S. Sato, R. Takahashi, T. Sodesawa, *J. Mol. Catal. A* **231** (2005) 181-189.

[18] J. McMurry, *Fundamentals of Organic Chemistry, third ed*, Brooks/ Cole, California, 1994.

[19] B. Delley, *J. Chem. Phys.* **92** (1990) 508-517.

[20] B. Delley, *J. Chem. Phys.* **113** (2000) 7756-7764.

[21] S. J. Vosko, L. Wilk, M. Nusair, *Can. J. Phys.* **58** (1980) 1200-1211.

[22] J.P. Perdew, K. Burke, M. Ernzerhof, *Phys. Rev. Lett.* **77** (1996) 3865-3868.

[23] H. J. Monkhorst, J. D. Pack, *Phys Rev. B* **13** (1976), 5188-5192.

[24] C.R.A. Catlow, L. Ackermann, R.G. Bell, F. Cora, D.H. Gay, M.A. Nygren, J.C. Pereira, G. Sastre, B. Slater, P.E. Sinclair, *Faraday. Disc.* **106** (1997) 1-40.

[25] H. Fujimoto, N. Koga, K. Fukui, *J. Am. Chem. Soc.* **103** (1981) 7452-7457.

[26] H. Fujimoto, *Acc. Chem. Res.* **20** (1987) 448-453.

- [27] T. Motoki, A. Shiga, *J. Computational Chem.* **25** (2004) 106-111.
- [28] A. Shiga, H. Kawamura-Hirabayashi, T. Sasaki, *J. Mol. Catal.* **87** (1994) 243-261.
- [29] A. Shiga, H. Kawamura-Hirabayashi, T. Sasaki, *J. Mol. Catal. A* **98** (1995) 15-24.
- [30] A. Shiga, *J. Mol. Catal. A* **146** (1999) 325-334.
- [31] M. Ishida, T. Suzuki, H. Ichihashi, A. Shiga, *Catal. Today* **87** (2003) 187-194.
- [32] G. Burns, *J. Chem. Phys.* **41** (1964) 1521-1522.
- [33] P. Pyykkö, L.L. Lohr Jr., *Inorg. Chem.* **20** (1981) 1950-1959.
- [34] I. Kosacki, T. Suzuki, H. U. Anderson, P. Colomban, *Solid State Ionics* **149** (2002) 99-105.
- [35] S. Tsunekawa, T. Fukuda, A. Kasuya, *Surf. Sci.* **457** (2000) L437-L440.
- [36] Z. L. Wang, X. Feng, *J. Phys. Chem. B* **107** (2003) 13563-13566.
- [37] S. N. Jacobsen, U. Helmersson, R. Erlandsson, B. Skårman, L. R. Wallenberg, *Surf. Sci.* **429** (1999) 22-33.
- [38] Z. L. Wang, *J. Phys. Chem. B* **104** (2000) 1153-1175.
- [39] T. X. T. Sayle, S. C. Parker, C. R. A. Catlow, *Surf. Sci.* **316** (1994) 329-336.
- [40] J. Conesa, *Surf. Sci.* **339** (1995) 337-352.
- [41] L. A. Bruce, M. Hoang, A. E. Hughes, T. W. Turney, *Appl. Catal. A* **134** (1996) 351-362.
- [42] P. Zimmer, A. Tschoepe, R. Birringer, *J. Catal.* **205** (2002) 339-345.
- [43] Y. Li, A. D. He, Q. Zhu, A. Zhang, B. Zu, *J. Catal.* **221** (2004) 584-593.
- [44] B. Irigoyen, A. Juan, S. Larrondo, N. Amadeo, *Surf. Sci.* **523** (2003) 252-266.
- [45] H. Nörenberg, G. A. D. Briggs, *Surf. Sci.* **402-404** (1998) 734-737.
- [46] H. Nörenberg, G. A. D. Briggs, *Surf. Sci.* **424** (1999) L352-L355.
- [47] K. Fukui, Y. Namai, Y. Iwasawa, *Appl. Surf. Sci.* **188** (2002) 252-256.
- [48] Y. Namai, K. Fukui, Y. Iwasawa, *Catal. Today* **85** (2003) 79-91.

[49] J. M. Thomas, W. J. Thomas, *Introduction to the Principle of Heterogeneous Catalysis*, Academic Press, London, 1981.

Table 5.1 CeO₂ samples used in this study and their physical properties

T _c ^a (°C)	SA ^b (m ² g ⁻¹)	D ^c (nm)	Reducibility ^d (%)		
			<600 °C	>600 °C	Total
500	141	6.0 (8.0)	21.6	22.1	43.7
600	74	11.4 (10.8)	10.7	17.8	28.5
800	42	20.1 (17.4)	4.7	23.9	28.6
900	23	36.7 (26.8)	2.0	26.5	28.5
1000	13	65.0 (37.0)	2.5	27.6	30.1

^a Calcination temperature of CeO₂.

^b Specific surface area calculated by BET method using N₂ isotherm at -196 °C.

^c Particle size of CeO₂ is calculated by Eq. (1), and number in parenthesis indicates a particle diameter estimated by Sherrer's equation in the (111) peak of Fig. 5.1.

^d Ce³⁺/(Ce³⁺ + Ce⁴⁺)

Table 5.2 Catalytic activity in the dehydration of 1,3-BDO at 325 °C.

SA (m ² g ⁻¹)	Conversion ^a		Selectivity (mol%) ^{a,b}									
	(%)		3B2O	t2B1O	c2B1O	1BO	MEK	MeOH	EtOH	AcH	2PO	AcMe
141	35.4		37.2	24.7	1.8	0.6	3.6	17.5	7.1	0.3	0.8	4.2
74	37.1		47.3	32.6	2.1	0.8	1.7	8.9	3.7	0.0	0.0	1.6
42	33.3		53.0	35.0	2.2	0.8	1.0	4.0	2.3	0.2	0.0	1.0
23	28.0		57.6	36.9	1.9	0.5	0.0	1.3	1.1	0.0	0.2	0.1
13	21.2		58.1	37.8	1.9	0.2	0.0	0.4	1.0	0.0	0.0	0.5

^a Average activity in the initial 5 h. $W/F = 0.05 \text{ g h cm}^{-3}$.

^b 3B2O, 3-buten-2-ol; t2B1O, *trans*-2-buten-1-ol; c2B1O, *cis*-2-buten-1-ol; 1BO, 1-butanol; MEK, butanone; MeOH, methanol; EtOH, ethanol; AcH, acetaldehyde; 2PO, 2-propanol; AcMe, propanone..

Table 5.3 Structure parameters for free and adsorbed 1,3-BDO molecule together with the bond length of O¹-Ce, O³-Ce and H^{2a}-Ce ^a.

	bond length ^b / Å			
	free	Structure 1	Structure 2	Structure 3
C ¹ -H ^{1α}	1.114	1.106	1.104	1.107
C ¹ -H ^{1β}	1.103	1.117	1.104	1.107
C ¹ -O ¹	1.401	1.400	<u>1.418</u>	<u>1.425</u>
C ² -H ^{2α}	1.104	<u>1.117</u>	<u>1.113</u>	1.102
C ² -H ^{2β}	1.103	1.104	1.101	1.104
C ³ -H ³	1.105	1.108	1.109	1.109
C ³ -O ³	1.434	1.424	<u>1.451</u>	1.418
C ⁴ -H ^{4α}	1.100	1.100	1.102	1.102
C ⁴ -H ^{4β}	1.100	1.101	1.102	1.100
C ⁴ -H ^{4γ}	1.103	1.102	1.102	1.102
O ¹ -H ^{O1}	0.986	<u>1.202</u>	0.986	<u>1.037</u>
O ³ -H ^{O3}	0.973	0.977	<u>0.984</u>	<u>1.510</u>
O ¹ -Ce ¹	-	2.496	2.565	2.481
O ³ -Ce ³	-	2.641	2.673	2.378
H ^{2α} -Ce ²	-	3.279	2.500	3.194

^a The nomenclature of each atom is the same as shown in Fig. 5.10.

^b Under-lined numbers mean large change in the bond length after adsorption.

Table 5.4 Adsorption energies of 1-, 2-butanol and 1,3-BDO on oxygen-defected and stoichiometric CeO₂(111) surface ^a.

Adsorbate	oxygen-defect site	stoichiometric surface
1-butanol	-80.1	-64.5
2-butanol	-46.6	-66.2
1,3-BDO	-98.8, -102.7	-82.7

^a The unit of energy is kJ mol⁻¹.

Table 5.5 Eigenvalue, overlap population and LCAO representation of PIO-n (n = 1-6)

n	Eigenvalue (EV)	Overlap population (OP)	Component ^a
1	0.863	0.0440	$\psi_1 = -0.151 \text{ Ce}^1_{5dx^2-y^2} + 0.137 \text{ Ce}^1_{5py} + 0.077 \text{ Ce}^1_{6s} + \dots$
			$\varphi_1 = -0.682 \text{ O}^1_{2py} + 0.301 \text{ O}^1_{2pz} - 0.242 \text{ O}^3_{2py} - 0.214 \text{ O}^3_{2pz} - 0.209 \text{ C}^1_{2pz} + \dots$
2	0.217	0.0202	$\psi_2 = +0.160 \text{ Ce}^3_{5dyz} - 0.124 \text{ Ce}^2_{5dxy} - 0.119 \text{ Ce}^3_{5dx^2-y^2} + \dots$
			$\varphi_2 = -0.426 \text{ O}^3_{2py} + 0.357 \text{ C}^2_{2py} - 0.349 \text{ O}^1_{2px} + 0.278 \text{ H}^{2\beta}_{1s} - 0.264 \text{ O}^1_{2pz} + \dots$
3	0.097	0.0062	$\psi_3 = +0.207 \text{ Ce}^3_{5py} - 0.143 \text{ Ce}^1_{5py} - 0.108 \text{ Ce}^3_{5dyz} + \dots$
			$\varphi_3 = +0.315 \text{ C}^3_{2py} - 0.299 \text{ C}^4_{2py} - 0.214 \text{ C}^1_{2py} + 0.214 \text{ O}^1_{2py} - 0.178 \text{ O}^3_{2pz} + \dots$
4	0.083	0.0249	$\psi_4 = -0.210 \text{ Ce}^3_{5dyz} + 0.185 \text{ Ce}^3_{5dx^2-y^2} + 0.106 \text{ Ce}^1_{5py} + \dots$
			$\varphi_4 = +0.698 \text{ O}^3_{2py} - 0.353 \text{ O}^1_{2py} + 0.266 \text{ O}^3_{2pz} - 0.199 \text{ O}^1_{2px} + 0.172 \text{ C}^3_{2px} + \dots$
5	0.032	-0.0409	$\psi_5 = -0.430 \text{ Ce}^1_{5py} - 0.309 \text{ Ce}^1_{6s} - 0.232 \text{ Ce}^2_{5py} - 0.195 \text{ Ce}^2_{6s} - 0.174 \text{ Ce}^2_{5px} + \dots$
			$\varphi_5 = -0.363 \text{ C}^1_{2py} + 0.288 \text{ C}^2_{2s} - 0.276 \text{ O}^1_{2py} + 0.224 \text{ O}^1_{2s} - 0.128 \text{ H}^{2\alpha}_{1s} + \dots$
6	0.024	0.0199	$\psi_6 = +0.389 \text{ Ce}^1_{5py} + 0.353 \text{ Ce}^1_{5dx^2-y^2} - 0.272 \text{ Ce}^1_{6s} - 0.104 \text{ Ce}^2_{5px} - 0.100 \text{ Ce}^2_{5py} + \dots$
			$\varphi_6 = -0.344 \text{ O}^1_{2pz} - 0.272 \text{ O}^1_{2s} + 0.208 \text{ C}^2_{2s} + 0.181 \text{ C}^2_{2px} - 0.150 \text{ H}^{2\alpha}_{1s} + \dots$

^a ψ and φ represent molecular orbitals of $(\text{Ce}_9\text{O}_{36}\text{H}_{26})^{12-}$ cluster and 1,3-BDO, respectively.

Table 5.6 CeO₂ samples used in this study and their physical properties

<i>SA</i> (m ² g ⁻¹)	<i>D</i> (nm)	<i>n</i> ^a	<i>F</i> ^b	<i>N</i> ₃₀₀ ^c (cm ⁻³)	<i>N</i> ₅₉₈ ^d (cm ⁻³)	<i>N_s</i> ^e (nm ⁻²)	<i>C</i> ^f (%)
141	6.0	12	0.227	1.3×10 ²⁰	2.5×10 ²¹	0.57	7.2
74	11.4	22	0.130	1.8×10 ¹⁹	9.4×10 ²⁰	0.23	2.9
42	20.1	38	0.0768	1.7×10 ¹⁸	2.9×10 ²⁰	0.074	0.94
23	36.7	69	0.0432	5.0×10 ¹⁷	1.6×10 ²⁰	0.042	0.53
13	65.0	121	0.0246	2.9×10 ¹⁷	1.2×10 ²⁰	0.032	0.41

^a Number of oxygen atoms consisting the particle with the *D* is calculated by Eq. (5).

^b Fraction of surface oxygen atoms is calculated by Eq. (4).

^c Concentration of oxygen defect at 27 °C is cited from Ref. [34].

^d Concentration of oxygen defect at 325 °C is calculated by Eq. (2').

^e Surface density of oxygen defect sites at 325 °C is calculated by Eq. (3).

^f Percentage expression of surface oxygen defects is estimated by using that the concentration of outmost oxygen of 7.9 nm⁻², which is cited from Ref. [48].

Table 5.7 Effect of H₂ pretreatment of CeO₂ on the catalytic reaction of 1,3-BDO at 325 °C^{a, b, c}

Pretreatment (°C)	Conversion (%)	Selectivity (mol%)		SA (m ² g ⁻¹)
		3-buten-1-ol	<i>trans</i> -2-buten-1-ol	
100	61.6	56.1	35.6	20.4
250	60.0	56.2	34.9	-
325	60.3	56.2	34.9	-
500	59.4	56.1	35.4	20.3
600	57.5	54.5	35.3	18.4
700	41.0	53.9	36.7	9.0
800	29.6	52.3	36.4	2.3
900	10.8	51.8	35.2	2.1

^a Reaction results are cited by Ref. [16].

^b The samples are pretreated under H₂ flow of 73 mmol h⁻¹ for 1 h at prescribed temperature.

^c Reaction was carried out under following conditions: catalyst weight: 0.3 g, reactant feed rate: 2.01 cm³ h⁻¹, carrier gas : N₂ (flow rate 73 mmol h⁻¹).

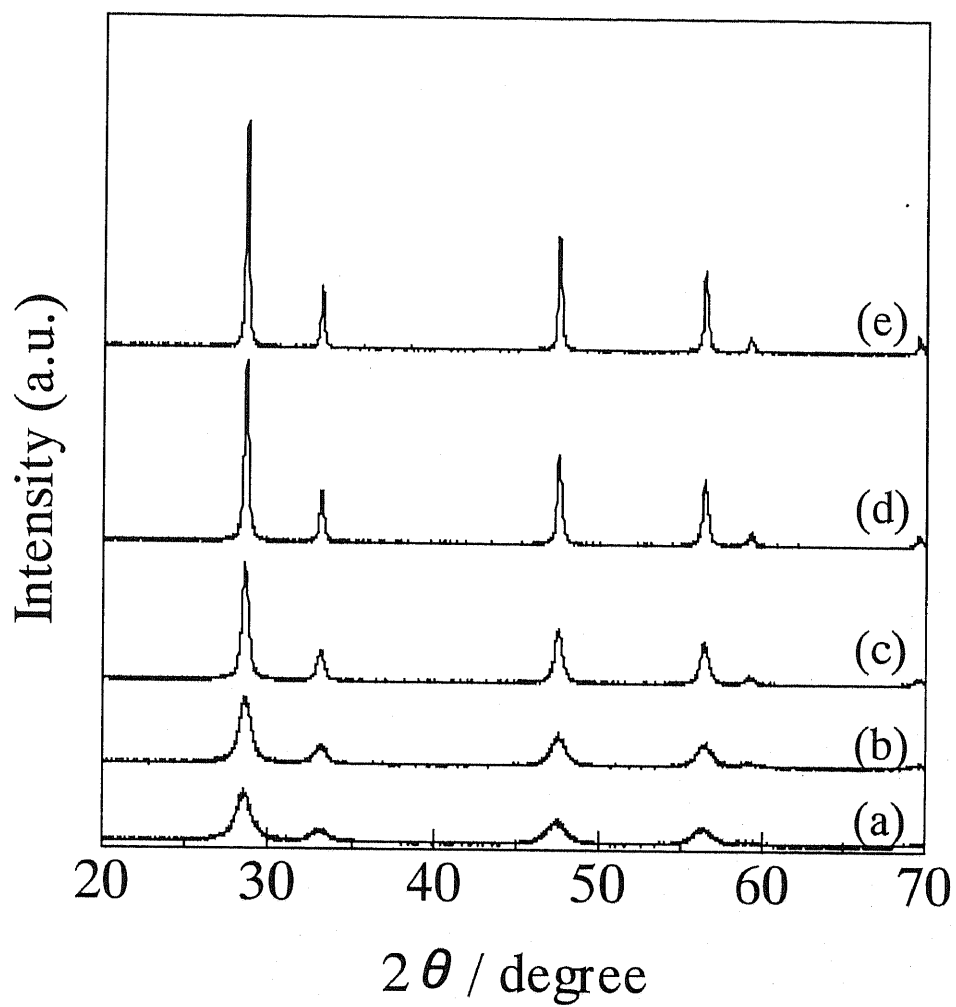


Fig. 5.1 XRD profiles of CeO₂ with different calcinations temperature, Tc. Tc is (a) 500, (b) 600, (c) 800, (d) 900, (e) 1000 °C.

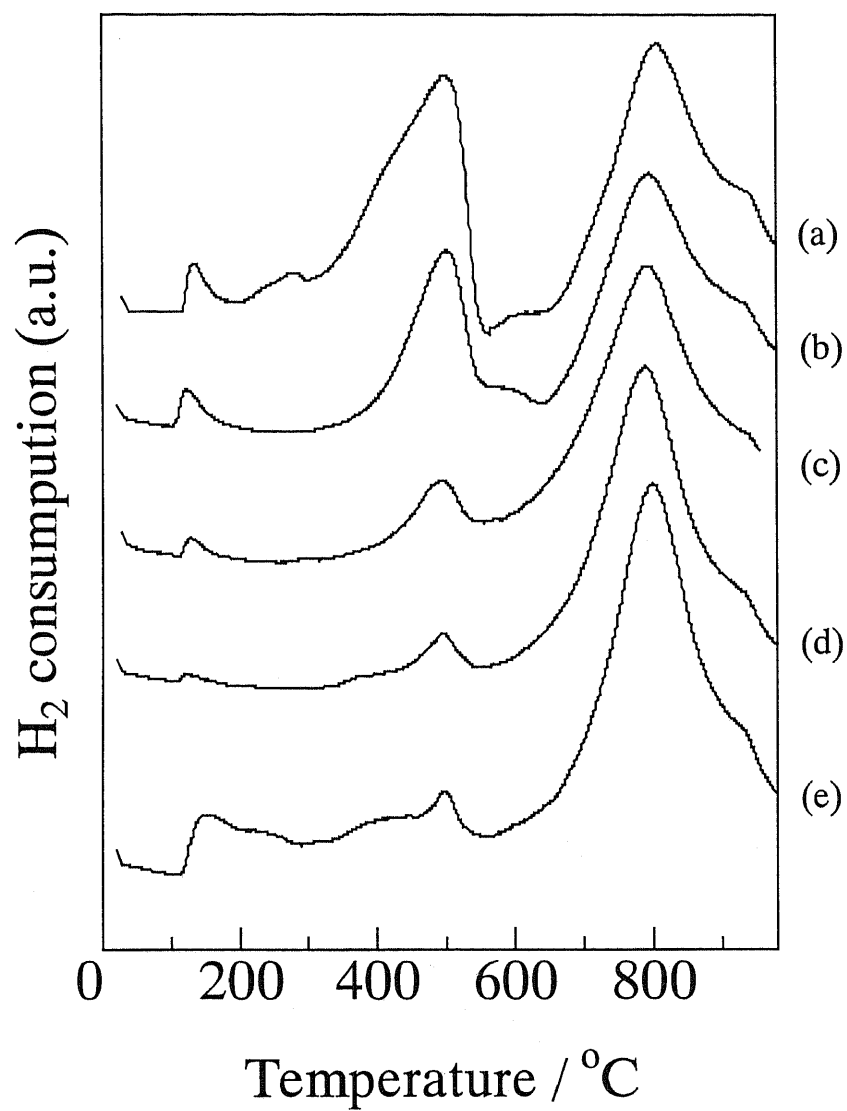


Fig. 5.2 TPR profiles of CeO₂ with different specific surface area. The samples were calcined at (a) 500, (b) 600, (c) 800, (d) 900, (e) 1000 °C.

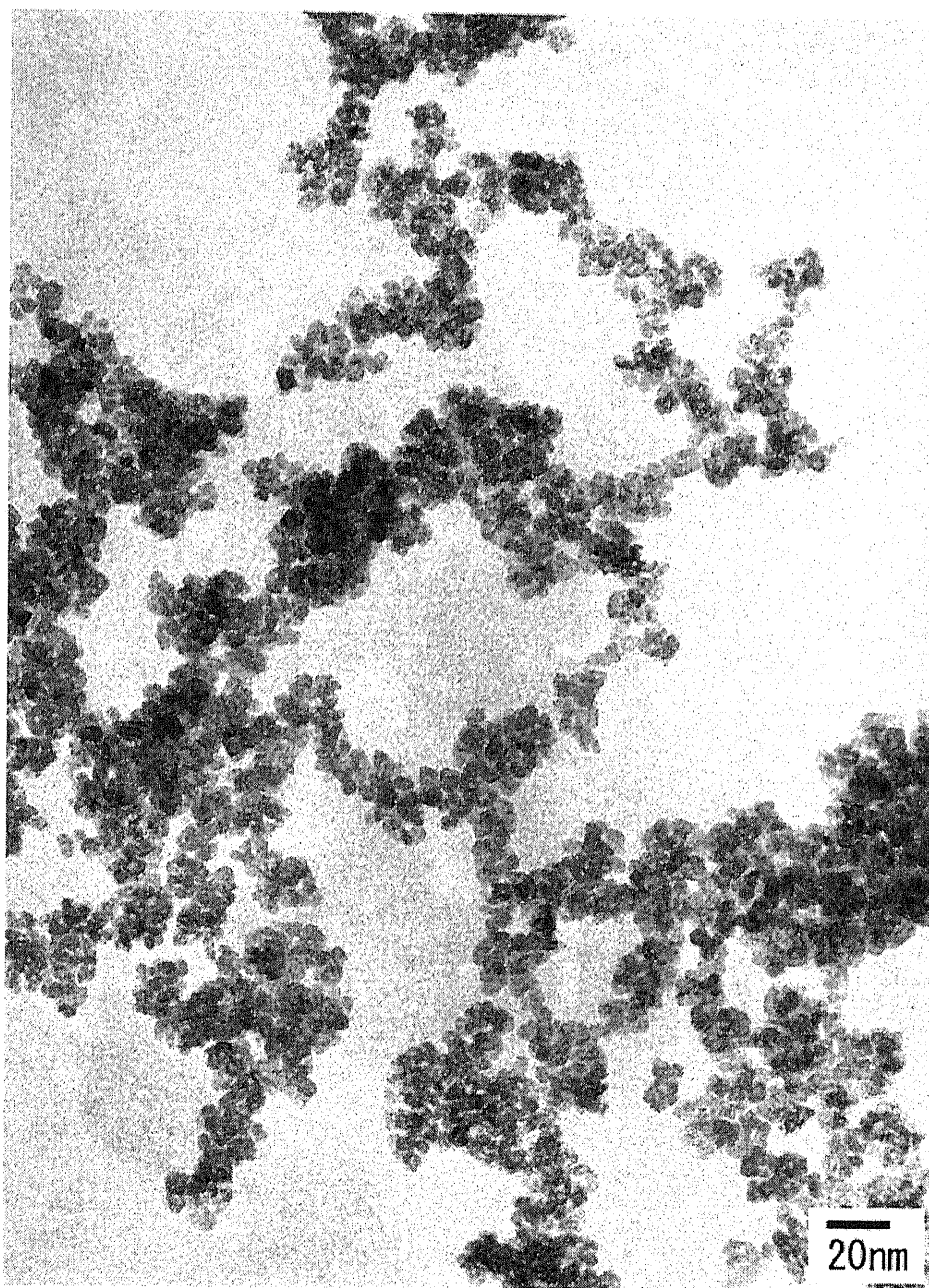


Fig. 5.3 TEM image of CeO₂ calcined at 500 °C.

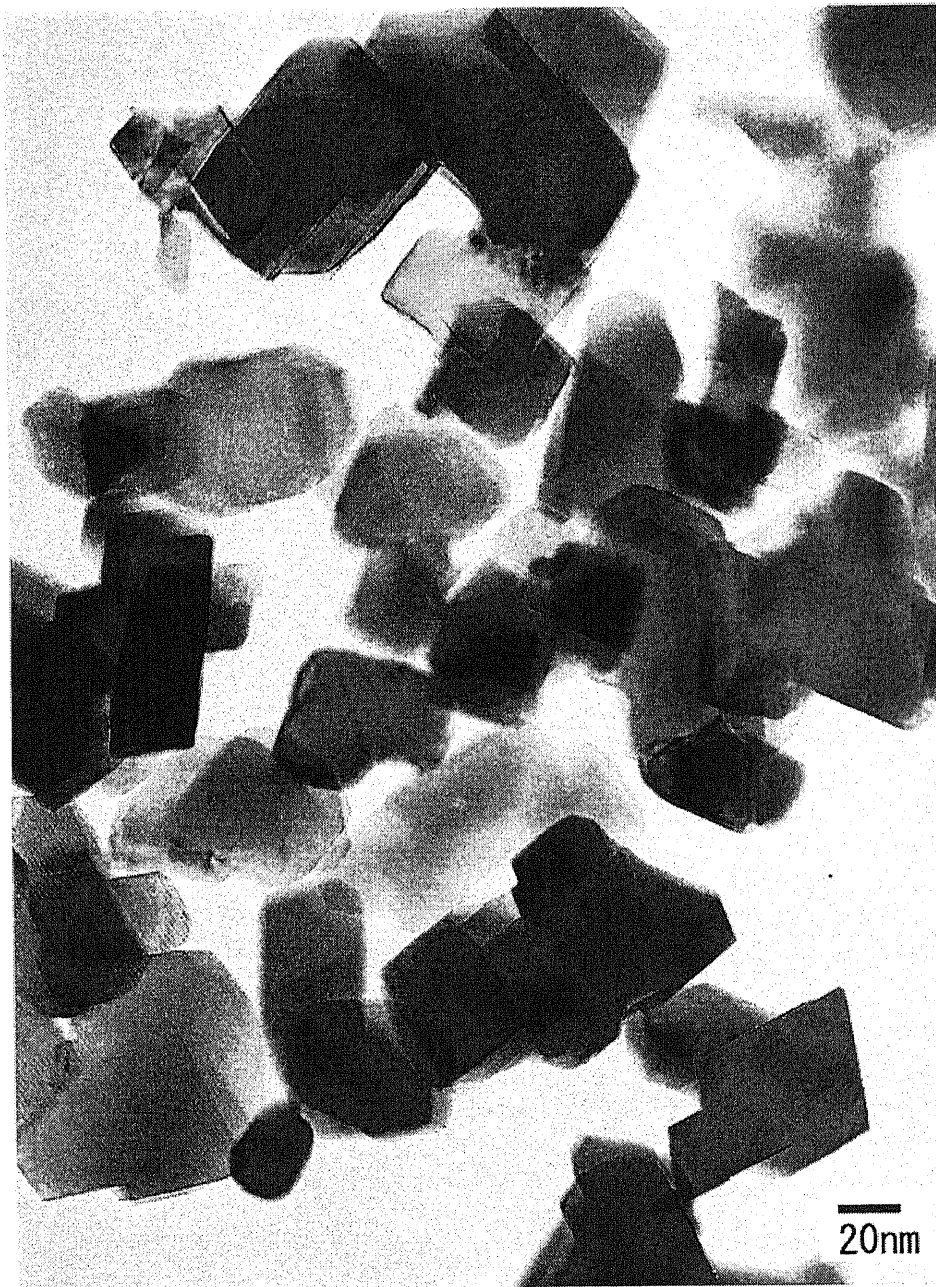


Fig. 5.4 TEM image of CeO₂ calcined at 1000 °C.

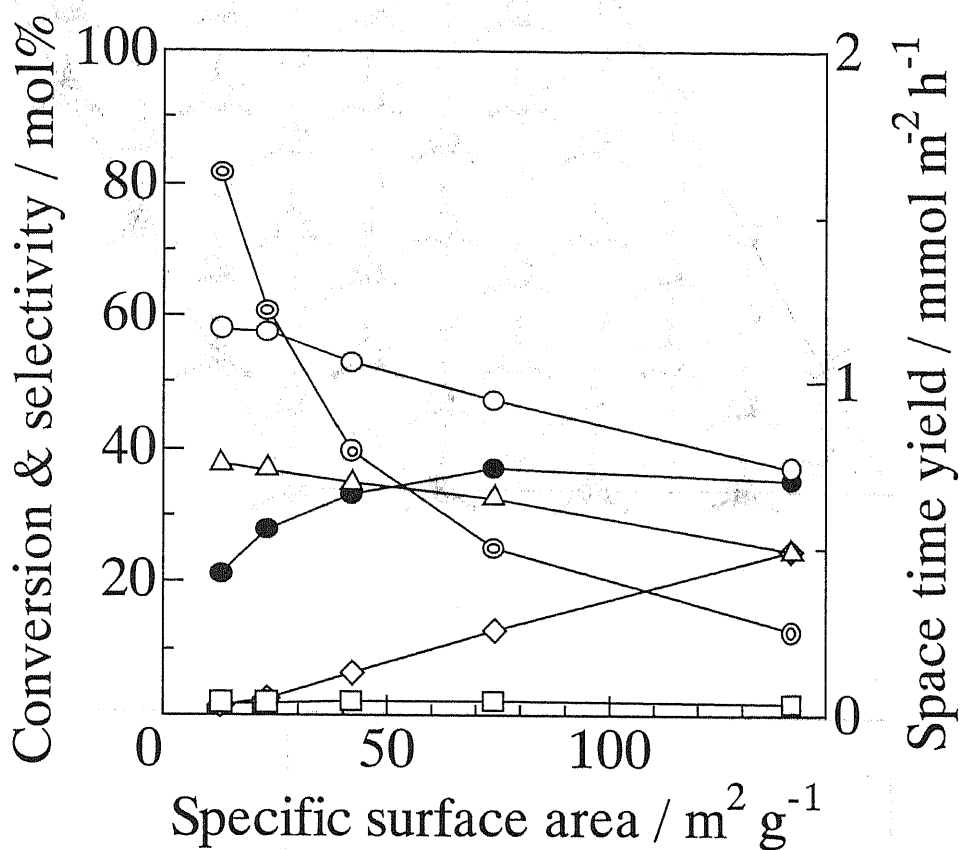
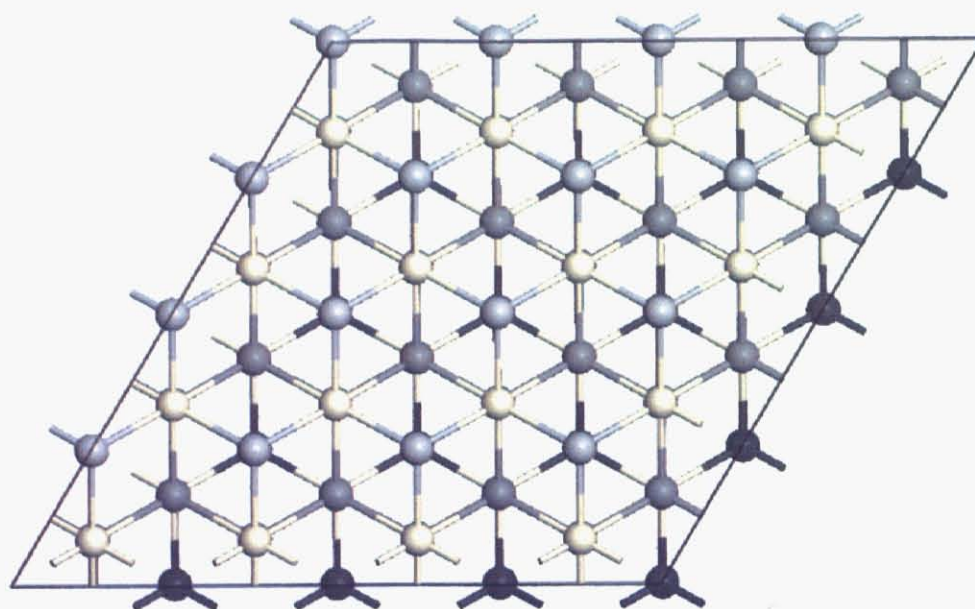
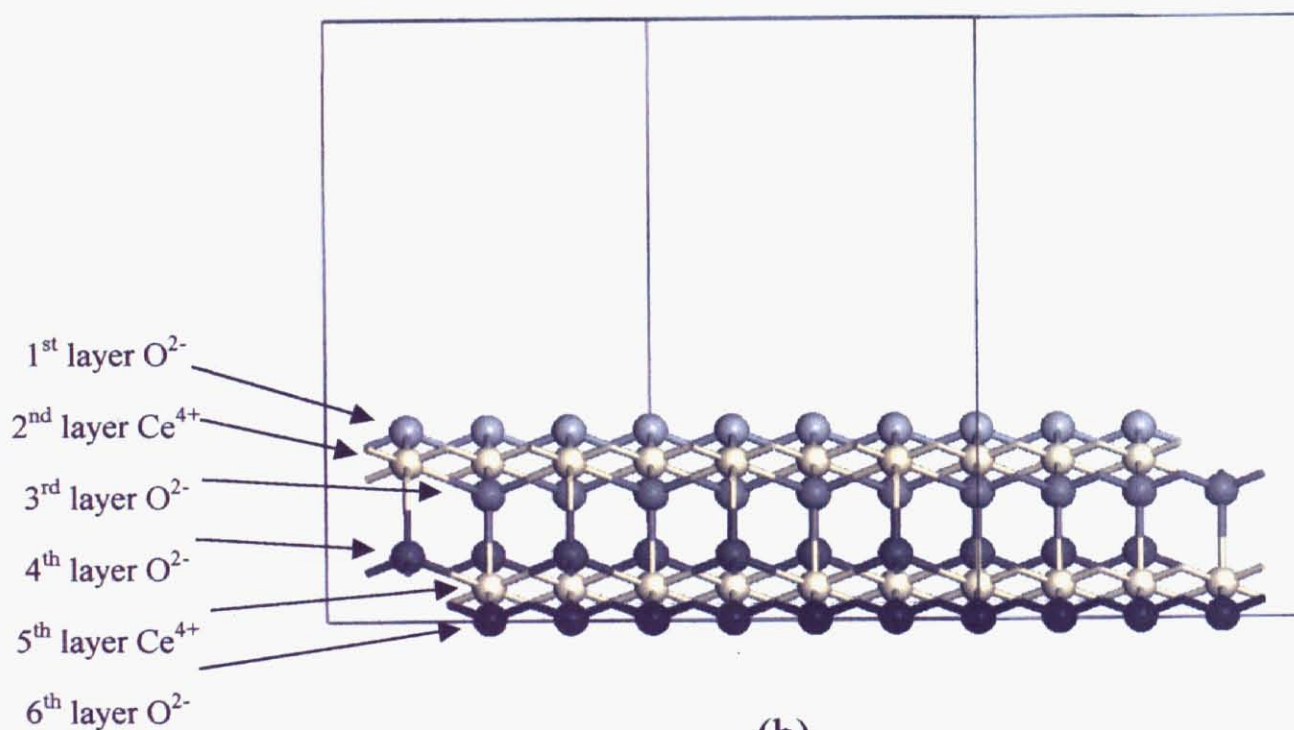


Fig. 5.5 Reaction of 1,3-butanediol over CeO_2 with different specific surface area. (●) conversion of 1,3-butanediol, selectivity to (○) 3-buten-2-ol, (Δ) *trans*-2-buten-1-ol, (\square) *cis*-2-buten-1-ol, (\diamond) methanol and ethanol. (⊙) STY of unsaturated alcohols.



(a)



(b)

Fig. 5.6 Structure of $\text{CeO}_2(111)$ surface employed in DFT calculation. (a) top view, (b) side view.

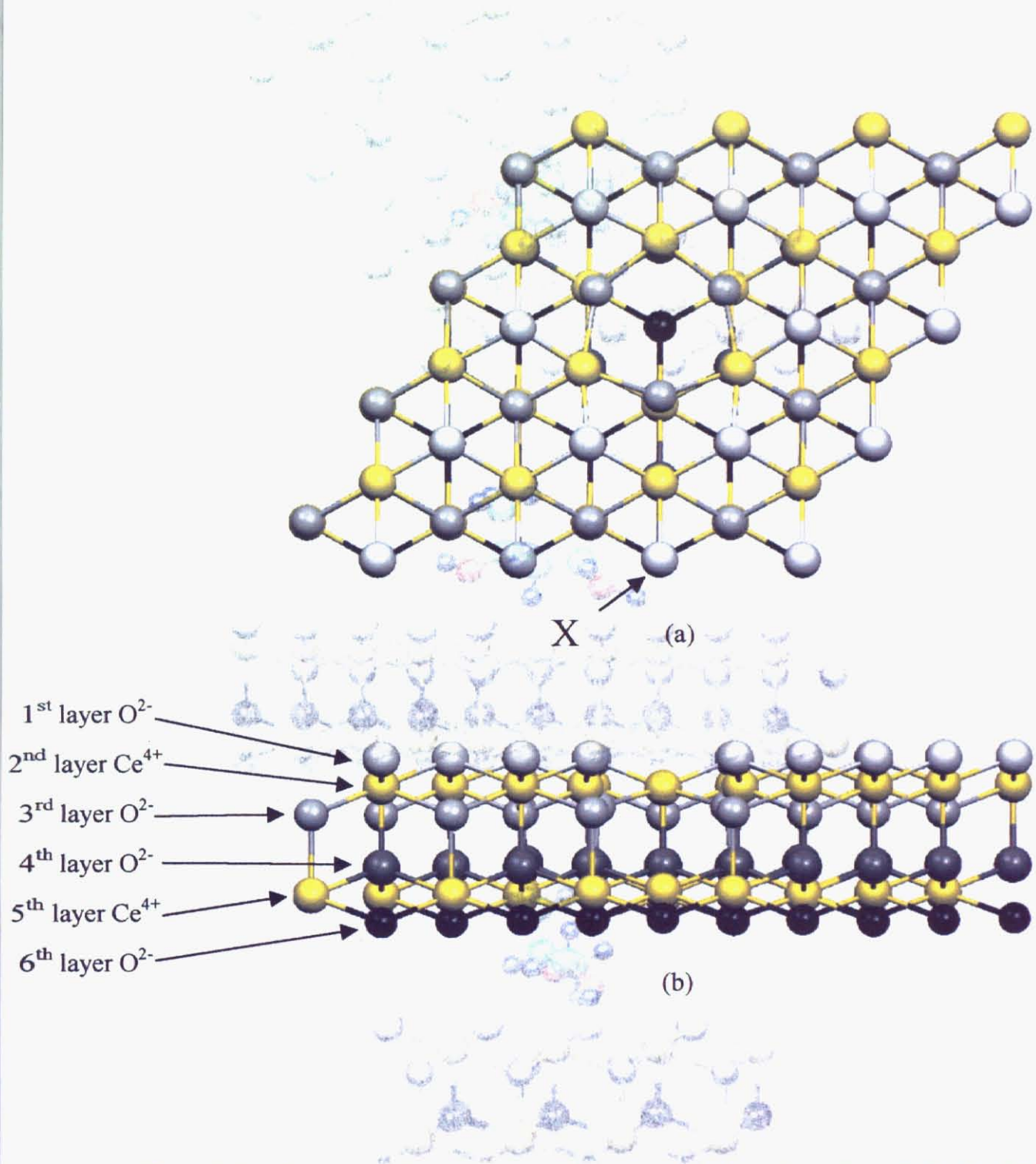


Fig. 5.7 Optimized structure of oxygen-defect introduced $\text{CeO}_2(111)$ surface. (a) top view, (b) side view. In the side view, a 1st layer O atom that is overlapping with oxygen-defect site, namely X assigned in the top view, is removed in order to clearly visualize the oxygen-defect site.

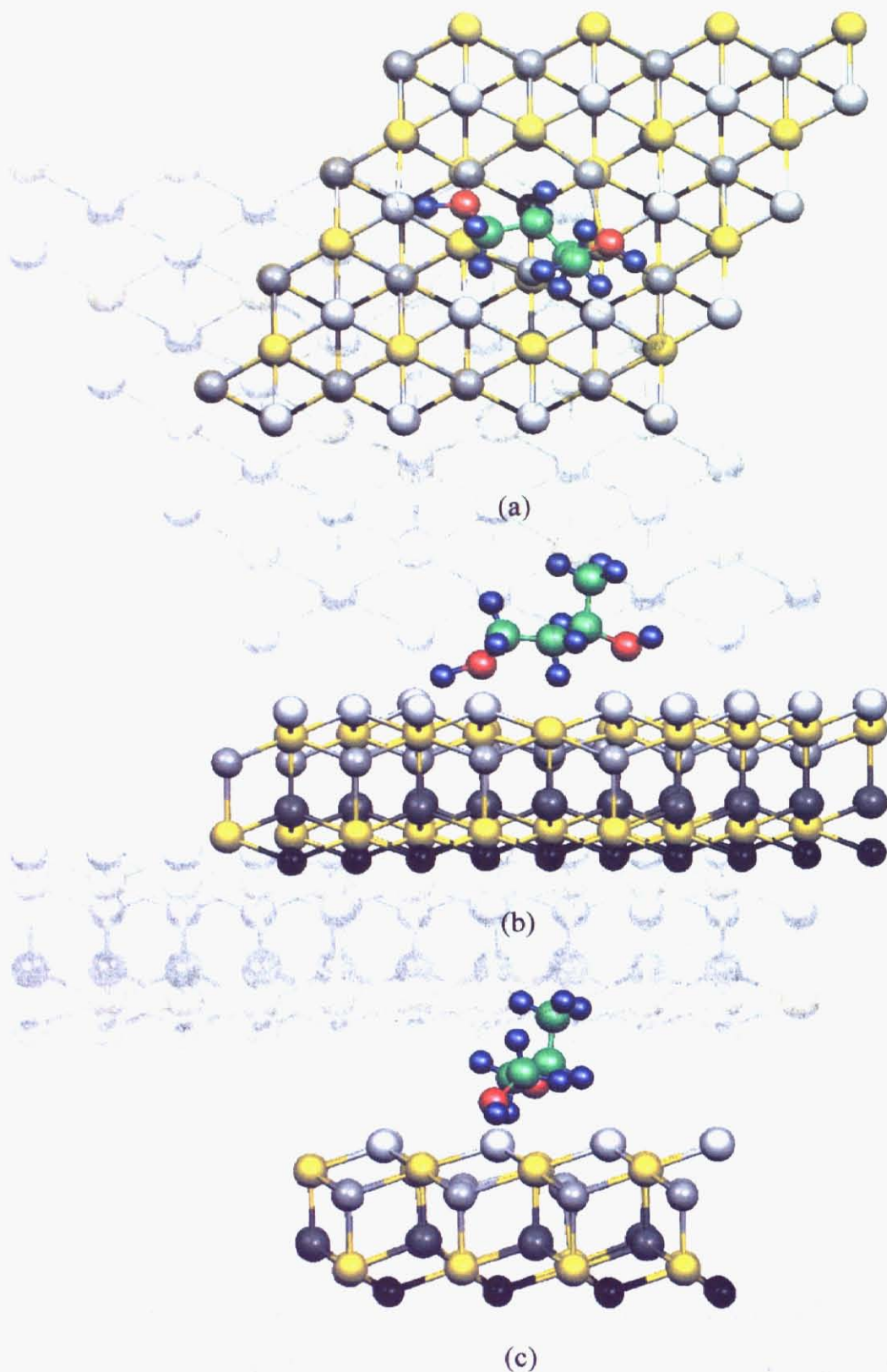


Fig. 5.8 An adsorption of 1,3-butanediol on oxygen-defect site of CeO₂(111) surface optimized by DFT calculation (Structure 1). (a) top view, (b) side view, (c) front view. In the side view, a 1st layer O atom assigned as X in Fig. 5.7 was removed.

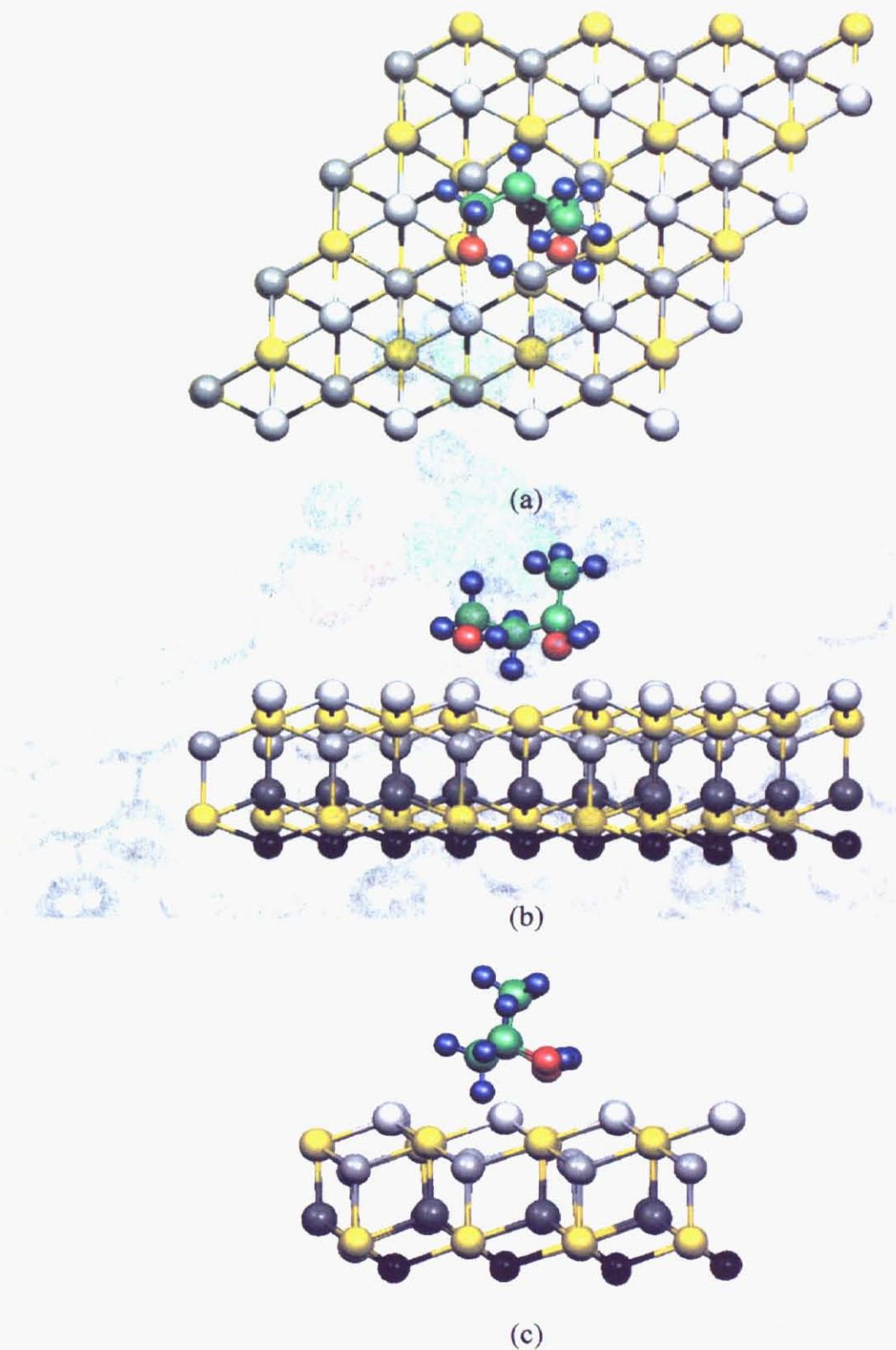


Fig. 5.9 An adsorption of 1,3-butanediol on oxygen-defect site of CeO₂(111) surface optimized by DFT calculation (Structure 2). (a) top view, (b) side view, (c) front view. In the side view, a 1st layer O atom assigned as X in Fig. 5.7 was removed.

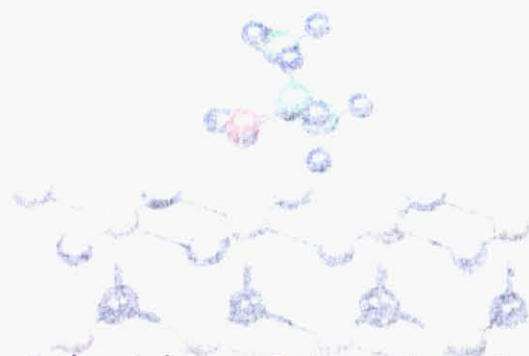
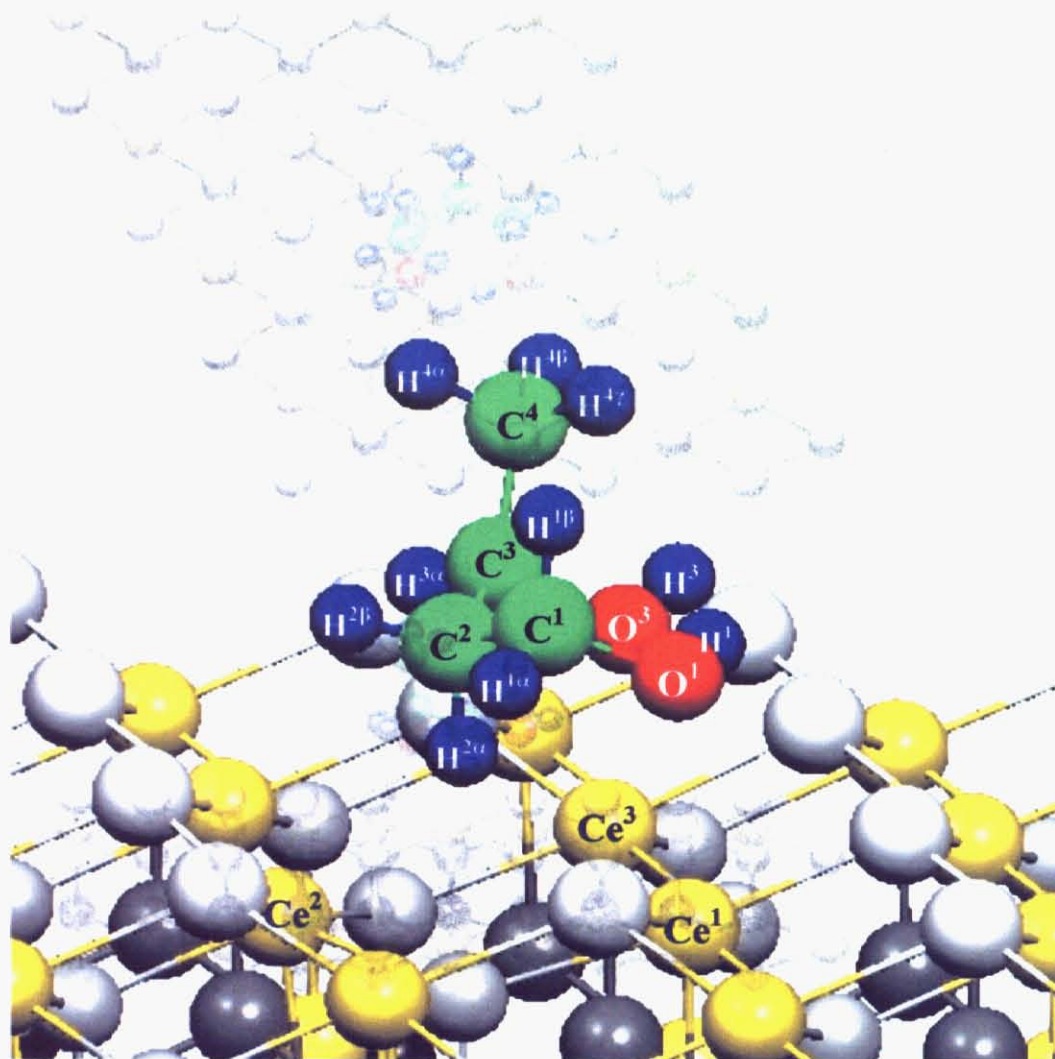


Fig. 5.10 Perspective view of the adsorption of 1,3-butanediol on oxygen-defect site of $\text{CeO}_2(111)$ surface (Structure 2) and nomenclature of the atoms in 1,3-butanediol and three Ce cations.

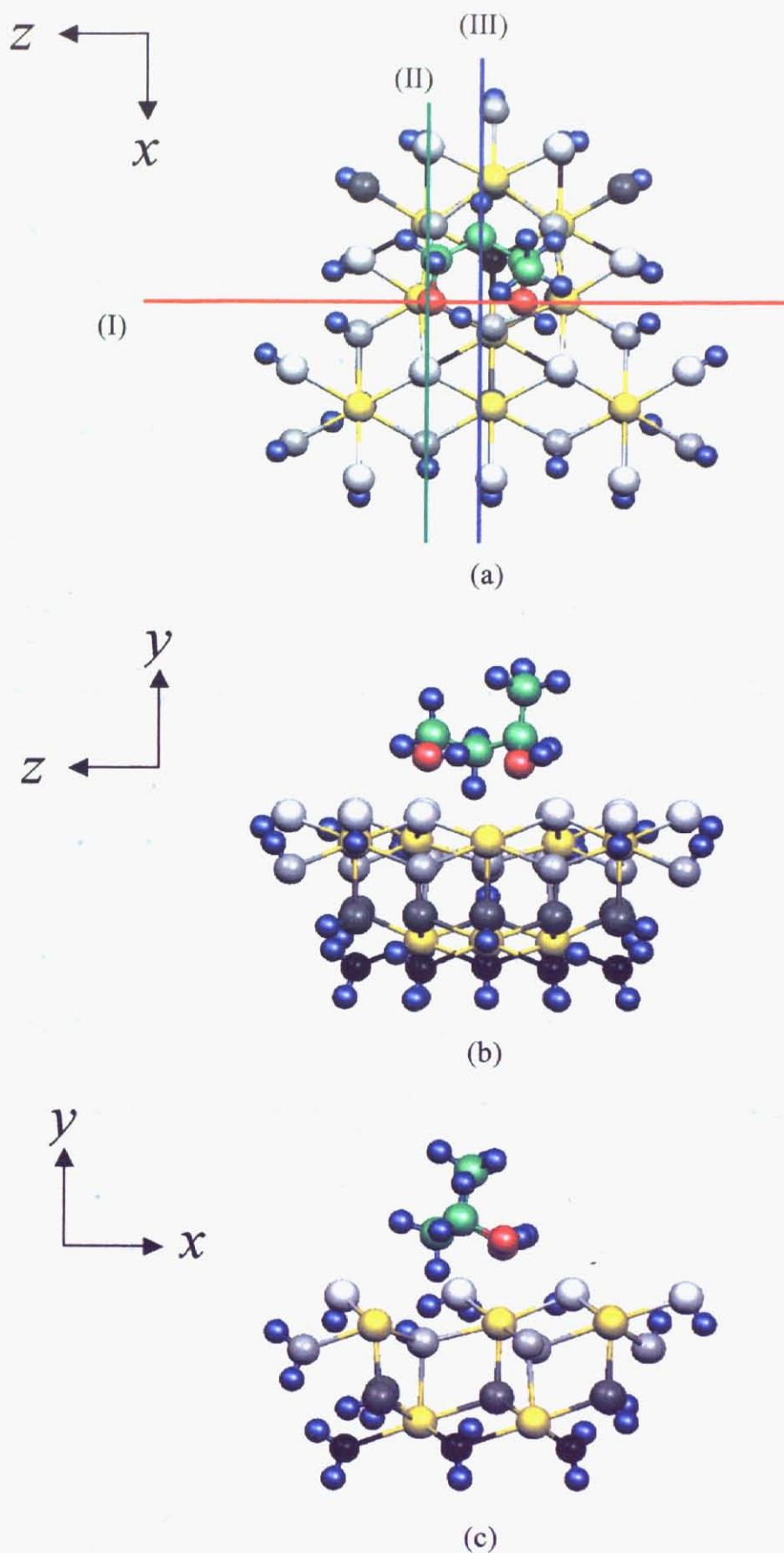


Fig. 5.11 Graphical images of $Ce_9O_{36}H_{26}$ cluster and 1,3-butenediol for PIO calculations with cut-out planes. (a) top view, (b) side view, (c) front view. In the side view, a 1st layer O atom assigned as X in Fig. 5.7 was removed.

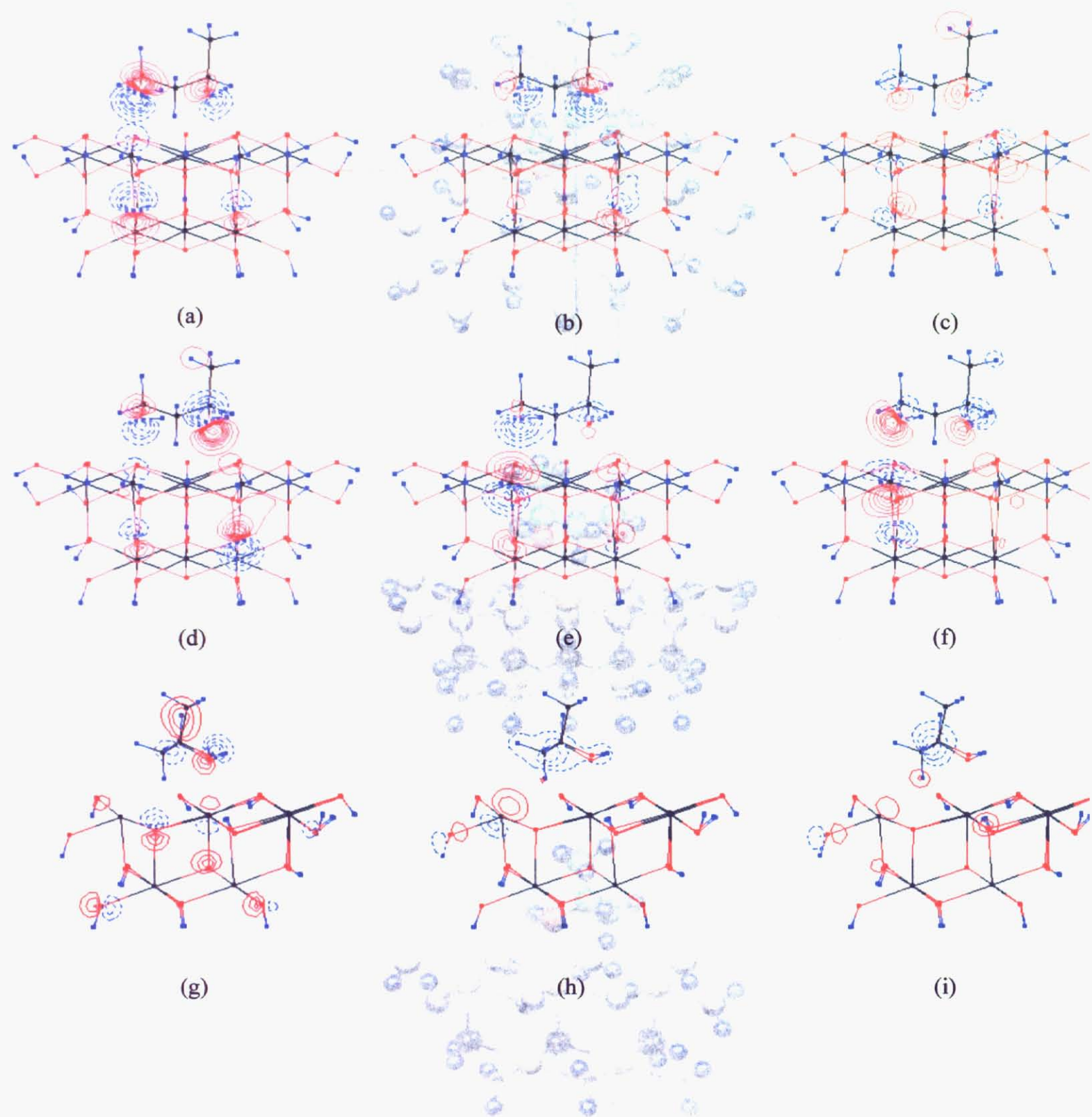


Fig. 5.12 Counter maps of PIO 1-6. (a) PIO-1, (b) PIO-2, (c) PIO-3, (d) PIO-4, (e) PIO-5, (f) PIO-6, (g) PIO-3, (h) PIO-5, (i) PIO-6. (a-f) are the images from the view of the cut-out plane (I) in Fig. 5.11a, (g) from (II), and (h, i) from (III).

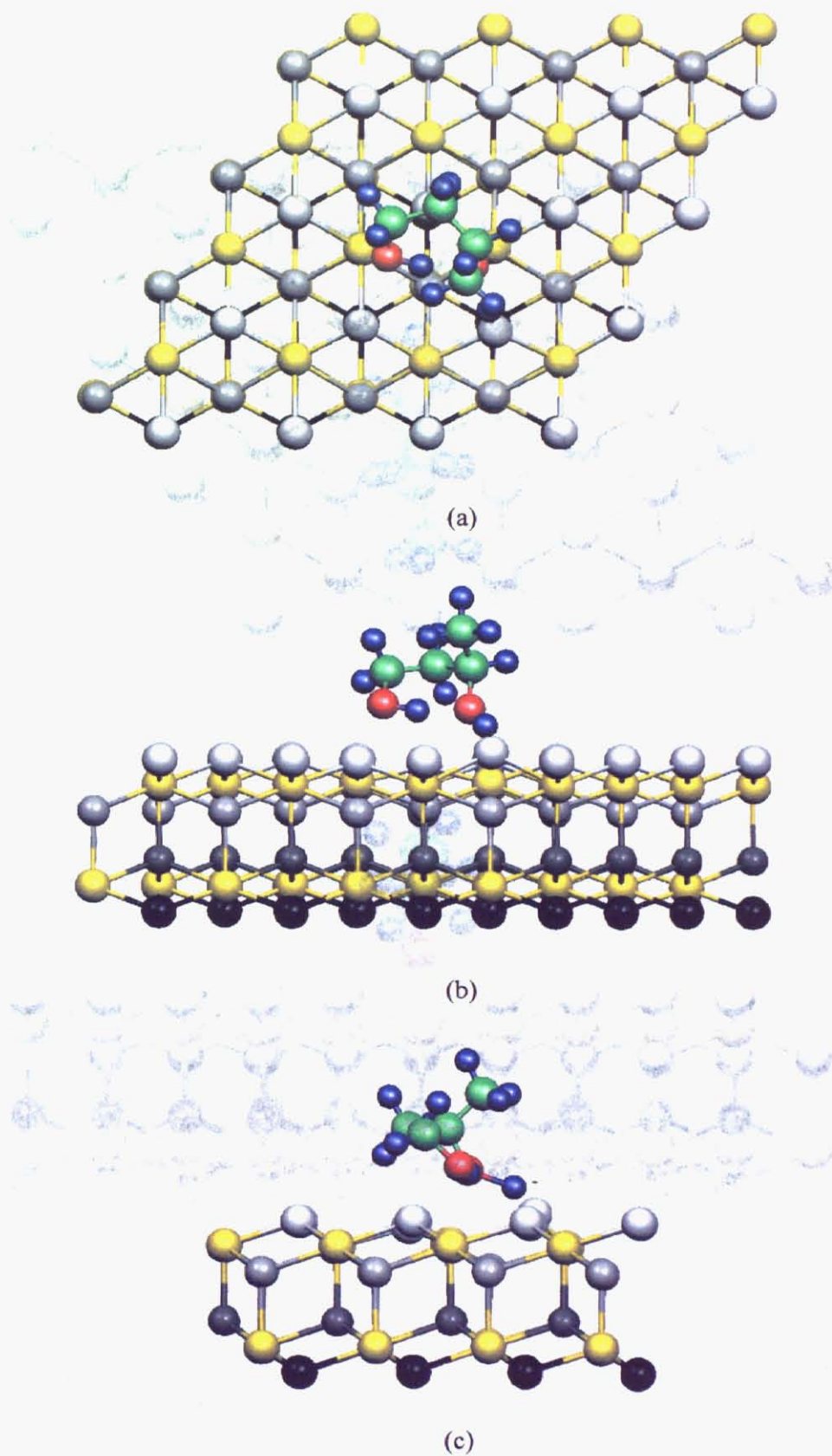


Fig. 5.13 An adsorption of 1,3-butanediol on stoichiometric CeO₂(111) surface optimized by DFT calculation (structure 3). (a) top view, (b) side view, (c) front view.

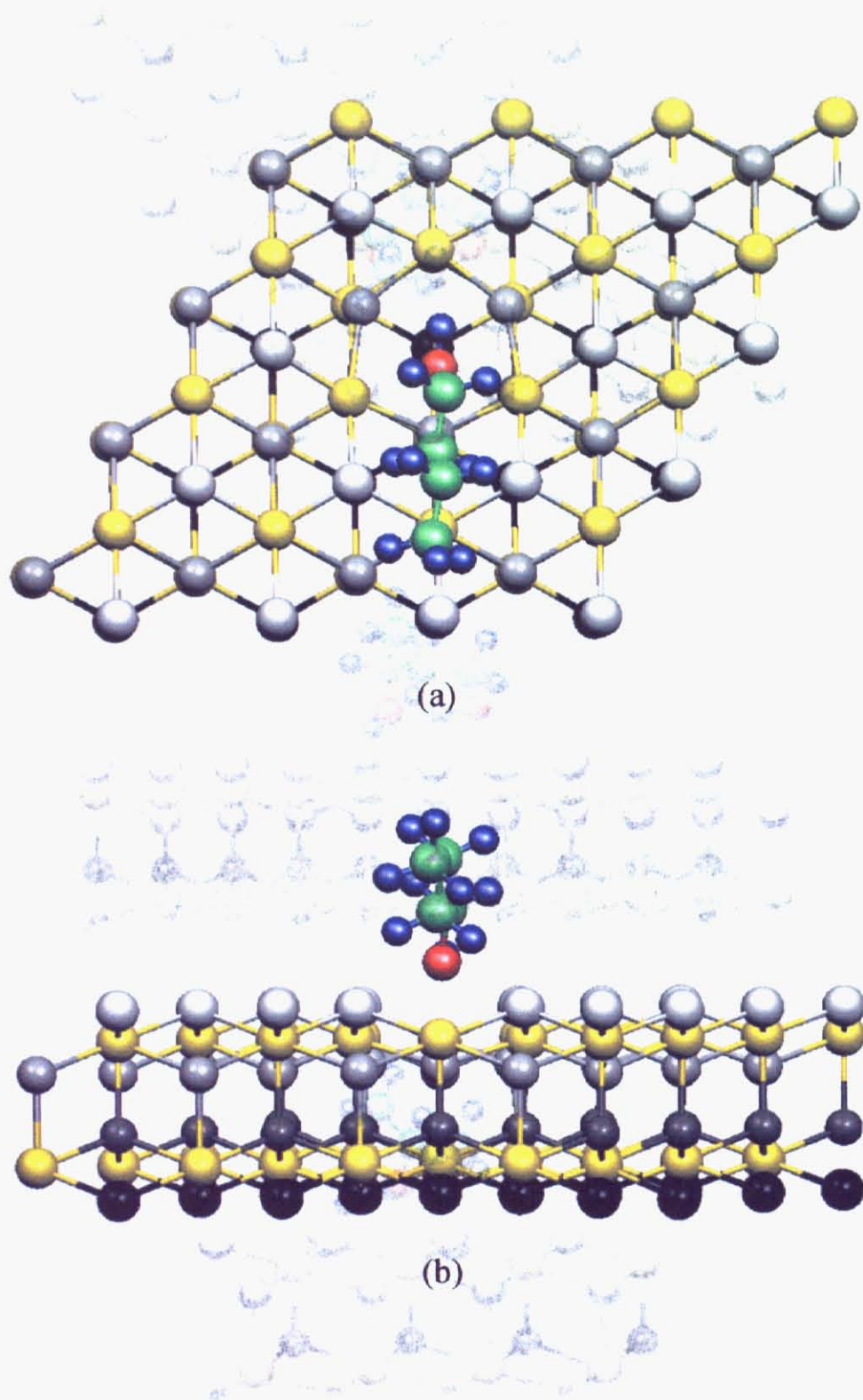
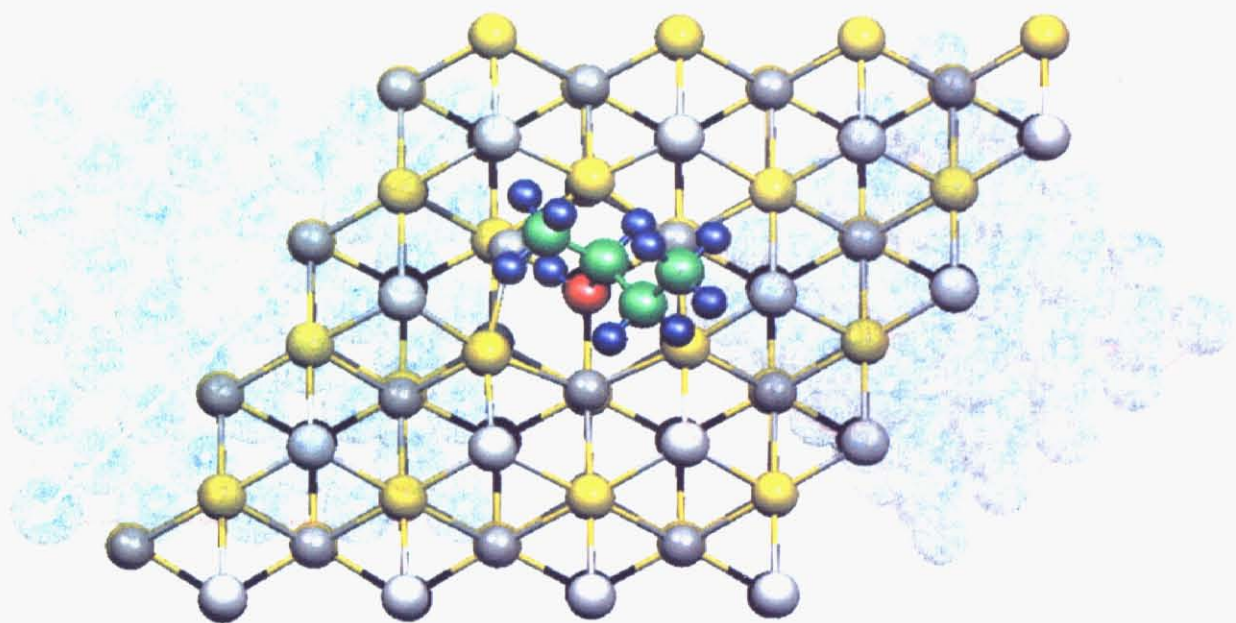
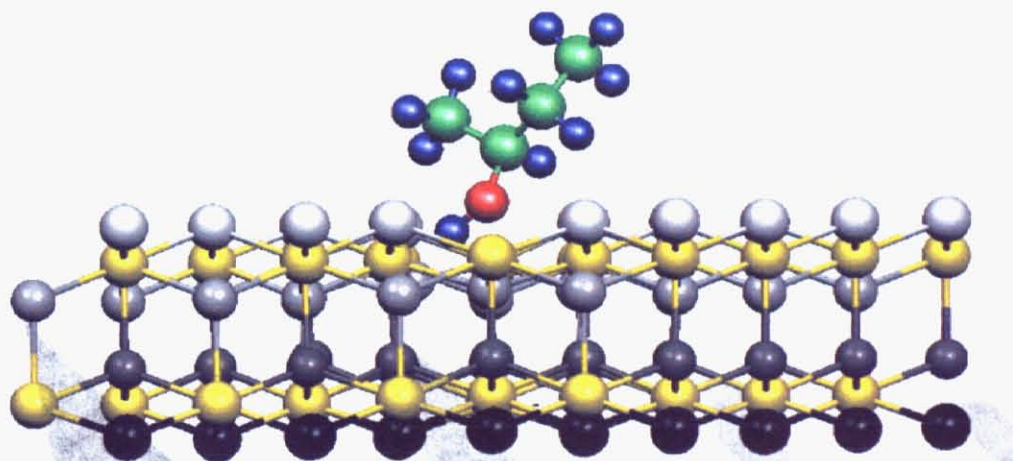


Fig. 5.14 Adsorption structure of 1-butanol on oxygen-defect site of $\text{CeO}_2(111)$ surface. (a) top view, (b) side view. In the side view, a 1st layer O atom assigned as X in Fig. 5.7 was removed.



(a)



(b)

Fig. 5.15 Adsorption structure of 2-butanol on oxygen-defect site of $\text{CeO}_2(111)$ surface. (a) top view, (b) side view. In the side view, a 1st layer O atom assigned as X in Fig. 5.7 was removed.

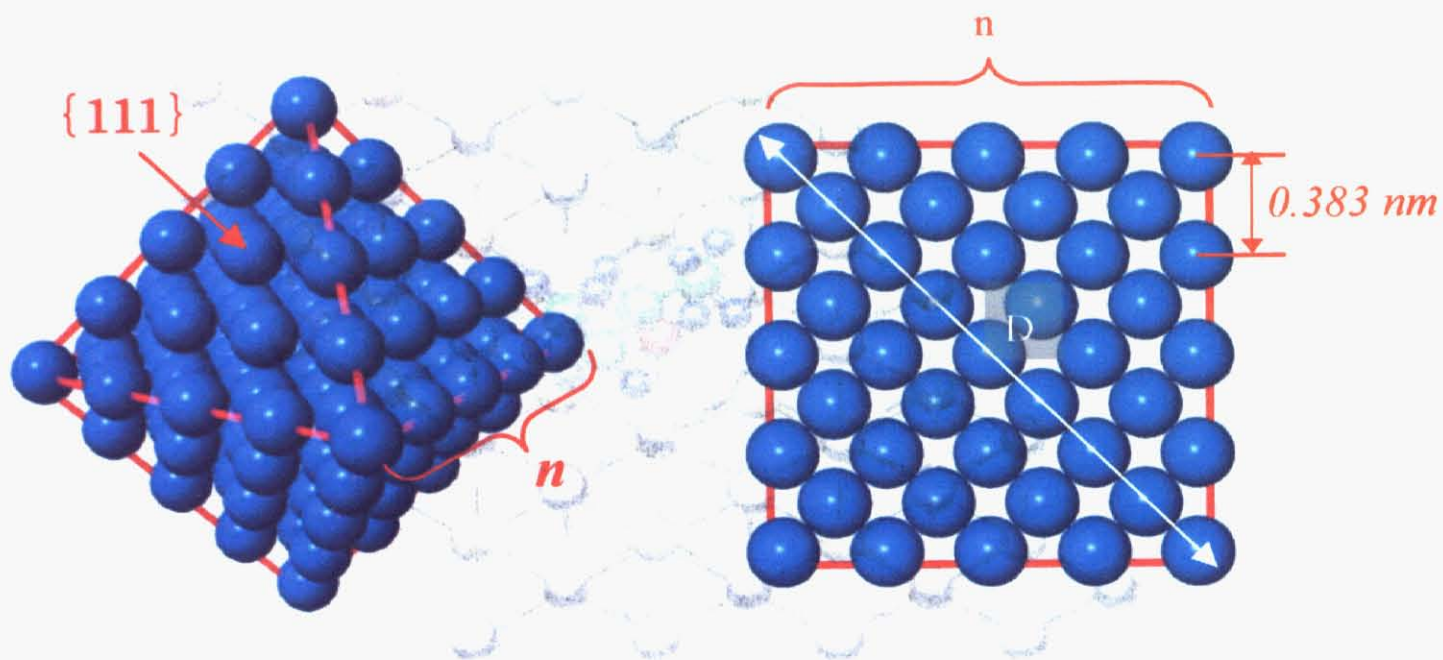


Fig. 5.16 Model of CeO₂ particle for the estimation of fraction of surface oxygen atom. (a) Perspective view, (b) cross-section image of CeO₂ particle along $\langle 100 \rangle$ direction. Balls express oxygen anions, and cerium cations are not drawn

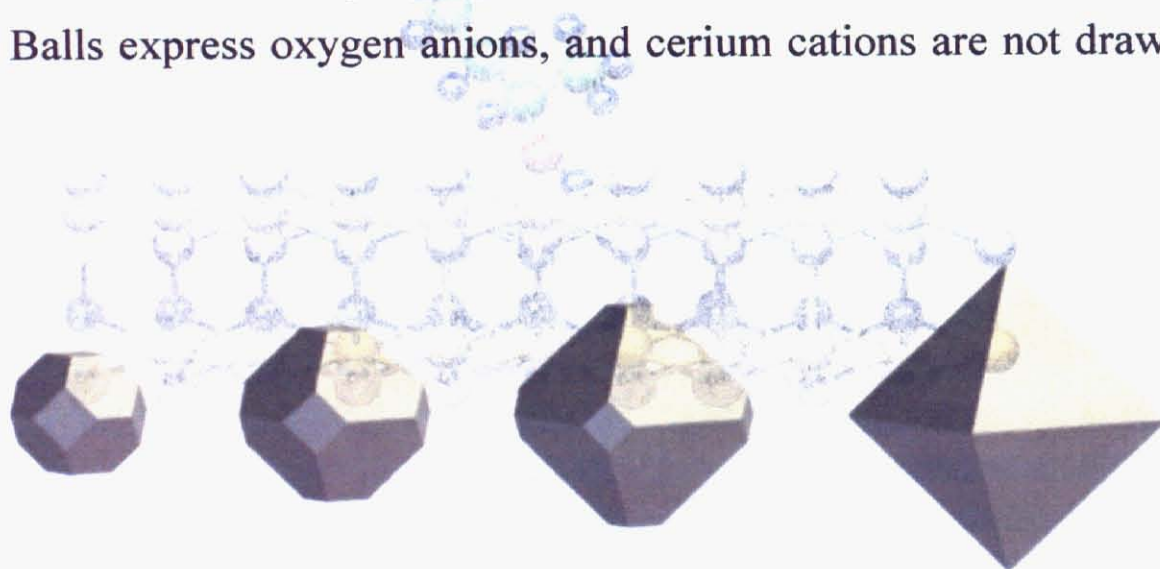


Fig. 5.17 Images of the change in the morphology of CeO₂ particle with increasing the particle size, D .

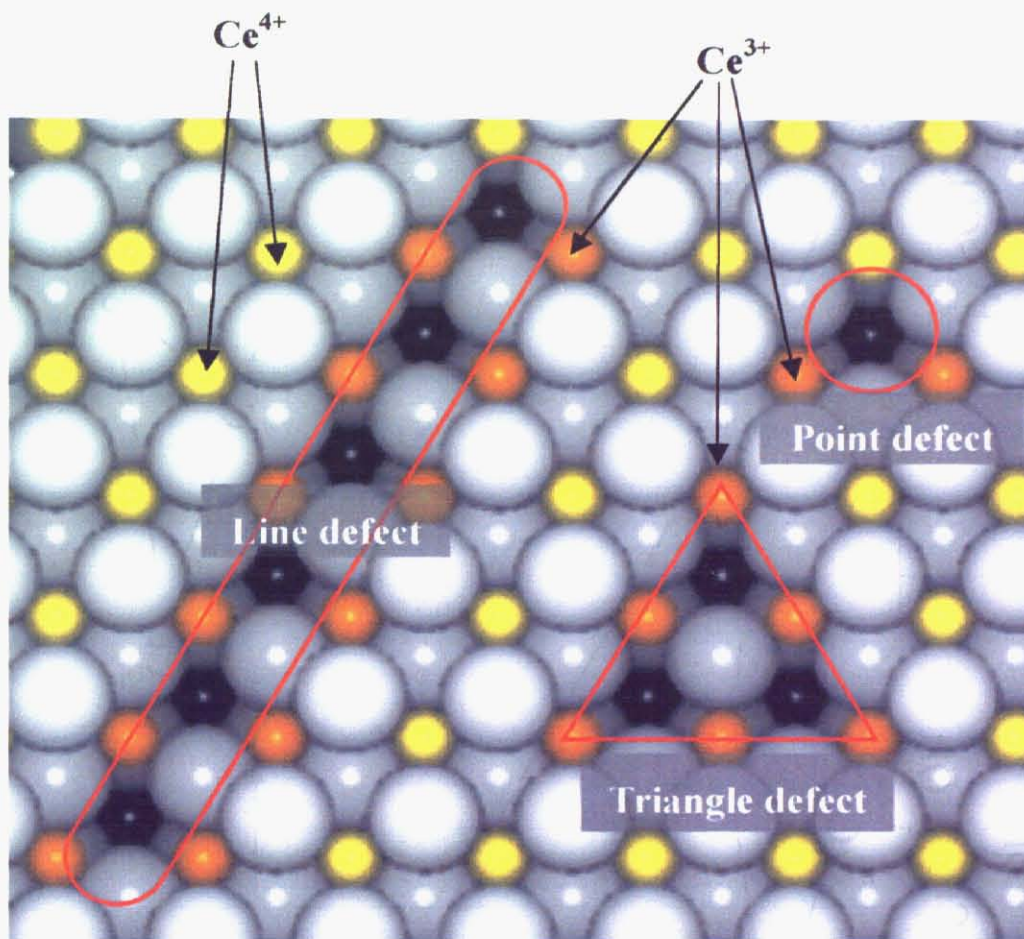
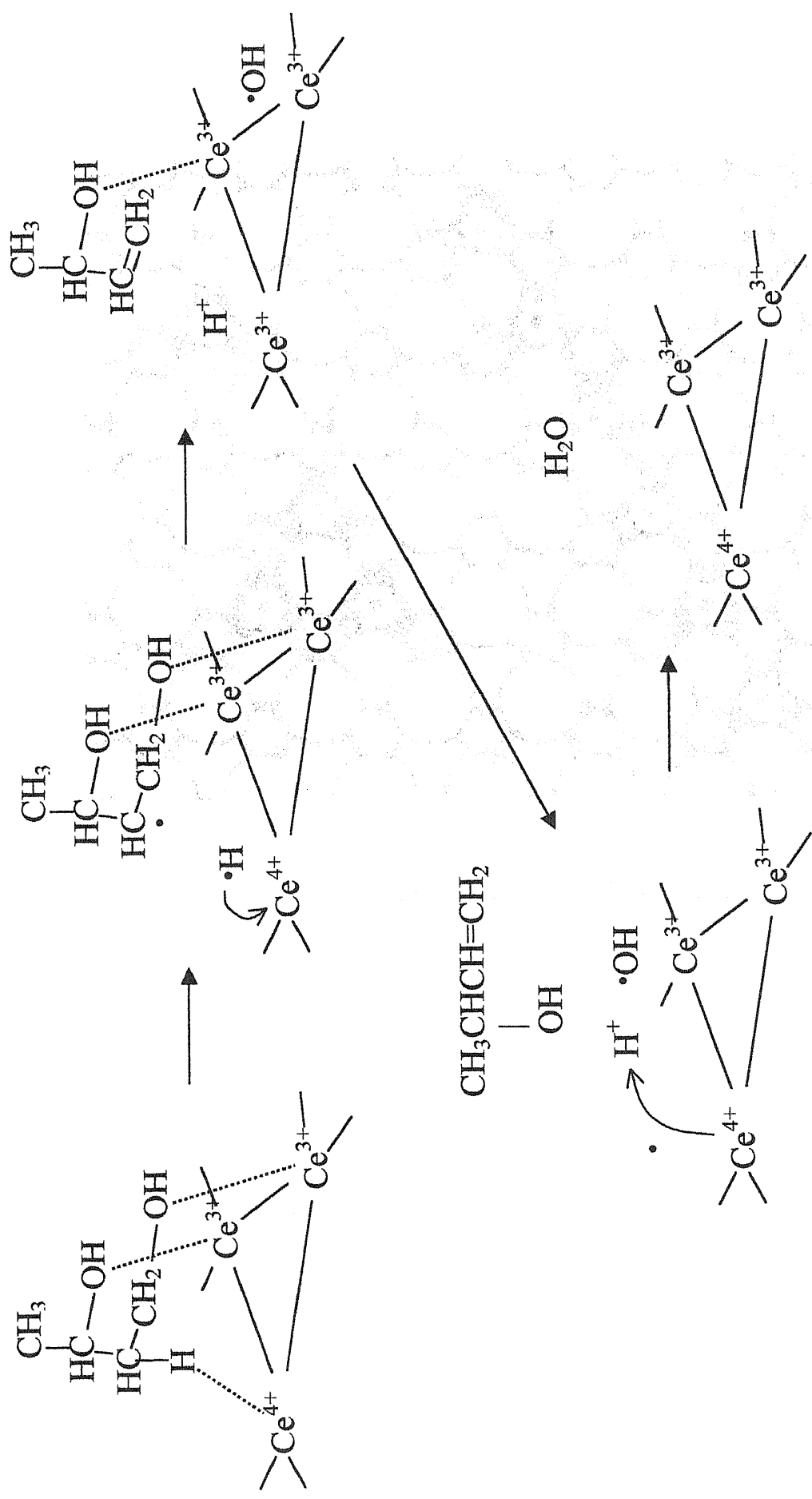


Fig. 5.18 Image of $\text{CeO}_2(111)$ surface with single and multiple oxygen-defect site. The small and large balls represent Ce cations and O anions, respectively.



Scheme 5.1 Proposed reaction mechanism of dehydration of 1,3-butanediol over oxygen-defect site of CeO₂(111)

General conclusions

The present thesis has described the studies on the utilization of 1,3- and 1,4-butanediol (BDO). Four different reactions of butanediols were investigated and I proposed that they are promising chemical resources for the valuable products.

In Chapter 2, the dehydrogenation of 1,4-BDO into γ -butyrolactone (GBL) was investigated over Cu-based catalysts with metal-oxide additives such as ZnO, ZrO₂ and Al₂O₃. The addition of Al₂O₃ enlarged the specific and Cu surface area, whereas the catalytic activity of Cu-Al₂O₃ was not high. The cyclic dehydration of 1,4-BDO into tetrahydrofuran (THF) proceeded over Cu-Al₂O₃ due to high acidity of Al₂O₃. ZrO₂ drastically enhanced catalytic performance while ZnO hardly affected it. The reaction pathway was concluded as follows: initially, 1,4-BDO was dehydrogenated into 4-hydroxybutanal, which was rapidly transformed into 2-hydroxytetrahydrofuran (2HTHF). 2HTHF was further dehydrogenated to produce GBL. It was concluded that the active center of dehydrogenation is metallic Cu.

In Chapter 3, effective catalysts for the dehydration of 4-hydroxy-2-butanone (HB), which can be obtained via dehydrogenation of 1,3-BDO, into 3-buten-2-one (MVK) were investigated. It was found that anatase-TiO₂, which had quite weak acid sites, exhibited good performance. The catalysts with strong acid sites such as SiO₂-Al₂O₃, Al₂O₃, and rutile-TiO₂ were rapidly deactivated due to the deposition of carbon species. The reaction temperature at 160 °C was optimal: the temperatures below and above 160 °C induced the deactivation because of the poisoning of produced MVK and deposition of carbon species, respectively.

In Chapter 4, the examination of the reaction of 1,3-BDO over four catalysts with different acid-base property was described. The catalytic activity was affected by

the acidity of the catalysts. The products distribution was quite different over the catalysts. Over $\text{SiO}_2\text{-Al}_2\text{O}_3$, 1,3-BDO was preferably dehydrated into 3-buten-1-ol and it was consecutively dehydrated into 1,3-butadiene. Al_2O_3 catalyzed 1,3-BDO into 4-methyl-1,3-dioxane, which was acetal compound of 1,3-BDO with formaldehyde. Over TiO_2 and ZrO_2 , product distribution was quite complicated because of several reactions such as dehydration, dehydrogenation, hydrogenation and decomposition proceeded. The unsaturated alcohols were formed over acid-base catalysts, but not selectively.

In Chapter 5, the reaction of 1,3-BDO over CeO_2 , the active site, and the reaction mechanism of 1,3-BDO dehydration into unsaturated alcohols over CeO_2 were investigated. Judging from the reaction results, it was speculated that plane (111) was an active surface for the dehydration. Sequentially, the adsorption of 1,3-BDO on (111) surface with/without an oxygen-defect was investigated with computational technique. 1,3-BDO was preferably adsorbed on the oxygen-defect site of $\text{CeO}_2(111)$ and it was confirmed that the elongation of $\text{C}^2\text{-H}^{2\alpha}$, $\text{C}^1\text{-O}^1$ and $\text{C}^3\text{-O}^3$ bonds in 1,3-BDO, which correspond to the activated part in actual dehydration of 1,3-BDO. Therefore, it was concluded that oxygen-defect site of $\text{CeO}_2(111)$ surface was the active one, and that the reaction proceeded following mechanism: initially, $\text{H}^{2\alpha}$ was radically abstracted by Ce^{4+} cation. H radical donated one electron to reduce Ce^{4+} to Ce^{3+} and the H radical itself was oxidized to proton. Then, one of the OH groups was abstracted radically to form unsaturated alcohols, and the OH radical and proton combined to produce H_2O with accepting one electron from Ce^{3+} , and Ce^{3+} was oxidized into Ce^{4+} .

List of publication

Chapter 2

“Dehydrogenative cyclization of 1,4-butanediol over copper-based catalyst”

N. Ichikawa, S. Sato, R. Takahashi, T. Sodesawa, K. Inui, *J. Mol. Catal. A* **212** (2004) 197-203.

Chapter 3

“Synthesis of 3-buten-2-one from 4-hydroxy-2-butanol over anatase-TiO₂ catalyst”

N. Ichikawa, S. Sato, R. Takahashi, T. Sodesawa, *Catal. Commun.* **6** (2005) 19-22.

Chapter 4

“Catalytic reaction of 1,3-butanediol over solid acids”

N. Ichikawa, S. Sato, R. Takahashi, T. Sodesawa, will be submitted to *J. Mol. Catal. A*.

Chapter 5

“PIO study on 1,3-butanediol dehydration over CeO₂(111) surface”

N. Ichikawa, S. Sato, R. Takahashi, T. Sodesawa, *J. Mol. Catal. A* **231** (2005) 181-189.

“Dehydration of butanediols over CeO₂ catalysts with different particle size”

A. Igarashi, N. Ichikawa, S. Sato, R. Takahashi, T. Sodesawa, accepted in *Appl. Catal. A*.

“Theoretical investigation of the adsorption of 1,3-butanediol on oxygen-defected CeO₂(111) surface”

N. Ichikawa, S. Sato, R. Takahashi, T. Sodesawa, Harunori Fujita, Takashi Atoguchi, Akinobu Shiga, *J. Catal.* submitted.

Related articles

“Effective formation of ethyl acetate from ethanol over Cu-Zn-Zr-Al-O catalysts”

K. Inui, T. Kurabayashi, S. Sato, N. Ichikawa, *J. Mol. Catal. A* **216** (2004) 147-156.

Acknowledgement

The present thesis has been carried out under the supervision of Professor Toshiaki Sodesawa at Graduate School of Science and Technology, Chiba University.

The author would like to express gratitude to Professor Toshiaki Sodesawa for his guidance in the accomplishment of this study. The author acknowledges Professor Satoshi Sato, Professor Fumihiko Akutsu, Professor Shogo Shimazu, and Professor Kyoichi Saito for reviewing the present thesis and their useful advice.

The author acknowledges Dr. Kanichiro Inui for his assistance in a part of experiment and helpful discussion.

The author gratefully wishes to express thank Professor Satoshi Sato for his assistance in large part of this study, and to thank Dr. Ryoji Takahashi for his valuable discussion and helpful suggestion.